NTNU
Norwegian University of
Science and Technology

Nickel Cobalt Catalyst for Methane Abatement in Marine Machinery

Ragnhild Brokstad Lund-Johansen

Chemical Engineering and Biotechnology
Submission date: June 2017
Supervisor: Hilde Johnsen Venvik, IKP
Co-supervisor: Jia Yang, IKP
Rune Lødeng, SINTEF

Norwegian University of Science and Technology
Department of Chemical Engineering

Preface

This master thesis is written for the Catalysis group in relation to the final year of the study of Chemical Engineering at the Norwegian University of Science and Technology.

I would like to thank my supervisor, Professor Hilde Venvik, for her excellent and continuous guiding during the time line of the research. I would also like to thank my co-supervisor, Senior Scientist at SINTEF, Rune Lødeng, for his guidance especially in regards to reporting. Co-supervisor, Associate Professor Jia Yang, has been a precise guide in regards to the reaction rig, and she has my sincere gratitude, especially during the times of hardware malfunction.

Finally, I would like to thank all the people who have made my six years of studies in Trondheim to a memorable time, especially Mirna Aleric and Silje Salbostad, who have been wonderful supports during a hectic final year. I also thank Morten Lund-Johansen, for helping me improve my academic language, Helene and Marie Lund-Johansen, for keeping me motivated, and finally Rita Brokstad for being a continuous inspiration.

Declaration of Compliance

I declare that this is an independent work according to the exam regulations at the Norwegian University of Science and Technology.

Trondheim, Norway
June 9, 2017

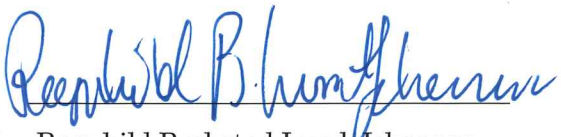

Ragnhild Brokstad Lund-Johansen

Abstract

Natural gas vehicles (NGVs) have been suggested as an alternative to conventional vehicles in the marine sector, in order to reduce the large contribution this sector provides to greenhouse gas emissions. Natural gas has been found to produce lower emissions particulates and CO_2, $NO_x$and SO_x gases, than heavy fuel oil, which is conventionally used as fuel for ships. However, the lean combustion that facilitates this reduction, entails methane slip in the exhaust gas which counter balance the environmental advantages by employing NG. Methane abatement from the exhaust gas can be facilitated by complete catalytic oxidation of methane, however, the conditions and the composition of the exhaust gas require demanding properties of the catalytic material. Supported palladium has been shown to display superior activity, but the material's sensitivity to presence of water vapour and the high price and limited availability of the material have encouraged researchers to investigate alternative materials.

In this master thesis mixed metal oxides of nickel and cobalt have been studied for complete catalytic oxidation of methane. The catalytic activity was investigated for dependency on stoichiometric ratio between nickel and cobalt, calcination temperature during preparation and deposition of a small load of palladium on the surface. The activity dependency of methane concentration in feed, and in the presence of water were investigated, to conclude on the activity in realistic exhaust gas conditions. All catalysts were synthesized by the coprecipitation method, and the Pd deposition was conducted by incipient wetness impregnation. The catalysts were characterized with XRD, N_2 physisorption, XRF, Raman spectroscopy and TEM.

It was found that mixed oxides of nickel and cobalt generally displayed high activity for methane oxidation at relatively low temperatures, although the activity was reduced reversibly in the presence of water. Kinetic investigations suggested that addition of water altered the kinetic model of the system. The ratio of nickel and cobalt showed limited influence on catalytic activity. The catalysts investigated for this purpose displayed similar reaction rates and activation energies of reasonable values, estimated with a kinetic model that was of first order in methane and zero in oxygen. It was further observed that the catalysts underwent structural changes during first reaction cycle over fresh catalyst. Palladium enhanced the catalytic activity considerably, possibly due to the high obtained Pd dispersion and/or a synergic effect between Pd and the mixed oxide support. Based on the kinetic investigation, it was possible that the catalyst comprising palladium followed the assumed model to a greater extent than the mixed oxides. Conclusively, mixed oxides of nickel and cobalt show promising potential for after treatment of NGV exhaust gas.

Sammendrag

Fartøy drevet av naturgass (NG) har blitt foreslått som et alternativ til konvensjonelle fartøy, for å redusere de høye utslippene av drivhusgasser fra maritim sektor. Naturgass har blitt funnet til å produsere lavere utslipp av partikler, CO_2-, NO_x- og SO_x-gasser enn konvensjonell bunkerolje, som vanligvis brukes som drivstoff i skip. "Lean" forbrenning, som fasiliterer denne reduksjonen, forårsaker derimot metanlekkasje i eksosen, som motvirker de miljømessige fordelene ved bruk av NG. Metanlekkasjen kan reduseres ved katalytisk etterbehandling av eksosen, men sammensetningen og forholdene i eksosen medfører at krevende katalysatoregenskaper må oppnås. Palladium på bærer har vist overlegen aktivitet, men materialets sensitivitet i kontakt med vanndamp, i samspill med materialets høye pris og begrensede tilgjengelighet har motivert forskere til å undersøke alternative materialer.

I denne masteroppgaven har blandede metalloksider av nikkel og kobolt blitt undersøkt for katalytisk oksidasjon av metan. Den katalytiske aktiviteten ble undersøkt for avhengighet av støkiometrisk forhold mellom nikkel og kobolt, kalsineringstemperatur ved syntese og ved avsetning av en liten fraksjon palladium på overflaten. Videre ble avhengigheten av fødekonsentrasjonen av metan og tilstedeværelsen av vann undersøkt, for å kunne konkludere rundt, aktiviteten i reelle eksosforhold. Alle katalysatorer ble syntetisert med samutfellingsmetoden, og palladium ble avsatt på overflaten med impregnering. Katalysatorene ble karakterisert med XRD, N_2 physisorption, XRF, Raman spektroskopi og TEM.

Det ble funnet at blandende oksider av nikkel og kobolt viste høy aktivitet for metan oksidasjon ved relativt lave temperaturer, tross et reversibelt tap av aktivitet ved tilstedeværelse av vann. Kinetiske undersøkelser indikerte at addisjon av vann til føden mulig endret den kinetiske modellen i systemet. De blandede oksidene viste begrenset avhengighet av nikkel-kobolt forholdet i katalysatoren. Katalysatorene som ble undersøkt med denne hensikten, viste lignende aktiveringsenergi- og reaksjonsrateverdier av rimelige størrelser, som ble tilnærmet med en kinetisk modell som var av antatt å være av første orden i metan og i nulte orden i oksygen. Videre ble det observert at katalysatorene undergikk strukturelle endringer under første reaksjonssyklus ved fersk katalysator. Palladium forbedret aktiviteten betydelig, mulig grunnet den høye dispersjonen av Pd som ble oppnådd, og/eller en synergisk effekt mellom Pd og det blandede oksidet. Basert på den kinetiske undersøkelsen, var det mulig at palladiumkatalysatoren fulgte den antatte modellen bedre enn de blandede oksidene. Generelt viste blandede oksider av nikkel og kobolt lovende potensial for etterbehandling av eksos fra NG fartøy.

Contents

Abbreviations

AFR	Air-to-Fuel ratio
BET isotherm	Isotherm of Brunauer, Emmett and Teller
BJH method	The Barret-Joyned-Halenda method
BF	Bright Field
CNG	Compressed natural gas
ECD	Electron capture detector
EDXS	Energy dispersive x-ray spectroscopy
FID	Flame ionization detector
GC	Gas chromatography
HAADF	High angle annular dark field
HFO	Heavy fuel oil
HRTEM	High resolution transmission electron microscopy
IWI	Incipient wetness impregnation
LH	Langmuir-Hinshelwood mechanism
LNG	Liquefied natural gas
MFC	Mass flow controller
MvK	Mars-van-Krevelen mechanism
MT16	Master thesis 2016, refering to measurements reportet by Helene Sandvik.
NG	Natural gas
NGV	Natural gas vehicle
NTNU	Norwegian University of Science and Technology
PLOT MS Column	Porous layer open tubular molsieve column
RT	Room temperature
TCD	Thermal conductivity detector
$\mathbf{T}_{10}$	Temperature at 10% methane conversion
$\mathbf{T}_{50}$	Temperature at 50% methane conversion
$\mathbf{T}_{90}$	Temperature at 90% methane conversion
TEM	Transmission electron microscopy

STEM	Scanning transmission electron microscopy
SEM	Scanning electron microscopy
XRD	X-ray diffraction
XRF	X-ray fluorescence
CH_4	Methane
H_2O	Water
KOH	Potassium hydroxide
N_2	Nitrogen
$NiCo_2O_4$	Nickel dicobalt oxide, Batch 1 of catalyst
$NiCoO_4$	Nickel cobalt oxide with 1:1 ratio of Ni and Co, Batch 2 of catalyst
$Ni_{0,75}Co_{2.25}O_4$	Nickel cobalt oxide with 1:3 ratio of Ni and Co, Batch 3 of catalyst
$NiCo_2O_{4-550°C}$	Nickel dicobalt oxide, calcined at 350°C, Batch 4 of catalyst
$NiCo_2O_{4-550°C}$	Nickel dicobalt oxide, calcined at 550°C, Batch 5 of catalyst
O_2	Oxygen
Pd	Palladium
PdO	Palladium Oxide
0,5wt%Pd/$NiCo_2O_4$	0,5 weight percent Pd deposited on $NiCo_2O_4$, Batch 6 of catalyst
Pt	Platinum
2%	Reactant feed comprising 2% CH_4, 10% O_2 and balance N_2
0,5%	Reactant feed comprising 0,5% CH_4, 10% O_2 and balance N_2
0,1%	Reactant feed comprising 0,1% CH_4, 10% O_2 and balance N_2
0,1%$_{H_2O}$	Reactant feed comprising 0,1% CH_4, 15% H_2O, 10% O_2 and balance N_2

List of Symbols

α	Constant $\frac{\chi-1}{\chi V_0}$	mm^{-3}
β	Peak width	rad
η	Constant $\frac{1}{\chi V_0}$	mm^{-3}
θ	Angle of diffraction	$^\circ$
λ	Air-fuel equvalence ratio	-
λ	Wavelenght of X-rays	nm
ρ	Density	$\mathrm{kg\,m}^{-3}$
τ	Residence time	s
χ	Ratio of desorption rate	-
A	Pre exponential factor	-
A_i	Peak area of component i	nm^2
A_M	Occupation are of one molecule	$\mathrm{nm}^2\,\mathrm{molecule}^{-1}$
A_T	Total surface area	nm^2
C_A	Concentration of component A	$\mathrm{mol\,L}^{-1}$
C_{A0}	Initial concentration of A	$\mathrm{mol\,L}^{-1}$
d	Lattice spacing	Å
E_C	Error over carbon	%
E_A	Activation energy	$\mathrm{kJ\,mol}^{-1}$
F_i	Flow rate of component i	$\mathrm{mol\,s}^{-1}$
F_{tot}	Total flow rate	$\mathrm{mol\,s}^{-1}$
GHSV	Gash hourly space velocity	$\mathrm{NmL\,h}^{-1}\,\mathrm{g}_{\mathrm{cat}}^{-1}$
h	Height of catalyst bed	cm
ΔH_f^0	Heat of formation	$\mathrm{kJ\,mol}^{-1}$
k	Rate constant	s^{-1}
K	Scherrer's constant	-
k_B	Boltzmann's constant	$\mathrm{J\,K}^{-1}$
k_i	Response factor of component i	nm^{-1}
L	Length og particle diameter	nm
M	Molarity	$\mathrm{mol\,L}^{-1}$
Mm	Molecular weight	$\mathrm{g\,mol}^{-1}$
m	Mass	g
n	Order of diffraction	-

n_i	Mol of component i	mol
P	Pressure	Bar
P_0	Partial pressure of condensed gas	Bar
q	Volumetic flow rate	$\mathrm{NmL\,min^{-1}}$
r	Reaction rate	$\mathrm{mol\,g_{cat}^{-1}\,h^{-1}}$
r_{Pd}	Reaction rate per gram Pd	$\mathrm{mol\,g_{Pd}^{-1}\,h^{-1}}$
S_{BET}	Specific surface area	$\mathrm{m^2\,g_{cat}^{-1}}$
T	Temperature	K
V	Volume	$\mathrm{cm^3}$
V_0	Volume of adsorbed molecules first layer	$\mathrm{mm^3}$
V_a	Total volume adsorbed molecules	$\mathrm{mm^3}$
V_R	Reactor volume	$\mathrm{cm^3}$
V_P	Pore volume	$\mathrm{cm^3\,g_{cat}^{-1}}$
X	Conversion	%
y_i	Mole fraction of i in gas phase	-

List of Figures

List of Tables

Chapter 1

Introduction

1.1 Motivation

The interest for utilization of natural gas (NG) as an energy source is increasing in industrial countries world wide, with a dual motivation. The world reservoirs of NG exceed those of oil by extent, and efficient application of NG to the energy sector is increasing as governments strive to diversify their energy sources. In addition, the climate threat is a heavy on leading countries, and new emission regulations and constraints are continuously being demanded by all industries. The marine industry has lately been identified as a large contributor to greenhouse gas emissions, and governments worldwide have initiated regulations for abatement of emissions originating from this sector. Natural gas vehicles (NGVs) have been suggested as an alternative to traditional marine vessels, which conventionally run on heavy fuel oil (HFO). Conventional fuels are based on long hydrocarbon chains, which display a low hydrogen to carbon (H:C) ratio, with inbound species of nitrogen and sulphur. Consequently, traditional marine vehicles contribute to high CO_2-, NO_x- and SO_x-emissions. NGVs allow for exploitation of natural gas, mainly comprised of methane, according to the reaction equation, [1]:

$$CH_4 + 2O_2 \rightarrow CO_2 + 2H_2O \qquad \Delta H_f^0 = -802,3 \text{kJ mol}^{-1}$$

All NGs are dominated by methane, at a level of approximately 85-95%. Due to the high H:C ratio in the NG mixture, the CO_2 emissions are reduced considerably, in comparison to conventional fuels. In addition to decreasing the CO_2 emissions, NGV combustion can operate under lean conditions, which reduce the formation of thermal NO_x. Further, NGs have low content of particulates, and nitrogen- and sulfur species, which leads to a relatively clean exhaust gas. The latter motivates the utilization of NGVs also in urban areas, where air quality is an important issue, [1].

The environmental advantages of NGV employment are however partly counterbalanced by methane slip in the exhaust gas. Fractions of unoxidized methane from the combustion chamber, counteract the environmental benefits due to the nature of the methane molecule. According to the Kyoto protocol, methane displays a global warming potential (GWP) 21 times

greater than that of CO_2 over a time horizon of 100 years. The molecule has a lifetime in the atmosphere from 9 to 15 years, [2]. Methane abatement from the NGV exhaust gas is thus necessary to ensure environmental advantages from using NGVs in the marine sector.

There are different alternatives to facilitate methane abatement from NG combustion. At increased temperature and pressure, complete methane combustion occur, however the methane abatement is a trade off with formation of thermal NO_x. Under such conditions the temperature increases to above the thermal NO_x limit of 1300°C. Due to the high exothermicity of the reaction, the combustion temperature can easily go out of control. First, this leads to risky reaction conditions. Second, although it may no longer be necessary to removal methane from the exhaust gas, it must be treated to remove NO_x. It may therefore be more advantageous to keep the reaction conditions at lower temperature, by facilitating lean methane combustion, and rather treat the exhaust gas for methane slip by complete catalytic oxidation, [3].

Several catalysts have been investigated to overcome the obstacles presented by the reaction conditions for complete catalytic oxidation of methane. The catalytic material must show high activity at low temperatures (normally below 550°C) and for diluted concentrations of methane. In addition, the catalyst must withstand the composition of the exhaust gas, which contains high amounts of water vapor and CO_2. Supported noble metal catalysts (especially palladium supported on alumina) have been identified to have superior properties for the reaction. However, due to the high price and limited availability of precious metals, in addition to the decreased reaction rate in presence of water, further research for alternative materials is needed, [1].

1.2 Objective

The objective of this Master thesis is to investigate transition metal oxides comprised of cobalt and nickel for low temperature catalytic methane oxidation. The dependency of catalytic activity on oxide composition, catalyst preparation and deposition of a small fraction of noble metal will be investigated. The synthesized catalysts will be characterized using some of the main techniques, to obtain information about the catalytic material. Further, the catalyst activities will be investigated in reactant gases of low methane concentrations at lean conditions. The catalytic actvity in realistic exhaust conditions will also be tested, with addition of water to the reactant gas.

1.3 Method

This Master thesis is written as an addition to the research project EmX2025, which is an R&D base for reduced exhaust greenhouse gas emissions from the Norwegian marine transportation sector. The thesis is a continuation of the specialization project conducted the autumn 2016 regarding the same topic, and research material produced during this project is thus presented in the thesis. This will be marked accordingly, where it is applicable. The research project has been subject to two prior Master theses from the department, which regarded noble metal based catalysts. It was thus found to be of interest to compare the results obtained in the present research with those reported by Sandvik and Storvik, who respectively studied supported palladium- and platinum catalysts, [4] and [5].

The scientific methods of the research were derived by the author, in agreement with and with guidance by the master supervisors. All lab work (apart from TEM) were executed independently, though the supervisors and scientific staff contributed to apparatus training and troubleshooting along the experimental timeline. The methods of characterization and activity conditions were outlined along the timeline. For instance, when the stoichiometrically different catalysts showed little dependency on catalytic activity, it was found to be of higher interest to investigate the activity under realistic exhaust conditions. The literature was then reviewed to establish if study of water or CO_2 addition to the reactant feed should be prioritized. Further, as the literature reviled limitation over palladium based catalysts in wet conditions, it was interesting to observe if palladium deposited onto the active mixed oxide would experience similar effects to the undeposited support.

The literature research conducted for the theoretical background of the thesis was mostly done by conducting abstract research in several scientific article databases, and by exploring the references from relevant articles and theses. The obtained results from the conducted research were discussed with basis on discovered literature, although this was somewhat challenging as mixed oxides of nickel and cobalt are mainly studied for their electrochemical properties. The literature base on the relevant material for the present topic was found to be limited.

Chapter 2

Theory

2.1 Natural Gas as Fuel

There are large stranded resources of methane globally, which means it is not integrated into pipeline infrastructure. By transforming NG to more a compact and energy dense state, such as liquefied natural gas (LNG) or compressed natural gas (CNG), the resource can more easily be utilized on mobile vessels, for example in the marine industry. Historically LNG was produced simply to decrease the volume of the NG, as it was moved from stranded areas to areas connected to pipeline infrastructure. Lately, however, the use of LNG directly as transportation fuel has catalyzed a shift from conventional fuels globally. Norway is in a unique position in this transition, with more than 50 operative LNG fueled ships in 2015, [6].

In addition to the environmental benefits of LNG utilization mentioned introductory, one provident advantage of utilizing transport vehicles with CNG and LNG engines is that the engines can easily be fueled by compressed or liquefied biogas (CBG/LBG), or mixed biogas and NG. Energy diversity an important aspect for developed governments, and the ability to accept fuel from different energy sources is an additional motivation for NGV application [7]. However, this transitions demands much upgrading of the biogas, to meet the necessary requirements for liquefaction. Impurities, such as N- or S-species are removed prior to liquefaction because they damage the liquefaction process. Compressed gas may contain small amounts of impurities, although impurities from CNG or CBG fuels may entail NOx or SOx production in the engine. It is important to note that the topic of this thesis, methane abatement from LNG exhaust, is relevant regardless of the origin of the fuel gas. Although the carbon species in biogas have the potential of being carbon neutral, the high global warming potential of methane entails that emission to the atmosphere should be eliminated. Correspondingly, NOx and SOx have the same pollutive effect if the gases originate from fossil fuels or from bio fuels, [8].

NG engines are tuned to operate in a certain way that increase temperature control of the highly exothermic reaction in order to minimize the NOx fraction in the exhaust gas. The operation could be tuned to minimize the methane fraction studied in the present work, but this would result in NOx formation. Historically, NOx emissions have been subject to more political

controversy, which have governed the present design of NG engines. These engines operate under lean conditions, which decrease the formation of thermal NO_x during combustion and increase the efficiency of the engine. NO_x formation is favoured at high temperatures (T> 1300°C), and the formation is thus limited due to the cooler operating temperature resulting form the high air-to-fuel ratio. NG also contains low amounts of sulphur, and the formation of SO_x compounds is thereby limited. The lack of SOx in LNG exhaust gas contributes to increased energy efficiency, because waste heat can be exploited from the exhaust without corrosion issues originating from high SOx content [9]. The 1999 Gothenburg protocol assessed methods to decrease release of pollutants such as SOx, NOx, VOCs and particular matter from industry [10]. On the basis of these pollutants, LNG vehicles offer a significant improvement compared to HFOs. Lately, however, coherent with increased awareness of global the attention to carbon species emissions has increased, culminating in the Paris Agreement signed by 194 countries, including Norway, in December 2015. The Paris Agreement aims to unite the world's nations with the common goal to limit global warming to below 2°C [11].

In an assessment performed by DNV-GL for the Norwegian Ministry of Climate and Environment, it is reported that the transition from conventional fuels to LNG can reduce total emissions of greenhouse gases from the marine transport in national waters by approximately 20%. By coupling future investments made in bunkering and storage with solutions compatible with bio gas, the environmental gain can be even higher [12]. The report states that the highly developed state of LNG engine technology allows it to function as a transition technology, while further developments are made in zero-emission technologies, such as full-electric and fuel cell vessels. It is expected that further technological advances must be made before full electric vessels can operate at open waters, and NG is thus an alternative fuel with lighter climate footprint compared to HFO. The climate gas reduction would, however, be even higher by use of catalysis for methane abatement. The time horizon of the transition to a international zero-emission marine fleet is long, as ships usually have an expected lifetime for at least 40 years. By development of an effective catalytic after-treatment system for methane abatement, the technology could likely be applied to ships fueled by LNG that are already operative.

Methane is the hydrocarbon that is hardest to activate, and the high stability of the molecule makes the conditions for catalytic NGV exhaust gas after treatment more challenging than the technology applied to other hydrocarbons. The additional obstacles for lean-burn NGV exhaust gas after treatment were summarized by Gélin and Primet (2002) [1]:

- The catalyst must operate at low temperatures, typically less than 500-550°C.
- The catalyst must operate at dilute reactant concentrations, typically 500-1000 ppm methane.
- Presence of large amounts of water vapor, 10-15%, and CO_2, 15%, in the reactant gas.

- Presence of SO_x, about 1 ppm, and, depending on the engine used, the possibility of NO_x in the reactant gas (NGVs in Norway does not emit NOx.

It has been identified that the catalyst design must focus on high low temperature activity and poison resistance, as the lean-burn conditions rules out the concern of the thermal stability of the material. The requirement for lean-burn combustion are [8]:

$$\lambda >> 1 \tag{2.1}$$

where λ is the air-fuel equivalence ratio, presented in Equation 2.2.

$$\lambda = \frac{\text{AFR}}{\text{AFR}_{Stoic}} \tag{2.2}$$

In the above equation, AFR is the air-to-fuel ratio in a reaction. AFR_{stoic} is the stoichiometric air-to-fuel ratio, given for methane combustion in Equation 2.3.

$$\text{AFR}_{stoic} = \frac{n_{air}}{n_{fuel}} = 2 \tag{2.3}$$

When operating at stoichiometric conditions AFR=AFR_{stoic}, and thus $\lambda = 1$.

2.2 Catalysts for Methane Oxidation

The requirements for successful catalytic combustion of methane from natural gas exhaust have been summarized above. In addition to these specifications, the catalyst must be able to endure temporal changes in the reactant feed composition. Due to the nature of NG, the exhaust gas may change composition depending on factors such as the composition of the NG or on different levels of engine fire power, as these may influence the magnitude of methane slip.

2.2.1 Noble Metal Catalysts

Noble metal catalysts have been extensively studied as suitable materials for complete catalytic oxidation of methane. Platinum (Pt) and palladium (Pd) are among the two most studied materials for this application, and they have shown superior catalytic activity to any other material so far [1]. Supported on a high surface area material, such as alumina, they can obtain a high degree of dispersion, which helps to improve their catalytic activity. In an environment

where there is O_2 abundance, palladium has been shown to possess the highest activity of the two, much due to the maintained activity towards methane oxidation for oxidized palladium, PdO [1]. The relationship of activity between Pd and PdO has been widely studied and debated, and there is consensus that both phases are active for methane conversion. However, presence of water and sulphur containing compounds in the reactant gas poses a big drawback to the activity. NGV emission gas usually contains a large fraction of water vapor, and if exhaust treatment occurs directly after the combustion chamber, the catalyst needs to withstand this parameter over a long time on stream, [1]. Bimetallic systems, catalysts comprising both Pd and Pt have been shown to improve the deactivation of both palladium and platinum, compared to the respective monometallic materials, [13]. However, precious metals are pricey materials with limited availability, which lowers commercial interest for large scale industrial application. This has motivated researchers to develop a catalytic material comprised of cheaper and more available components, [14].

2.2.2 Metal Oxide Catalysts

Metal oxides, primarily consisting of transition metals, are interesting materials for catalytic oxidation, due to their d-band electron vacancy. Transition metals can obtain multiple valence states, allowing them to exist in several oxidation states. They can alternate between high and low oxidation states, allowing lattice oxygen to be stored and released during the redox cycle [13]. In addition, they are available in abundant raw materials at significantly lower prices than noble metals, [15]. Several families of metal oxides have been studied for methane oxidation applications, both single metal oxides and mixed metal oxides. For instance CuO and several variations of CeO_2 such as Ce_xNi_yO, have been shown to display high activity for methane oxidation. Mixed metal oxides contains structures such as perovskites, spinels and hexaaluminates, [13].

Spinel oxides are mixed metal oxides with the general formula AB_2O_4. Normally A is a divalent cation occupying tetrahedral sites, and B is a trivalent cation in octahedral sites, as illustraded in Figure 2.1. However, spinels may occur as inverse variants with opposite features, or as intermediates where fractions of both metals occupy both sites, [16]. According to *Recent Advances in Catalysts for Methane Combustion*; an extensive review of recent research on different heterogeneous catalysts for methane oxidation written by Chen et al (2015, [13]), spinel oxides are a promising candidate for low-temperature methane oxidation. So far, however, these materials have been subject to little research.

Tao et al. report that at low temperatures, spinel oxides composed of nickel and cobalt exhibit higher activity for catalytic methane oxidation than noble metal based catalysts. Although the path of reaction over metal oxides can be difficult to identify, they suggest that the oxida-

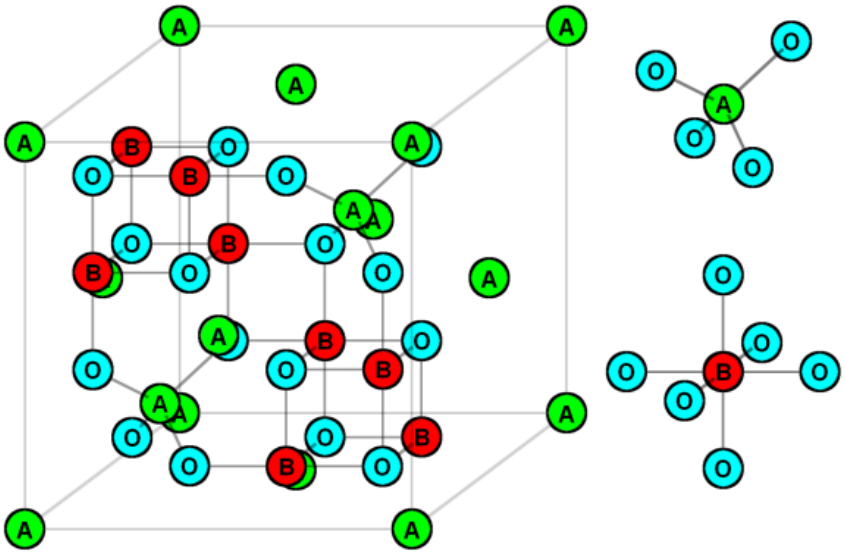

Figure 2.1: An illustration of the half front of the unit cell of a spinel oxide on the form AB_2O_4. A^{2+} cations occupy tetrahedral sites, and are bonded to four oxygen atoms. B^{3+} cations occupy octahedral sites, and are bonded to six oxygen atoms. The figure is obtained from [17] (2011, p. 12).

tion of methane occurs by initial dissociation of methane to methyl on nickel cations, which is further coupled with surface lattice oxygen to form $-CH_3O$. Further dehydrogenation and oxidative dehydrogenation transforms the transition states to product molecules, [14]. Chen et al. suggest that the combustion of methane over spinels occur by two possible mechanisms, the suprafacial and intrafacial, depending on the origin of the oxygen atom that participates in the oxidation. The suprafacial mechanism is believed to occur at relatively low temperatures, with the oxidizing atom originating from the gas phase. In the latter mechanism, oxygen from the bulk material becomes available for reaction by migrating to the surface. If it undergoes reaction, the oxygen vacancy is rapidly filled by oxygen from the gaseous phase. This is the principle of the Mars-Van-Krevelen mechanism, and the mechanism is believed to be efficient at higher temperatures, [13].

Pu et al (2017 [18]) report that the activity of Co_3O_4 for methane oxidation is dependent on the abundance of Co^{2+} cations occupying in the tetrahedral sites in the spinel structure. With this basis, the activity of $NiCo_2O_3$ is mostly governed by the cobalt fraction of the spinel. The high activity reported by Tao et al, is contradictory to the research reported by Lim et al (2015 [19]) that report that palladium based catalysts display higher activity that mixed ocides of nickel and cobalt. Lim et al further report that the activity of methane conversion is dependent on the ratio between nickel and cobalt within $NiCo_2O_4$, and the catalyst with most provident catalyst

displayed a 1:1 ratio of nickel and cobalt.

2.3 Catalyst Synthesis

2.3.1 Coprecipitation

Coprecipitation is a synthesis method that allow for several precursor compounds to be deposited together in a single process. In coprecipitation the precursors are precipitated from a highly supersaturated solution of the precursor compounds as hydroxide crystallites. Supersaturation occurs, for example, by increased pH of the solution, which is facilitated by addition of a precipitating agent. The conditions should be tuned carefully to ensure that both metals are precipitated throughout the process. Additionally the solution must be kept as homogeneous as possible, with no gradients over the solution. Constant mixing should thus be applied during the coprecipitation step. The coprecipitation method is considered to be a more difficult method than the much applied impregnation method presented in the next section. Both methods are applied industrially, although coprecipitation requires higher control of process conditions and more costly equipment. This is due to the range of material qualities that are contrived during the process, such as pore structure, particle size, shape, surface area and dispersion. The process conditions, such as stirring, mixing, temperature, ingredients and method of dosing, have strong influence on the final product, [20]. After precipitation, the product is a homogeneous mixture of hydroxide metal salts, which must be separated from the residue, usually by filtering. At industrial scale this may be a drawback of the method. [21].

To obtain the active catalyst, the precipitate must be dried and calcined at appropriate temperature. The last step, if conducted at correct temperature, ensures removal of inbound species that could be present from the precipitation process, such as nitrates originating from the precursor compounds. The calcination yields a porous catalytic material, [21].

2.3.2 Incipient Wetness Impregnation

Incipient wetness impregnation (IWI) is a method of depositing an active component to a support, [21]. The obtained load and distribution of the active component is governed by three steps during the preparation; the impregnation (illustrated in Figure 2.2), the drying (illustrated in Figure 2.3) and the calcination.

The impregnation step is based on capillary forces pulling a solution containing the precursor of the desired active component into the pores of the support material. If a support with pore volume V_P is mixed with a precursor solution with volume $V = V_P$, the liquid is pulled into the

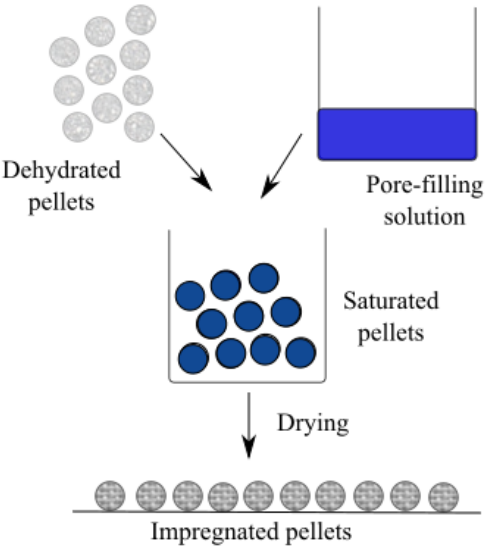

Figure 2.2: Illustration of steps in incipient wetness impregnation, adapted from page 116, [22]. The figure is made in Inkscape.

cavities by capillary forces. If the impregnation is done correctly, no excess liquid will remain on the surface of the support. Incipient wetness impregnation is therefore also called "dry" impregnation [23]. The sufficient amount of solution can be calculated from characterization techniques providing pore volume (such as N_2 physisorption, 2.4.2), however such techniques may be uncertain. A more reliable method may thus be to find the amount empirically by dripping a solvent, usually water, on the support until it reaches saturation, and taking note of the sufficient volume, [22].

The drying step ensures the crystallization of the metal salt onto the pore surface. Upon drying, the water is eliminated from the pore, thereby increasing the saturation of the precursor compounds in the aqueous phase to the point of crystallization, [23]. The rate of drying is important to gain an even and regular distribution of the active component within the pore. The ideal drying rate is identified when there is an even and regular concentration distribution of the active component, as illustrated in Figure 2.3**b)**. If the drying rate is too slow, the evaporation from the pores occurs on the meniscus of the solvent, which migrates to the depth of the pore. Upon complete drying, most of the salt crystallizes at the bottom of the pore. This results in a "egg-yolk" distribution of the active material, which is illustrated in Figure 2.3**a)**. For the opposite case, if the drying rate is too fast, the evaporation is driven from within the pore. The active component is crystallized at the pore opening, resulting in a "egg shell" distribution, as

illustrated in Figure 2.3**c)**, [22]. The ideal drying rate, which is not too fast and not too slow, can be difficult to determine, but information may be obtained from previous research.

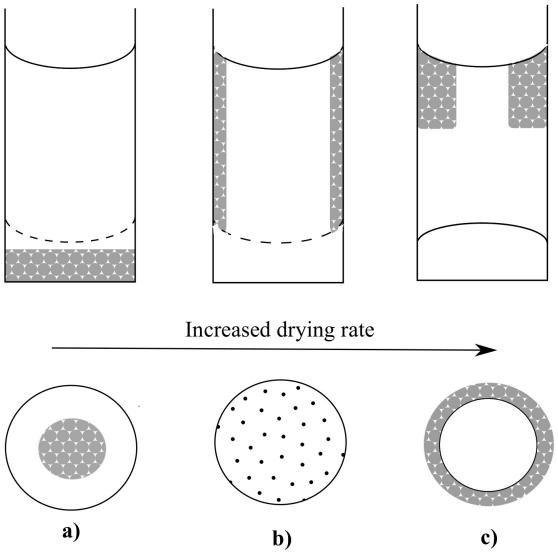

Figure 2.3: Illustration of the dependency of drying rate on the particle distribution. In **a)** the drying rate is too slow, resulting in an "egg-yolk" distribution and in **c)** the drying rate is too fast, resulting in an "eqq-shell" particle distribution. **b)** represents an ideal drying rate, with uniform distribution of deposited particles. The figure is adapted from page 116 in [22], and is made with Inkscape.

If the surface of the support possess electrostatic character, interactions between the surface and the precursor can contribute to enhanced dispersion of the active component. If certain groups on the surface of the support are oppositely charged to the precursor compounds, they can function as an anchoring site for the precursor [21]. Su et al. (2015 [24]) report that the surface of $NiCo_2O_4$ spinel may be hydroxylated to some extent. The hydroxyl groups can attain ionic character when they are wet, as they react with protons or OH^- groups. In this case, interaction between hydroxyl groups and the Pd-precursor, may facilitate enhanced dispersion of palladium, if they are oppositely charged. The pH of the solvent can further be used to manipulate such interactions, by altering the surface charge.

The final step of the impregnation is the calcination, which converts the crystallized precursor salt into a metal or metal oxide. The calcination step prevents the crystallized salts to redissolve if they are exposed to humid environments.

2.4 Catalyst Characterization

2.4.1 X-ray Diffraction

X-ray diffraction (XRD) is a method to identify crystalline phases in the material bulk, and to gain information about the crystallite size of the material. It is one of the most widely used characterization techniques for solid materials. A catalyst may contain several phases that can affect the catalytic activity differently. In XRD, incoming X-rays are scattered elastically by atoms in a periodic lattice, which gives constructive interference if the photons are in phase, as illustrated in Figure 2.4. The conditions for constructive interference is given by the Braggs relation, presented in Equation 2.4. If the diffraction of X-rays by crystal planes are applied to the Bragg equation, the lattice spacings in the crystal can be derived, [21] and [25].

$$n\lambda = 2d\sin\theta, \qquad n = 1,2,... \tag{2.4}$$

In the above equation λ is the wavelength of X-rays, d is the distance between two lattice planes, θ is the angle between incoming X-rays and the reflecting lattice normal and n is the order of reflection, [21].

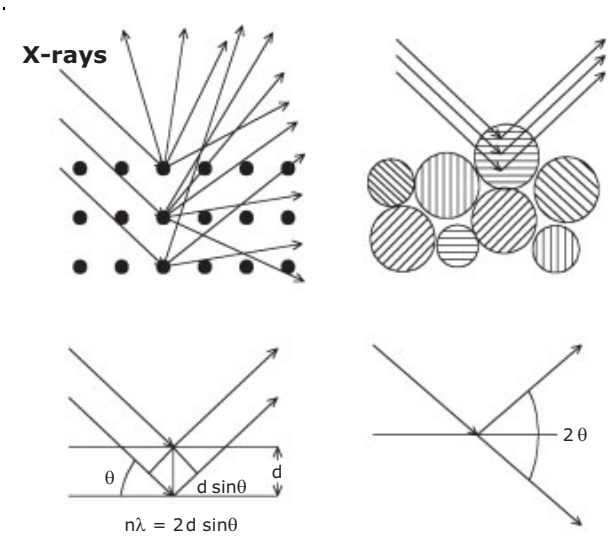

Figure 2.4: An illustration of constructive interference of scattered x-rays, given by Bragg's law in Equation 2.4. In a powder sample the diffraction pattern is provided by a small part of the sample. By rotating the sample (or the incident x-rays), the contribution to the diffraction pattern is improved by increasing the amount of participating particles. The figure is obtained from, [21] (p.132) .

The diffracted beams of an x-ray can be described by the Ewald sphere in the reciprocal space,

which in fact is a 3D diffraction pattern. By changing the angle of the incident x-ray, θ, all lattice spacings of many randomly oriented crystals (such as in powders) can be obtained along one direction [26]. Every compound will achieve a unique diffraction pattern, as the angles of diffraction differ for the various planes and atoms within a crystal. As all phases have unique planes and spacing of the atoms, the diffractogram will provide a "fingerprint" of crystalline phases present in the analyzed sample. However, for short-range ordered samples, clear diffraction peaks may be hard to obtain due to the limitations of the method. XRD will only provide clear peaks for sufficiently long-ranged ordered samples. Perfect crystals will provide sharp and narrow diffraction peaks, indicating large particles and crystallite sizes. For smaller crystallite sizes, the number of lattice planes becomes limited, and the clear distinction between constructive and destructive interference fades, [25]. In such an event, the Bragg peak will include a small range of diffraction angles, and the diffraction peak will appear broader, than for larger crystallites. This relation is quantified in the Scherrer formula given in Equation 2.5,

$$L = \frac{K\lambda}{\beta \cos\theta} \tag{2.5}$$

where L is the particle diameter, β is the peak width and K is a constant, [21].

Although XRD provides relatively clear information about a particle above a certain size, it fails to identify amorphous phases, and small particles may go undetected. Materials should have crystallite sizes above 2nm for clear information from XRD to be obtained. An XRD spectrum may thus not give complete information of all the phases present in a sample. Catalytic reactions occur on the surface of the catalyst, which may differ significantly from the bulk material. As information about the surface is unattainable with XRD, the technique should be coupled with other characterization methods to gain adequate information of a catalytic material.

2.4.2 N_2 Physisorption

Nitrogen adsorption and desorption is a method that allows for analysis of internal surface area and pore volume of a material.

A heterogeneous catalyzed reaction occurs at the surface of the active material. To facilitate a high reaction rate per catalyst mass it is thus beneficial to have a large surface area, in most cases. By performing physisorption of an inert gas, such as N_2, to the surface of a material one can determine the amount of molecules necessary to cover the surface. Knowing the occupation area of one molecule of N_2 (A_M=0.162 nm^2 at liquid N_2 temperature 77 K), the surface area of the material can be calculated. The method is based on the formation of multilayer physisorp-

tion of N_2, at the point of N_2 condensation in small pores. The latter is utilized to determine the pore volume and size distribution of the system, [21].

The theoretical derivation of calculating internal surface area with N_2 physisorption is based on the isotherm of Brunauer, Emmett and Teller, the BET isotherm. An adsorption isotherm represents the dependency of the adsorbed gas on the equilibrium pressure of the gas at constant temperature. The formation of the monolayer in the BET isotherm is assumed to follow the Langmuir isotherm. As the partial pressure of N_2 increase, the surface will fill gradually until it reaches a plateau, indicated by point B in Figure 2.5. At this point, the surface is completely covered with adsorbates. At higher pressures the BET isotherm deviates from the Langmuir isotherm, by formation of new layers. Depending on the morphology of the surface, different types of BET isotherms appear. Figure 2.5 illustrates a Type IV BET isotherm, which is typical for a porous material. For a porous material, N_2 will adsorb and desorb at different relative pressures as the relative pressure approaches 1, due to capillary condensation within the pore structures. The multilayer adsorption will be limited by the filling of the pore, and upon desorption capillary forces must be overcome before gas evacuation occur. Thus the hysteresis illustrated in Figure 2.5 can be observed. This hysteresis can provide information about the pore volume and distribution if applied to Barret-Joyned-Halenda analysis (the BJH-method), [21].

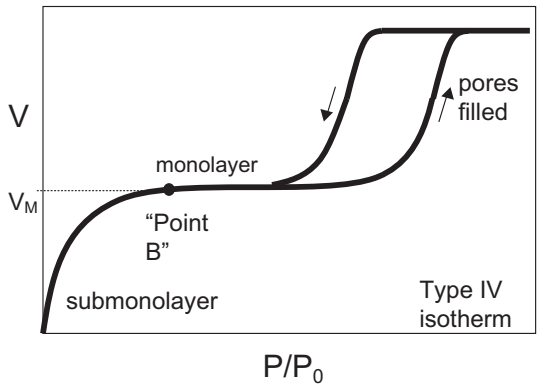

Figure 2.5: An illustration of a Type IV BET isotherm, typical for a mesoporous material. Point B indicates the completion of a monolayer on the surface, and the consecutive hysteresis is due to capillary condensation within the pores of the material. The figure is obtained from [21] (p.190).

Although the BET method is widely used and renowned, it contains limitations that should be assessed upon its application. The fundamental assumptions for the BET isotherm are, [21]:

- Adsorbate and adsorptive are in dynamic equilibrium, the rate of adsorption and desorption are equal in any layer.

- Molecules adsorb on equivalent adsorption sites in the first layer.
- Adsorbed molecules represent the adsorption site for consecutive layers.
- Interactions between adsorbates within a layer are ignored.
- The heat of adsorption and desorption are the same in all layers, except the first.
- The condensation energy equals the adsorption energy for molecules in the second layer and higher.
- At saturation pressure ($P = P_0$), the multilayer grows to infinite thickness, meaning that the N_2 condensate to liquid.

To apply the BET method with N_2 physisorption successfully, the surface area of the catalyst should exceed 1 or 2 $\frac{m^2}{g}$. For micro porous materials mono- and multilayer formations are prevented, and the BET method should not be used. In addition, the assumption of constant packing of N_2 molecules might be hard to obtain in realistic systems. However, other molecules, such as Krypton, can be used for systems with smaller pore volume.

The BET isotherm is given by

$$\frac{P}{V_a(P_0 - P)} = \frac{1}{\chi V_0} + \frac{(\chi - 1)}{\chi V_0}\frac{P}{P_0} \equiv \eta + \alpha\frac{P}{P_0} \tag{2.6}$$

where V_a is the total volume of adsorbed molecules, V_0 is the volume of adsorbed molecules in the first layer, χ is the ratio of the desorption rate constants for the second and first layers, P is the pressure and P_0 is the partial pressure of condensed gas, [21].

V_0 can be found by plotting $\frac{P}{V_a(P_0-P)}$ against $\frac{P}{P_0}$, which yields a straight line with slope $\alpha = \frac{(\chi-1)}{\chi V_0}$ with x-axis intersection at $\eta = \frac{1}{\chi V_0}$. The total number of molecules adsorbed in the first layer, N_0, can be found by solving $N_0 = \frac{PV_0}{k_B T}$, where k_B is Bolztmann's constant. Knowing the area each molecule occupies, A_M (0.162 nm^2 at liquid N_2 temperature 77 K), the total surface area can be calculated, $A_T = N_0 A_M$.

2.4.3 X-ray Fluorescence

X-ray fluorescence (XRF) is a technique which can be utilized to determine the composition in a sample. The method gives both quantitative and qualitative information about the individual species within the analyzed sample.

The foundation of the principle is based on the emission caused by an atom's behavior upon X-ray radiation. If the excitation radiation is larger than the binding energy of an electron in

the inner atom orbital, the electron can be ejected from the atom upon collision. The atom is thus ionized with a vacancy in the inner electron orbital. The atom is highly unstable in this state, and two subsequent paths may occur to counteract the destabilization, as illustrated in Figure 2.6. The energy can be liberated by emitting an electron from the atom orbital, called an Auger electron. This concept is utilized in Auger electron spectroscopy. However, if the vacancy if filled by an electron from an outer electron orbital, the atom will emit a characteristic X-ray photon, with energy equal to the energy difference between the inner and the outer electron orbital, [27]. The two possible effects are competitive, and the probability of X-ray emission occurring is called the fluorescence yield. XRF have low sensitivity to elements below atomic number 11 (Na), due to the low fluorescence yield of light elements, [27] and [28].

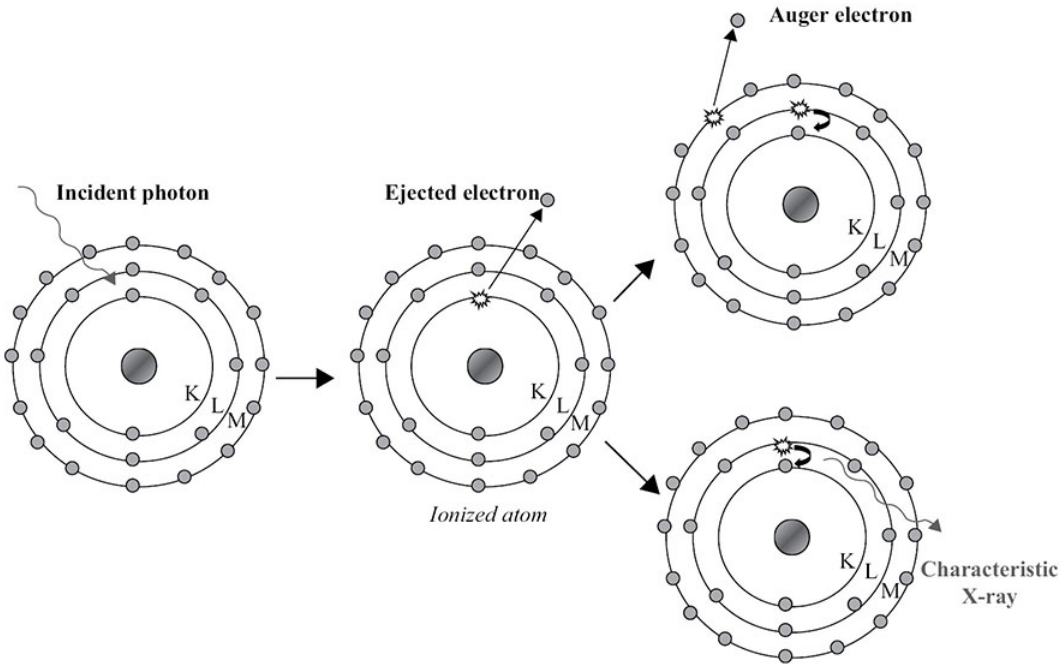

Figure 2.6: X-ray radiation generates either X-ray Fluorescence or the release of an Auger electron, if the excitation source is greater than the binding energy of the inner orbital electrons. The figure is obtained from *X-Ray Fluorescence Spectrometry and Related Techniques: An Introduction* (2013, Margui and Grieken), [27].

The X-ray photon emitted upon radiation is characteristic to every element on the periodic table. The atoms present in a sample can thus easily be determined using XRF. By investigating the intensity of the characteristic emissions, the concentration of a specific atom can also be determined, [27] and [29].

The basic components of an XRF spectrometer are an excitation source, a sample chamber, a detection system and a system for signal processing and data collection. The most common

radiation source used commercially is X-ray tubes, which generates a continuous stream of X-ray photons to the sample, [27].

2.4.4 Raman Spectroscopy

Raman Spectroscopy is a useful method to gain information such as crystallinity and coordination of metal oxide sites from metal oxide catalysts. The frequencies of the stretch vibrations of metal-oxygen bands usually range between 100-1000 cm^-1 [30].

Raman active vibration requires that the molecule changes its shape during the vibration. As illustrated in Figure 2.7 an exited electron can give two types of scattering. In Rayleigh scattering, illustrated in Figure 2.7**(b)** the incident photon excites an electron from an initial vibrational energy level of a molecule to an intermediate vibrational state, before it transitions back to the original energy level. This concept is also named elastic scattering, and occurs without any energy exchange between the molecule and the photon. The Raman effect, however, originates from inelastic scattering. In Raman scattering, the electron is exited from a different energy vibration level than the one it settles on, due to energy exchange between the excited electron and the incident photon. This can occur by two paths, obtaining Raman peaks called Stokes or Anti-Stokes lines, as illustrated in Figure 2.7**(a)** and **(c)**, respectively. If an electron is excited from an energy vibrational mode with energy v_0 to a higher energy state v_1, it takes the required energy for this transition from the incident photon. The molecule will thus scatter light with frequency $v_0 - v_1$, giving rise to a "Stokes" band Raman peak. However, if the electron is de-excited from energy vibrational mode v_1 to v_0, it transfers the excess energy to the photon, and the molecule will scatter light with frequency $v_0 + v_1$. In this case the obtained Raman peak is labeled an "Anti-Stokes" band. [31] and [30]

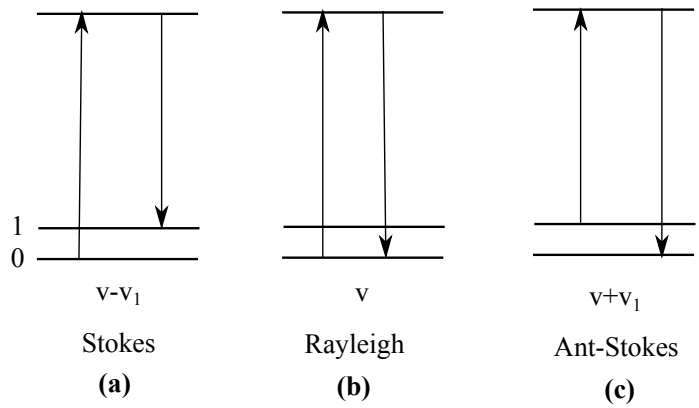

Figure 2.7: Scattering of monochromatic light by a sample can occur by two paths. By elastic Rayleigh scattering, without loosing energy, **(b)** or by inelastic Raman scattering via Stokes **a** or Anti-Stokes **(c)**. Figure made in Inkscape, adapted from [31].

Fluorescence of the sample poses a limitation to the Raman signal, due to the magnitude of the signal caused by fluorescent materials. The signal caused by fluorescence can be several orders of magnitude stronger than that obtained by the Raman scattering, resulting in a large background that may suppress the entire Raman spectrum, - especially if the Raman signal is weak. Fluorescence of molecules occurs mostly in the visible spectrum, between 300 and 700 nm. The undesirable effect can thus be annulled by shifting the excitation source out of the visible region, to the ultraviolet (UV) or near the infrared (near-IR) region. This technique is called UV Raman spectroscopy and Fourier Transform (FT) Raman spectroscopy, respectively. However, fluorescence usually increases at higher frequencies, which implies that some metal oxides can be studied with Raman spectroscopy at lower frequencies where fluorescence does not pose an issue [31].

There is limited research reported from Raman spectroscopy over $NiCo_2O_4$, however all spinels comprise the same Raman active vibrations. Introduction to group theory will not be covered by this thesis, but information on this subject can be reviewed in [32]. The Raman active modes in spinel structures relates to $3F_{2g}$, E_g and A_1, with the virbation frequency of A_1 usually being the highest. Most literature agrees that the A_1 vibration mode is assigned to the AO_4 unit in the spinel lattice [17]. For the spinel oxides investigated in the present work, that relates to the unit comprising nickel-ions.

2.4.5 Transmission Electron Microscopy

Figure 2.8 illustrates the different types of detectable signals that are generated from interaction between an electron beam and a sample. Transmission electron spectroscopy (TEM) is a commonly applied characterization technique that utilizes transmitted and diffracted electrons to produce a two dimensional projection of the analyzed sample. A high energy and intensity electron beam passes through the sample, it is diminished depending on the sample's density and thickness. The transmitted electrons are magnified by the apparatus optics, and produce a "bright-field" image (BF image). The electrons that experience diffraction from the sample, produce a two dimensional project that is off-angle to the transmitted beam. This image is called a "dark-field" image (DF). The quality of the obtained TEM image of a supported catalyst is dependent on the contrast between the supported particles and the support, which for several well dispersed supported oxides may be low [30].

STEM (Scanning TEM) combines the operation modes of scanning electron microscopy (SEM) and TEM. SEM maps the surface of a particle by detecting the secondary or backscattered electron's dependence on the position of the beam source. STEM allows the researcher to analyze certain regions of the sample separately, for example one supported particle on a larger particle. For catalysts with low contrast between supported particles and support, the contrast

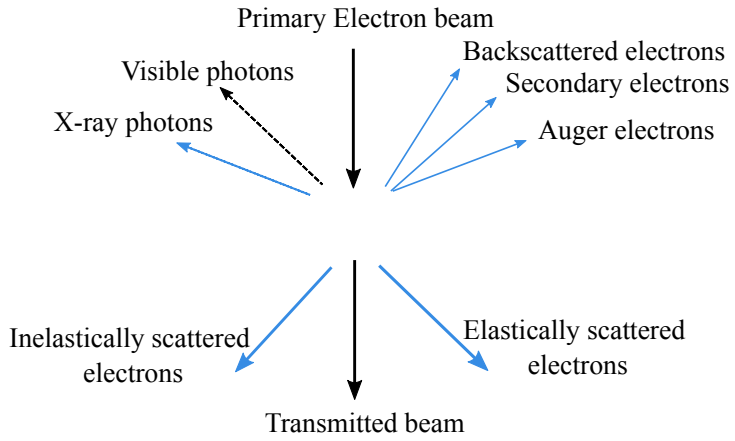

Figure 2.8: Different types of detectable signals generated from the interaction between an electron beam and a sample. Figure made in Inkscape, adapted from [33].

can be enhanced by ring-shaped detectors allowing for high angle annular dark field (HAADF) imaging [30].

Electron microscopy can also be utilized for elemental analysis, by exploiting the X-rays emitted from the sample. Energy dispersive x-ray spectroscopy (EDXS) detect and analyze the X-ray fluorescence from a sample and the local composition of a site can thus be determined [30]. Further can the diffraction pattern be investigated by analog XRD of the elastically scattered electrons, which provide for example lattice spacing and crystalline phases.

2.5 Gas Chromatography

The principle of gas chromatography (GC) is based on the separation and quantification of a gas mixture. The basic parts of the apparatus are the carrier gas, flow controller, injector, column, detector and data system, [34].

Mobile Phase

The mobile phase of a GC is the carrier gas, an inert gas that flows continuously through the injection port, column and detector. The sample gas is introduced through the injection port, and flows with the carrier gas to the column. The aim of the carrier is to carry the sample through the GC, without interacting chemically with the sample. It is required of the mobile phase to be of high purity. The most commonly used mobile phases are helium, nitrogen or argon, but hydrogen is also utilized, despite the high explosion risk. The choice of mobile phase is dependent on the detector used in the GC [34].

Stationary Phase

The stationary phase of the GC is dependent on the type of column utilized. Historically packed columns were utilized in GC, however the last decades they have been replaced with capillary columns. The advantage of capillary columns are that they are open, so little pressure drop occur through the column. This allows for utilization of long columns, up to 60 m (as opposed to maximum 2 m in packed columns), which enhance the efficiency of the GC.

The stationary phase of a capillary column is typically a liquid film or a solid substance coated to the column wall. A typical column is made of glass or stainless steel, and is coated with a high boiling liquid film on the inside, such as the wall coated open tubular column (WCOT). The support coated open tubular column is a packed column, and the stationary phase is comprised of the liquid film coated on the packing. However, certain columns does not comprise a liquid film, such as the porous layer open tubular column (PLOT column). In the PLOT column, the stationary phase is a porous layer of solid absorbent, coated on the on the column walls. Two examples if the porous layer are zeolite molecular sieves (such as MS 5A) or porous polymers (such as PLOT U). Depending on the sample compounds relative adsorption on the stationary phase and the respective vapour pressures, the sample gas is separated into its individual components. The components thus leave the column at different time points, and are further passed directly to a detector that quantifies the respective compounds and generates an electrical signal that is sent to the data system, [34].

Detector

The most common detectors are the flame ionization detector (FID), thermal conductivity detector (TCD) and the electron capture detector (ECD). FID is based on the ionization of each gas solute by burning the column effluent in a small oxy-hydrogen flame. The collected ions form a current that becomes the signal for the data system. The TCD (utilized in for this thesis) measures the thermal conductivity of the solute compounds in the carrier gas and compares it to the thermal conductivity in the pure carrier gas. It is thus beneficial to use a carrier gas that contains significantly different thermal conductivity properties than the samples. The most common mobile phases for TCDs are helium or hydrogen, both having much higher TC values than other inert gases. In this thesis helium is used as a carrier gas. The data system generates a chromatogram and automatically integrates the peak area for the separate compounds. This yields quantitative results about the concentration of the different compounds in the sample gas, and their specific retention time in the GC, [34].

2.6 Catalytic Activity

There are several methods to describe the activity of a catalyst. However, the activity can be difficult to quantify, and many methods are based on assumptions or empirical derivations. A practical way to gain information about the catalytic activity is to identify the temperatures necessary to obtain certain levels of conversion. T_{10}, T_{50} and T_{90} (respectively the light-off, half-conversion and 90% conversion temperatures) describes the temperatures at the point of 10%, 50% and 90% conversion of reactant.

Indications about the catalytic activity can also be drawn from its kinetic properties or from the activation energy.

2.6.1 Kinetics

The kinetic framework of a catalytic reaction describes the rate at which the reaction occurs. The kinetics are governed by the reaction mechanisms the reaction undergoes, and enables for relations between the reaction rate and measurable process parameters such as temperature, pressure and concentration. Catalytic reactions are a set of subsequent reaction mechanisms, and correct route of conversion can be difficult to determine. Several suggestions of kinetic models have been developed as the catalytic technology have advanced, for example the widely used Langmuir-Hinshelwood(LH) model and the Mars-Van-Krevlen (MvK) model. The latter presents a reaction path where reacting oxygen is stored and released in the material bulk; a process which may occur in metal oxides. LH-kinetics are based on the adsorption of one or all reactants as the preliminary step reaction. Studies of catalytic activity can be challenging. For instance, many of the reaction steps may be difficult or even impossible to measure. These undetectable transition states and intermediates still influence the overall kinetics. The measurable parameters of a reaction are thus usually used to obtain empirical data which are further compared with known kinetic models. This method may enable researches to conclude about certain kinetic parameters of the reaction from the basis of known kinetic models.

Chen et al (2015, [13]) report that common kinetic features for metal oxide catalysts around 500°C are positive reaction orders for both oxygen and methane, 0,16-0,32 and 0,7-0,9, respectively. They report of several proposed mechanisms for methane combustion over metal oxides, among others Langmuir-Hinshelwood and Mars-Van-Krevlen models. If the methane combustion is assumed to be first order in methane and zero order in oxygen, the reaction rate can be quantified according to Equation 2.7. This reaction is valid for low levels of methane

conversion, usually below 20%, and assuming differential conditions.

$$r = \frac{\text{GHSV}}{V_R} \cdot X \cdot C_{A0} \qquad \left[\frac{\text{mol}}{\text{h} \cdot \text{g}_{\text{cat}}}\right] \tag{2.7}$$

where r is the reaction rate, GHSV is the gas hourly space velocity, V_R is the reactor volume, X is the conversion of methane and C_{A0} is the feed concentration of methane. The GHSV is presented in Equation 2.8, where F_{tot} is the total feed flow and m_{cat} is the mass of catalyst used in the reaction.

$$\text{GHSV} = \frac{q_{\text{tot}}}{m_{\text{cat}}} \qquad \left[\frac{\text{NmL}}{\text{h} \cdot \text{g}_{\text{cat}}}\right] \tag{2.8}$$

The model can be checked for authenticity by regarding the relationship between the reaction rate and the feed concentration of reactant, which should be directly proportional, as can be seen in Equation 2.9 ($r \propto C_{A0}$). When applying reactions of unknown kinetics to known models, one should carefully consider the assumptions and limitations of the steps taken.

2.6.2 Activation Energy

The activation energy can be expressed as the energy threshold the system needs to overcome to facilitate reaction. Catalysts decrease the activation energy of a reaction, as illustrated in Figure 2.9, and hence decrease the amount of heat necessary for the reactants to react. As mentioned above, Chen et al. have provided a wide suggestion of reaction orders for several metal oxides in *Recent Advances in Catalysts for Methane Combustion* (2015, [13]). The materials explored in this thesis, however, have not be investigated widely for reaction order, though by assuming first reaction order, an estimation of the activation energy can be obtained. The obtained activation energy from the calculation will be empirical, and may include energy barriers not originating from the activation of methane. The calculated activation energy is thus denoted the *apparent* activation energy of catalytic combustion of methane over the studied materials.

If a reaction is assumed to be of the first order in component A, the rate of the reaction can be expressed as presented Equation 2.9, [35].

$$-r = k \cdot C_A \tag{2.9}$$

In the above equation, k is the rate constant, given by Equation 2.11 and the concentration of

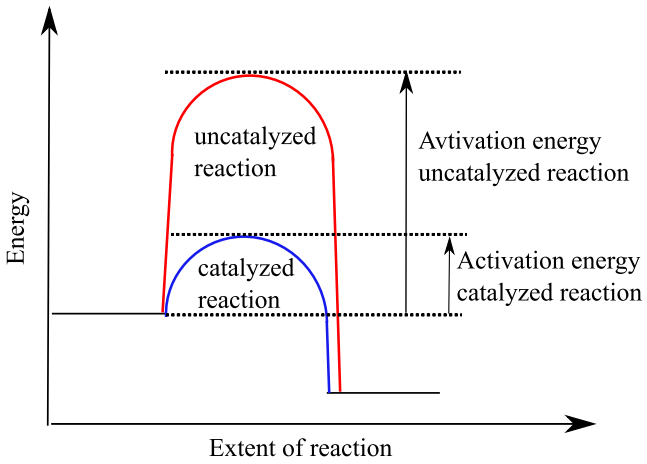

Figure 2.9: Illustration of an energy diagram of a reaction performed with or without a catalyst. The catalyst decreases the activation energy, E_A of the reaction. The figure is made in Inkscape.

CH_4, C_A, is given by Equation 2.10.

$$C_A = C_{A0}(1 - X_A) \qquad \left[\frac{\text{mol}}{\text{L}}\right] \tag{2.10}$$

$$k = A \cdot e^{-\frac{E_A}{R \cdot T}} \qquad [-] \tag{2.11}$$

In Equation 2.11, A is the pre-exponential factor, R is the gas constant, T is the temperature and E_A is the activation energy.

The design equation for a packed bed reactor is given by Equation 2.12.

$$\frac{df_A}{dW} = r_A \tag{2.12}$$

In this equation W is the weight of the catalyst bed and F is the molar flow rate of CH_4, which can be given by Equation 2.13, where q is the volumetric flow rate.

$$F = C \cdot q \qquad \left[\frac{\text{mol}}{\text{min}}\right] \tag{2.13}$$

q can further be expressed by the residence time, τ, and the reactor volume, V_R, as given in Equation 2.14.

$$q = \frac{V_R}{\tau} \qquad \left[\frac{\text{NmL}}{\text{min}}\right] \tag{2.14}$$

The reactor volume is given by the weight and the density of the catalyst, ρ, as described in Equation 2.15.

$$V_R = \frac{W}{\rho} \qquad \left[\mathrm{cm}^3\right] \tag{2.15}$$

By using Equations 2.9 and 2.13-2.15, Equation 2.12 can be expressed as Equation 2.16.

$$\frac{dC_A}{d\tau} = -k \cdot C_A \tag{2.16}$$

Inserting the relation in Equation 2.10 and solving the integral in Equation 2.16, obtains Equation 2.17.

$$-\ln(1 - X_A) = k\tau \tag{2.17}$$

By taking the natural logarithm on both sides of Equation 2.17, and inserting Equation 2.11, the expression above can be linearized.

$$\ln(-\ln(1 - X_A)) = \ln(A) - \frac{E_A}{R} \cdot \frac{1}{T} \tag{2.18}$$

In the above equation E_A is the activation energy and R is the gas constant. By plotting the left side of Equation 2.18 against $1/T$ one yields a straight line with slope $-E_A/R$. The activation energy can thus be found by multiplying the slope with the gas constant. To obtain a more accurate estimate of the activation energy, it is beneficial to use the points of low methane concentration as calculation basis, for example from 10-50% conversion.

The catalytic combustion of methane is a kinetically governed reaction, and has no thermodynamic limitations. This implies that the reaction can always reach full conversion regardless of the reactant composition and pressure of the system, provided that the sufficient energy needed to overcome the activation energy is applied the system. However, the reaction rate can be limited by mass transport from the gas bulk to the active sites within a catalyst pore. On highly active catalysts, the diffusion into the pore can be slower than the reaction rate, and the reaction thus becomes transport limited [21]. At higher temperatures, oxidation reactions can be quite fast, and transport limitations may play a role on the catalytic activity. In general, it is desired to utilize the catalyst as efficiently as possible, while maintaining high reaction rate. If the catalyst undergo pore diffusion or external mass transport limitations can be suggested by investigating the apparent activation energy in an Arrhenius plot. Figure 2.10 illustrates the dependency of the apparent activation energy on the transfer limitations.

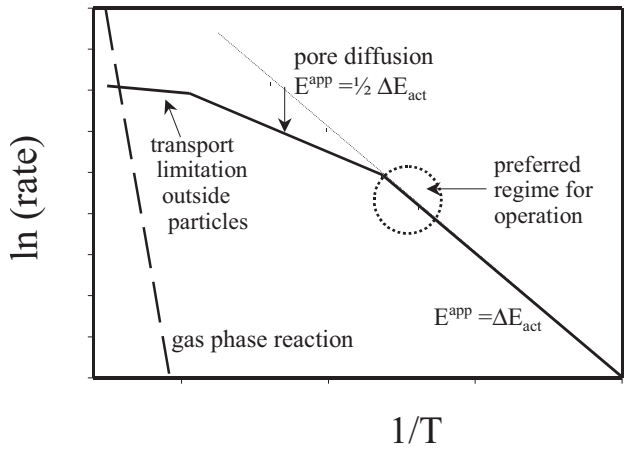

Figure 2.10: Arrhenius plot that illustrates the apparent activation energy under the influence of external transport limitations and pore diffusion limitations. The figure is obtained from [21] (p. 215).

Chapter 3

Experimental

3.1 Risk Assessment

The safety measurements and risks associated with the experiment were assessed following the NTNU Risk Assessment protocol. In addition, the after-hours agreement of the university was followed.

The highest risk was assumed to be associated with the usage of combustible gas in the catalyst activity experiments, due to the severity of potential consequences. This risk was however deemed acceptable, as the experiments were conducted within a closed rig, equipped with gas sensors and ventilation. The reaction rig was further equipped with a pressure controller, that would release all gas flow through the rig to ventilation if a critical pressure was exceeded. To further ensure that no combustible gas was released to the closed rig, a gas leakage test was conducted prior to every reaction run.

Several corrosive and/or toxic substances were used in the preparation of the catalysts, such as the precursor compounds $Ni(NO_3)_2{\cdot}6H_2O$ and $Pd(NO_3)_2$. The appropriate protective equipment were used when handling such substances, and the disposal regulations of the university was followed with care.

The risk assessment can be reviewed fully in the university risk assessment portal, with ID-number 12342.

3.2 Catalyst Synthesis

A total of six catalysts, presented in Table 3.1, were synthesized during the research, with the aim to investigate the effect of oxide composition, calcination temperature and noble metal deposition on catalytic activity. Batches 1-3 were synthesized to investigate methane oxidation dependency of spinel composition. Of these three, the first was a stoichiometric spinel, $NiCo_2O_4$, which will be presented as a reference catalyst in this report. The second catalyst, $NiCoO_4$, comprised a stoichiometric surplus of nickel with a 1:1 ratio of nickel and cobalt. The

third, $Ni_{0,75}Co_{2.25}O_4$, comprised a stoichiometric deficit of nickel. Batch 4 and 5 in Table 3.1 were both stoichiometric spinels, $NiCo_2O_4$. They were synthesized together in a large batch and investigated for dependency of calcination temperature, which was conducted at 350°C and 550°C, for Batch 4 and 5, respectively. Investigations of the reference catalyst and Batch 4 also allowed for evaluation of the reproducibility of the catalyst synthesis. Further, the effect of deposition of a small fraction of palladium (Pd) upon the stoichiometric spinel was investigated. A catalyst with 0,5wt%Pd supported on $NiCo_2O_4$ was thus synthesized; denoted Batch 6 in Table 3.1. It should be noted that all catalysts except for the one denoted $NiCo_2O_{4-550°C}$ was calcined at 350°C.

All mixed oxides, including the support for 0,5wt%Pd/$NiCo_2O_4$ were synthesized by the coprecipitation method. The palladium was further deposited on $NiCo_2O_4$ by incipient wetness impregnation.

3.2.1 Coprecipitation

The coprecipitation method is presented in Section 2.3. The precursor compounds for cobalt and nickel were $Ni(NO_3)_2{\cdot}6H_2O$ and $Co(NO_3)_2{\cdot}6H_2O$, respectively. The appropriate amounts of precursors, given in Table 3.1, were weighed, mixed and dissolved with sufficient amount of deionized water. The precipitating agent was potassium hydroxide (KOH) with molarity of 1 M. The amounts of deionized water and KOH that were used to produce the different batches of catalysts are presented in Table A.2 in Appendix A. Potassium hydroxide was dripped into the precursor solution, which was kept homogeneous by continuous stirring and bubbling of N_2. The resulting precipitate was centrifuged and washed with deionized water at 60°C, until the centrifugate held the pH value of around 7. The pH was measured using litmus paper. The precipitate was further dried at 130°C for 24 hours, then cooled, crushed and calcined in a quartz calcination apparatus under air for 24 hour. The calcination temperatures for the different catalysts are specified in Table 3.1.

For the catalyst activity experiments the calcined catalyst particles were sieved, to obtain particles with size fraction 200-400μm. If the obtained amount of desired fraction was too small, the fraction smaller than 200μm was pelletized and recrushed to obtain the sufficient amount of 500 mg catalytic material from each batch.

The calculations done to obtain correct amount of precursor compounds and molarity of KOH are presented in Appendix A.

Table 3.1: Measured amount of precursor compounds for the catalysts, found according to calculations presented in Appendix A, and the respective calcination temperatures. The different batches of catalysts have been provided with numbers 1-6, to more easily distinguish between them.

Batch	**Catalyst**	**Mass** [g] $Ni(NO_3)_2 \cdot 6H_2O$	**Mass** [g] $Co(NO_3)_2 \cdot 6H_2O$	$\mathbf{T_{Calcination}}$ [°C]
1^a	$NiCo_2O_4$	2,9021	5,8233	350
2^a	$NiCoO_4$	5,88236	5.8163	350
3	$Ni_{0,75}Co_{2,25}O_4$	2,1809	6,5482	350
4^b	$NiCo_2O_{4-350°C}$	5,8043	11,6417	350
5^b	$NiCo_2O_{4-550°C}$			550
6^c	0,5wt%Pd/$NiCo_2O_4$	5,8088	11,6475	350

[a] synthesized during Specialization Project, A16.
[b] precipitated together in a large batch, and calcined at different temperatures after drying.
[c] $NiCo_2O_4$ synthesized as support for 0,5wt%Pd/$NiCo_2O_4$.

3.2.2 Incipient Wetness Impregnation

The incipient wetness impregnation method, described in Section A.2, was used to make a catalyst with 0,5wt% palladium loading, 0,5wt%Pd/$NiCo_2O_4$, batch 6 in Table 3.1.

The support used was a stoichiometric spinel, $NiCo_2O_4$, which was made with the co-precipitation method explained above. The amounts of precursors used to make the support are presented in Table 3.1. The finished support was sieved to obtain maximal amount of the particle fraction between 200-400μm, and the weight of obtained support was noted.

Before impregnation the necessary amount of water and Pd-precursor to obtain a 0,5wt% loading to the support was identified. Based on the mass of support, the amount of Pd-precursor, $Pd(NO_3)_2$, was calculated according to Equations A.4-A.6 in Appendix A.2. The material was further saturated by dripping de-ionized water to the surface, using a pipette. The necessary volume of water to saturate the material was noted. Before impregnation, the wet support was dried overnight.

26,8 mg of $Pd(NO_3)_2$ was dissolved in 1,25 mL deionized water, and the solution was added to the support. The mixture was further dried for 3 h at 110°C and calcined at 350°C for additional 3 h. The drying and calcination procedure was determined according to the experimental method outlined by Chen et al. in [36]. Chen et al. studied palladium deposited on cobalt oxide spinel, Co_3O_4, which was assumed to exhibit similar characters to palladium deposited on $NiCo_2O_4$.

3.3 Catalyst Characterization

Batch 1 of $NiCo_2O_4$ was chosen as a reference catalyst for the experimental work. Most characterization techniques were thus conducted twice over this catalyst, to provide a measure of method reproducibility.

3.3.1 X-ray Diffraction

The principle of X-ray diffraction is presented in Section 2.4.1.

To obtain information about the crystalline phases in the samples, the catalysts were investigated in a Bruker D8 Advance DaVinchi X-ray Diffractometer. The apparatus utilizes CuKα radiation with wavelength $\lambda = 1,54$ nm. The analyses were conducted with fixed slit at 0,2 mm, to avoid accumulation of background due to the nature of the samples. The range of analyses were at angles 2θ from 10-75°, with scan time set to 30 minutes. $NiCo_2O_4$ was analyzed twice, to assure method precision. The obtained diffractograms were further analyzed with the DIFFRAC EVA and TOPAS softwares.

3.3.2 N_2 Physisorption

The theory of N_2 physisorption is presented in Section 2.4.2.

The surface area and pore volume of the catalysts were analyzed with the method of N_2 physisorption using a Micromeritics TriStar II 3020 Surface Area and Porosity Analyzer. The apparatus was equipped with a VacPrep 061 Degasser for sample preparation.

The catalysts were analyzed at liquid nitrogen temperature (77 K) after calcination treatment. Sample 1, $NiCo_2O_4$, was analyzed twice. 50-100mg of catalyst was placed in a sample tube, weighed, and degassed using the VacPrep 061 Degasser unit. The sample was evacuated for one hour at ambient temperature, before it was placed in the heating station and degassed overnight at 200°C. The sample was ready for analysis when it reached a pressure equal to or less than 100 mTorr. The sample tube was then installed to the Micromeritics Tristar apparatus, and liquid nitrogen was filled to the apparatus dewar. The sample was reweighed after measurement, to acquire information about material loss during measurement. The amounts of catalyst samples for all catalysts before and after measurement are presented in Table 3.2.

Table 3.2: Amount of sample for BET analysis, before and after N_2 physisorption. The reference catalyst, Batch 1 of $NiCo_2O_4$, was analyzed twice.

Sample	**Catalyst**	**Initial weight** [mg]	**Final weight** [mg]
1^a	$NiCo_2O_4$	64,8	64,4
$1^{a,b}$	$NiCo_2O_4$	71,7	71,2
2^a	$NiCoO_4$	72,9	71,2
3	$Ni_{0,75}Co_{2,25}O_4$	66,9	64,8
4	$NiCo_2O_{4-350°C}$	65,9	62,3
5	$NiCo_2O_{4-550°C}$	59,3	71,2
6^c	$NiCo_2O_4$	61,9	61,4
6	0,5wt%Pd/$NiCo_2O_4$	75,7	74,8

[a] synthesized and analyzed during Specialization Project, A16.
[b] second analysis.
[c] support for 0,5wt%Pd/$NiCo_2O_4$.

3.3.3 X-ray Fluorescence

The principle of X-ray fluorescence is presented in Section 2.4.3.

X-ray fluorescence was conducted with a Wavelength Dispersive X-Ray Fluorescence Supermini200 analyzer. The instrument was equipped with an X-ray tube, which generated X-rays from a Pd-source.

To avoid large sources of error, the sample preparation was executed with care. To obtain reliable results the samples should be presented as homogeneous as possible, and with minimal contamination. The samples were thus prepared as pellets of 40 mm diameter, with boric acid (H_3BO_3) as a binder. 100-200 mg of sample and 2,5-3 g boric acid was mixed and crushed to a homogeneous powder. This powder was pelletized to a 40 mm diameter pellet which was introduced to the sample holder. The sample holder was covered with a 6μm polypropylene film, which was ensured to cover the pellet surface smoothly without wrinkles.

Table 3.3 presents the sample amounts of different catalysts and boric acid for catalyst batches 1-6. The reference catalyst, Batch 1 of $NiCo_2O_4$, was prepared and analyzed twice, to obtain a measure of procedure reproducibility and error.

Table 3.3: Amount of sample and sample binder, H_3BO_3, for X-ray fluorescence analyses of catalysts batches 1-6. Batch 1, the reference catalyst $NiCo_2O_4$, was analyzed twice.

Sample	**Catalyst**	**Amount sample** [mg]	**Amount H_3BO_3**[g]
1[a]	$NiCo_2O_4$	190,6	3,08
1[a,b]	$NiCo_2O_4$	162,5	2,88
2[a]	$NiCoO_4$	175,4	2,99
3	$Ni_{0,75}Co_{2.25}O_4$	164,6	2,84
4	$NiCo_2O_{4-350°C}$	176,7	2,92
5	$NiCo_2O_{4-550°C}$	184,7	2,94
6	0,5wt%Pd/$NiCo_2O_4$	190,6	2,93

[a] synthesized during Specialization Project, A16.
[b] second analysis.

3.3.4 Raman Spectroscopy

Raman spectroscopy analyses were performed over catalyst batches 1-3, $NiCo_2O_4$, $NiCoO_4$ and $Ni_{0,75}Co_{2.25}O_4$, in order to obtain further information about how the Ni/Co-ratio influenced the structural properties of the materials. The apparatus was a HORIBA JOBIN YVON-LabRAM spectrometer, and the samples were investigated with a HeNe continuous wave laser with wavelength 632,8 nm and effect 20mW. The LabSpec software was used to locate and identify the Raman peaks.

3.3.5 Transmission Electron Microscopy

Transmission Electron Microscopy (TEM) and STEM (scanning TEM) was performed utilizing a Jeol JEM ARM200F apparatus. The aim of the analysis was to locate and gain information about the deposition of palladium on 0,5wt%Pd/$NiCo_2O_4$, in addition to get an overview of the particle system of the support. The TEM images were acquired by Research Scientist Ruben Bjørge, at SINTEF Materials and Chemistry. The apparatus was equipped with a large angle EDX, which allowed for elemental characterization in the points suspected of comprising a Pd-particle.

3.4 Catalyst Testing

The aim of the catalyst testing was to investigate and compare the catalytic performances of the different batches of catalysts, and the potential production of undesired byproducts. Further,

the catalytic performance and potential deactivation in relation to the reactant feed composition was investigated. The first batch of catalyst, $NiCO_2O_4$, was chosen as a reference catalyst, which were used as point of comparison for the remaining catalysts, and the changes in conditions. Further, the catalyst was used to gain information about procedure reproducibility.

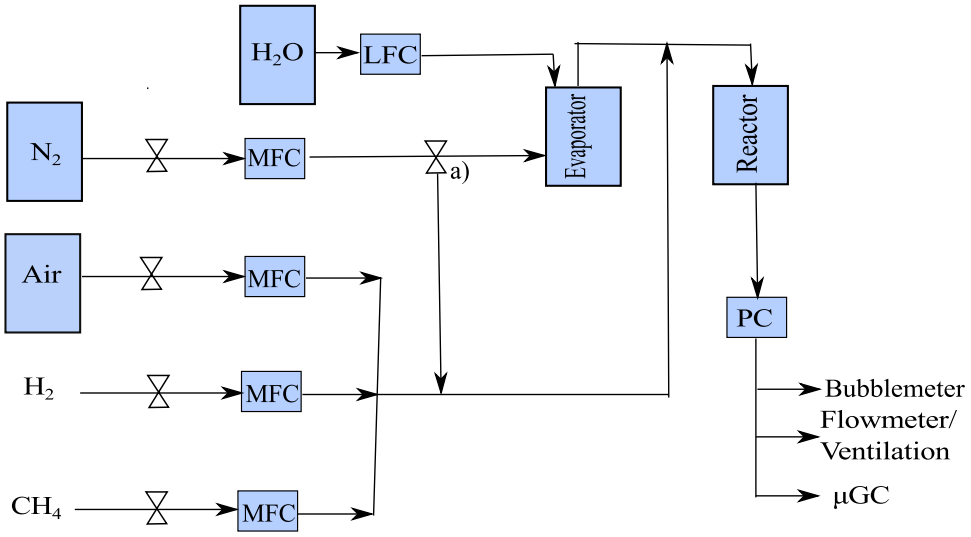

Figure 3.1: A simplified illustration of the reaction rig adapted for the methane oxidation experiment. MFC is short for Mass flow controller, LFC for liquid flow controller, μGC for Micro Gas Chromatograph and PC for Pressure Controller. The valve marked by a) was turned to the evaporator for the experiment including 15mol% H_2O in the reactant feed. The figure is made in Inkscape.

The catalytic activities were tested in an adapted reaction rig for methane oxidation. The reaction rig is illustrated in Figure 3.1, and was equipped with several mass flow controllers (MFCs), which monitored the feed rate of the reactant gases, and a pressure controller (PC) designed to cut the gas flow if the pressure in the system increased beyond the rig's tolerance. The product feed was connected to a µGC-apparatus, for product analysis. The catalysts were investigated in a quartz reactor, illustrated in Figure 3.2. The reactor was equipped with a temperature pocket which allowed for temperature measurements along the catalyst bed, where a thermocouple was inserted. The illustration of the experimental rig in Figure 3.1 indicates the position of the reactor.

As the experimental outline was to compare the catalytic performances and the relation to reactant composition, certain parameters were kept constant throughout the experiment. These parameters are presented in Table 3.4. The reactant gas compositions were chosen based on the features of realistic NG vehicle exhaust, presented in Section 2.1, as the activity under such conditions remained the overall aim of the present work. The main features of all reactant compositions were thus low methane concentration and high oxygen concentration. The

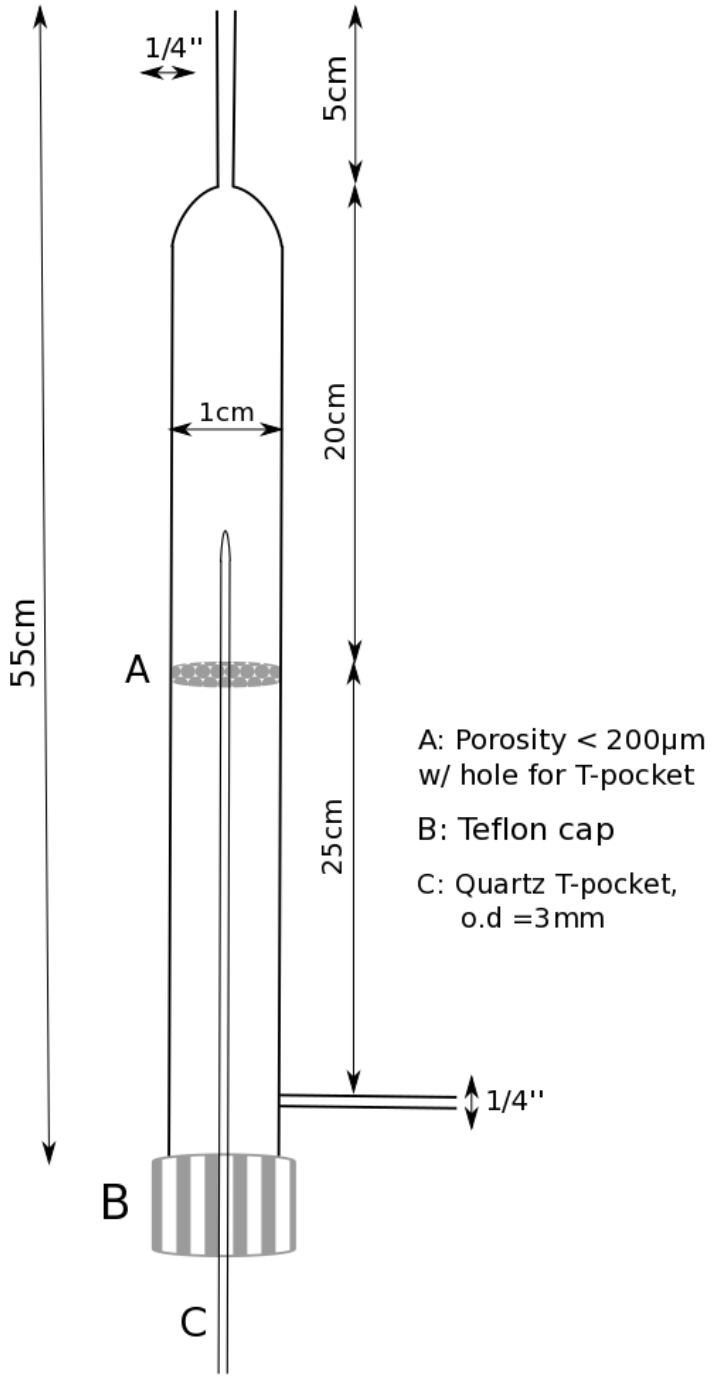

Figure 3.2: A simplified illustration of the quartz reactor utilized for catalytic methane oxidation. The figure is made in Inkscape.

combustion was ranging from lean to highly lean, based on the concentration of methane. As NG vehicle exhaust gas generally contains high concentration of O_2, the concentration of O_2 was kept constant at 10% in all feed compositions. The stoichiometric dependency of CH_4 and O_2 was thus not analyzed for the different CH_4 concentrations. Four different reactant gas compositions were analyzed for methane oxidation over the catalysts, denoted reactant feed 2%, 0,5%, 0,1% and 0,1%$_{H2O}$, indicating the methane concentration in the reactant feed and, for the latter, the presence of water. The investigation of the effect of water on catalytic activity was prioritized over the effect of CO_2 present in the feed, due to the review performed by Géline et al (2002, [1]) that report that for noble metal catalysts CO_2 presence has limited influence on catalytic activity. All feed mixtures contained 10% O_2 and balance N_2. Table 3.4 presents the conditions held constant for all reactions, and Table 3.5 presents the composition of the feed gas and the respective flow rates for each run. The calculation of the air-to-fuel equivalence ratio λ presented in Table 3.5 were calculated according to Equation 2.2 and can be reviewed in Appendix F.1.

Table 3.4: Parameters held constant for all performed reactions.

Parameter	**Symbol**	**Value**	**Unit**
Volumetric flow	F_{tot}	200	$NmL\,min^{-1}$
Flow O_2	F_{O_2}	20[a]	$NmL\,min^{-1}$
Gas Hourly Space Velocity	GHSV	24000	$NmL/h\,g_{cat}$
Residence time	τ	0,8	s^{-1}
Height catalyst bed	h	17	mm

[a] flow synthetic air: 95,25 $NmL\,min^{-1}$.

The mass flow controllers (MFCs), monitoring the feed rate of the different reactant gases to the reactor, were calibrated prior to the catalyst testing. The method of calibration, and the resulting calibration curves can be review in Appendix B. The calculation of set points for the specific flow rates can also be reviewed in Appendix B, and all set points are listed in Table B.1.

The catalyst bed was comprised of approximately 500 mg of sample with size fraction between 200-400μm, which was mixed with an inert material at a ratio of 1:3 catalyst and inert. The chosen inert material was silicon carbide (SiC) with mesh 60, due to the material's excellent temperature endurance. The dilution of catalyst was carried out to avoid hot spots and to dissipate the heat generated by the reaction. After implementation of the catalyst bed, the height of the bed was measured. The size fraction of catalytic material and inert was chosen to minimize the pressure drop over the catalyst bed. The fraction between 200-400μm had been identified as the optimal particle size by Associate Professor Jia Yang in previous experiments. The catalyst and respective amount used in Runs 1-17 are presented in Table 3.6.

After installation of the reactor, a gas leakage test was conducted over the rig. This was done

Table 3.5: Feed gas composition, flow rate and air-fuel equivalence ratio λ for four different reactant feed mixtures, and the respective runs they were applied to. All reactant feeds were complimented with 10% O_2 and balance N_2. Total flow rate was 200 NmLmin^{-1}. The respective calibrated mass flow controller set points can be reviewed in Appendix B. The catalysts used in Run 1-17 is presented in Table 3.6. λ is calculated in Appendix F.1.

Reactant feed	**CH_4**		**H_2O**		λ	**Run**
	mol%	NmL/min[a]	mol%	NmL/min		
2%	2	4	-	-	2,5	1, 6, 8, 10, 12, 14
0,5%	0,5	1	-	-	10	2, 7, 9, 11, 13
0,1%	0,1	0,2	-	-	50	3, 5, 15, 17
$0,1\%_{H_2O}$	0,1	0,2	15	30	50	4, 16

[a] for flow 0,2 NmLmin^{-1}: 5%CH_4 in N_2.

Table 3.6: Catalyst bed height and the amount of catalyst, m_{cat}, and inert, m_{SiC} used in Runs 1-17. The reactant feed compositions in Runs 1-17 are presented in Table 3.5.

Batch	**Catalyst**	**m_{cat}** [mg]	**m_{SiC}** [g]	**Bed height** [mm]	**Run**
1[a]	$NiCo_2O_4$	501,7	1,5101	17	1-5
2[a]	$NiCoO_4$	500,7	1,5008	17	6-7
3	$Ni_{0,75}Co_{2.25}O_4$	500,3	1,5016	17	8-9
4	$NiCo_2O_{4-350°C}$	500	1,5015	17	10-11
5	$NiCo_2O_{4-550°C}$	499	1,4965	17	12-13
6	0,5wt%Pd/$NiCo_2O_4$	500,7	1,5091	17	14-17

[a] synthesized during Specialization Project, A16.

by feeding 2% H_2 in N_2 through the reactor, and monitoring the links between reactor and gas feed and product pipes using a gas detector with cross sensitivity for H_2 and CO. If no H_2 was detected, the gas in the reactor was flushed out with pure N_2 for a couple of minutes, before the reactant feeds presented in Table 3.5 were introduced.

The catalytic activities were investigated by multiple aspects. The dependency of Ni/Co-ratio on catalytic activity were studied in Run 1, 2 and 6-9, by facilitating reaction with two different reactant feeds over the stoichiometric different catalysts, $NiCo_2O_4$, $NiCoO_2$ and $Ni_{0,75}Co_{2,25}O_4$. Methane concentration dependency was investigated in Runs 1-3, and the effect of Pd-deposition was investigated by comparing the activities in Runs 1 and 2 with 14 and 15. The effect of H_2O in the reactant feed was studied over the reference catalyst $NiCo_2O_4$ and over 0,5wt%Pd/$NiCo_2O_4$ in Runs 4 and 16, and the potential deactivation of the catalysts was checked for reversibility in Runs 5 and 17.

The catalyst activities were tested at increasing and decreasing reactor temperatures, from

room temperature and until complete conversion of methane was obtained. The temperature increased and decreased at a ramp of 5 K/min, and from 200-550°C it increased in a stepwise manner with 25°C increments holding constant temperature for 30 minutes. For reactant feed $0{,}1\%_{H_2O}$, water was introduced into the feed when the balance feed reached 200°C. At this point the N_2 stream was introduced into the water vapor feed, by turning the valve marked in Figure 3.1. Multiple cycles were completed for each run, to evaluate reproducibility between reaction cycles and potential change of catalytic activity after time on stream.

Based on results obtained from characterization and activity investigation through the experimental time line, the maximum reactor temperature was set to 500°C for Runs 14-17. The reactor temperature was thus kept at constant temperature for every 25°C between 200-500°C for these experiments. The motivation for this was to shield the catalyst for potential structural changes as much as possible, an observation that will be discussed in Chapter 5. Further, it was observed that addition of H_2O to the feed decreased the catalytic activity considerably, and a reaction with 0,1% CH_4 without water was thus repeated, to investigate if the deactivation of the catalyst was reversible.

3.4.1 Calculation of Methane Conversion

The reaction rig was coupled with an Agilent 3000 Micro Gas Chromatograph (μGC) apparatus, with two PLOT columns and helium as mobile phase. The two columns detected different gases from the reactant feed, Channel A (MS 5A PLOT (10 m x 0.32 mm) column) for detecting nitrogen and methane, and Channel B (PLOT U (8 m x 0.32 mm) column) for detecting CO_2 and other carbonaceous species. A TCD detector was used for this analysis. The μGC was calibrated prior to the experiment, to obtain accuracy for diluted levels of methane. Two calibration gases of different composition were utilized, one with 1% and one with 5% CH_4 content. Two methods were calibrated, to be applied for different levels of CH_4.

During the reaction cycle a fraction of the product gas was continuously fed to the μGC, which simultaneously analyzed and quantified the product composition. This allowed for calculation of methane conversion, X_{CH_4}, which is defined by the amount of reacted methane, given in Equation 3.1.

$$X_{CH_4} = \frac{F_{CH_4,in} - F_{CH_4,out}}{F_{CH_4,in}} \tag{3.1}$$

The flow of methane can be expressed by the concentration of methane in gas phase and the total flow of gas, presented in Equation 3.2 where p denotes the point along the reactor, i.e inlet

or outlet. This equation is applicable to any species present in the gas mixture.

$$F_{\mathrm{CH_4},p} = y_p \cdot F_{tot,p} \tag{3.2}$$

The gas composition of a species, y_i, provided by the μGC, is given by the peak area, measured by the electrical signal generated from the species, multiplied by it's response factor, k_i:

$$y_i = A_i \cdot k_i \tag{3.3}$$

By inserting the relationship in Equation 3.2 to Equation 3.1, the conversion of methane can be expressed as Equation 3.4.

$$X_{\mathrm{CH_4}} = \frac{y_{\mathrm{CH_4},in} \cdot F_{tot,in} - y_{\mathrm{CH_4},out} \cdot F_{tot,out}}{y_{\mathrm{CH_4},in} \cdot F_{tot,in}} \tag{3.4}$$

For the case when all methane is being converted only to CO_2 and H_2O, and no undesirable byproducts are formed, the system is stoichiometrically balanced, and $F_{tot,in} = F_{tot,out}$. This case is true for the overall mass balance, but is not valid over the μGC as H_2O is condensed from the product flow before it enters the columns. The concentration of N_2 can thus be used to express F_{tot}, as nitrogen is inert, and does not undergo reaction. By solving the previous derived relationships with respect to N_2, Equations 3.5-3.7 can be used to express Equation 3.4 with measurable quantities.

$$F_{tot,in} = \frac{F_{N_2,in}}{y_{N_2,in}} \tag{3.5}$$

$$F_{tot,out} = \frac{F_{N_2,out}}{y_{N_2,out}} \tag{3.6}$$

$$F_{N_2,in} = F_{N_2,out} \tag{3.7}$$

The conversion of CH_4 can thus be expressed by Equation 3.8.

$$X_{\mathrm{CH_4}} = 1 - \frac{y_{\mathrm{CH_4},out}}{y_{\mathrm{CH_4},in}} \cdot \frac{y_{\mathrm{N_2},in}}{y_{\mathrm{N_2},out}} \tag{3.8}$$

If CH_4 and CO_2 are the only carbon species in the system, the conversion of methane could also be calculated with basis on the produced CO_2. However, for the present work the μGC was

calibrated for low amounts of methane. By using CO_2 as calculation basis, the uncertainty of the calculation could increase, as the μGC was not calibrated for low amounts of CO_2.

3.4.2 Carbon Balance

The validity of the calculated conversion can be indicated by performing a mass balance over carbon in the system. If all carbon from methane is exclusively converted to CO_2, Equation 3.9 would be valid.

$$F_{\mathrm{CH_4},in} = F_{\mathrm{CH_4},out} + F_{\mathrm{CO_2},out} \tag{3.9}$$

The error in the carbon balance, E_C, can thus be calculated according to Equation 3.10.

$$E_C = 100\% \cdot \left(1 - \frac{F_{\mathrm{CH_4},in}}{F_{\mathrm{CH_4},out} + F_{\mathrm{CO_2},out}}\right) \tag{3.10}$$

The error in carbon balance can further be expressed by Equation 3.11, if the previous derived relationships are inserted to Equation 3.10.

$$E_C = \left(1 - \frac{y_{\mathrm{CH_4},in}}{y_{\mathrm{N_2},in}} \cdot \frac{y_{\mathrm{N_2},out}}{y_{\mathrm{CH_4},out} + y_{\mathrm{CO_2},out}}\right) \tag{3.11}$$

Chapter 4

Results

4.1 Catalyst Characterization

4.1.1 X-ray Diffraction

The X-ray diffractograms for the three catalysts with different Ni/Co-ratios are presented in Figure 4.1, where $NiCo_2O_4$ is indicated by red, $NiCoO_4$ by green and $Ni_{0,75}Co_{2,25}O_4$ by blue. The reference catalyst $NiCo_2O_4$ was analyzed twice, though only one spectrum was investigated further, as the two obtained spectra exhibited equal features. The two XRD analyses of the reference catalyst can be reviwed in Figure C.1 in Appendix C. In Figure 4.1 the square, circle and star respectively indicate the crystalline phase of $NiCo_2O_4$, Co_3O_4 and NiO. These phases were the suggested phases found by utilizing the DIFFRAC EVA software database.

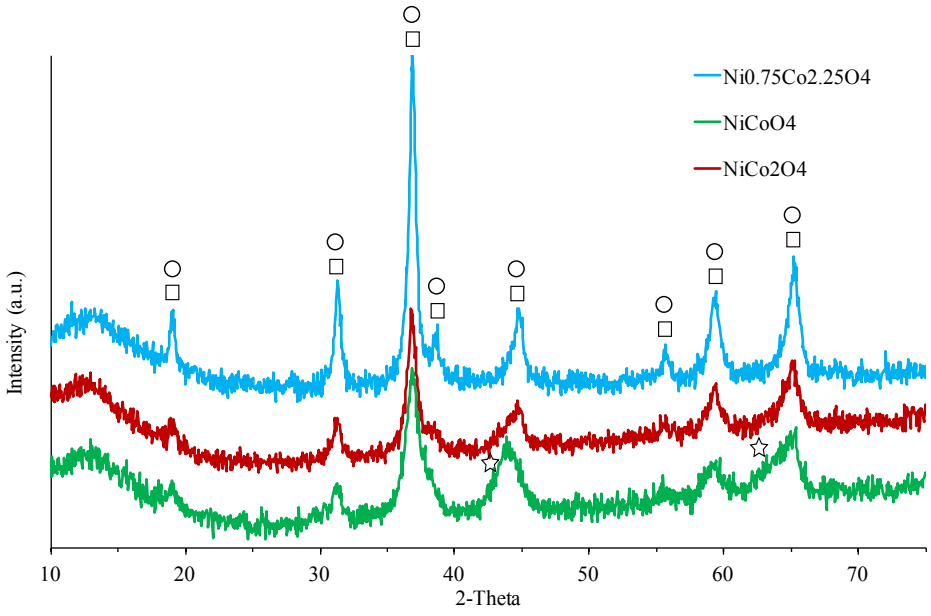

Figure 4.1: The XRD spectra for three catalysts with different Ni/Co-ratio, $NiCo_2O_4$ (red), $NiCo_2O_4$ (green) and $Ni_{0,75}Co_{2,25}O_4$ (blue). The suggested phases are; □: $NiCo_2O_4$, ○ : Co_3O_4 and ★: NiO, which were found using DIFFRAC EVA software.

As can be seen in Figure 4.1 the materials generally exhibit similar characteristic features, despite slight variations in peak shapes and intensities. These variations will be discussed further in Section 5.1.

Figure 4.2 presents the XRD spectra of the 4th and 5th batch of catalyst, which was stoichiometric spinel $NiCo_2O_4$ calcined at different temperatures. The figure also presents the spectrum obtained for 0,5wt%Pd/$NiCo_2O_4$. In this figure orange indicates $NiCo_2O_{4550°C}$, gray indicates $NiCo_2O_{4350°C}$ and blue indicates 0,5wt%Pd/$NiCo_2O_4$. It was noted that the $NiCo_2O_{4550°C}$ spectrum displayd more intense and sharp pekas for the $NiCo_2O_4$-phase. Further, additional peaks were observed for $NiCo_2O_{4550}$ at 2θ = 43 and 63, which were identified as NiO by the DIFFRAC EVA software database. No peaks indicating potential phases of Pd were detected in the XRD analysis.

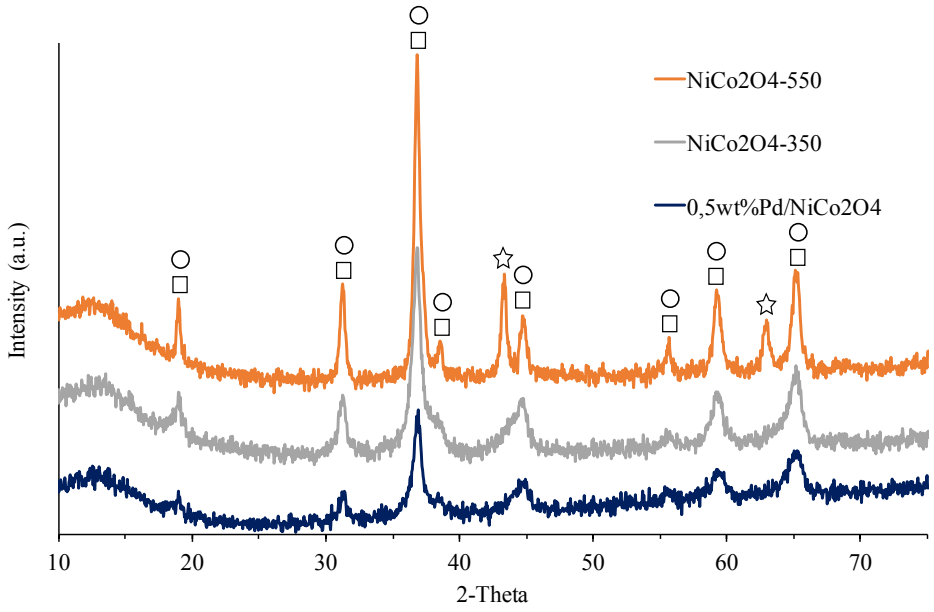

Figure 4.2: The XRD spectra for $NiCo_2O_{4350}$ (gray), $NiCo_2O_{4550}$ (orange) and 0,5wt%Pd/$NiCo_2O_4$ (blue).The suggested phases are; □: $NiCo_2O_4$, ◯ : Co_3O_4 and ★: NiO, which were found using DIFFRAC EVA software.

All spectra of the stoichiometric spinel calcined at 350°C, were graphed together and can be reviewed in Figure C.2 in Appendix C. The three spectra exhibited similar features with slight deviations that were deemed acceptable for procedure accuracy.

The Bruker TOPAS software was employed to estimate the crystallite sizes for all materials, according to the Scherrer-equation given by Equation 2.5. The crystallite sizes for all phases detected in the different materials are presented in Table 4.1.

4.1.2 N_2 Physisorption

Table 4.1 contains the obtained results from the N_2 physisorptions and the XRD analyses. S_{BET} is the specific surface area obtained with the BET-method and the pore volume was obtained with the BJH method (for theory see Section 2.4.2).

Table 4.1: Specific surface area, S_{BET}, pore volume and crystallite size in diameter, d_{cryst}, for the catalytic materials. S_{BET} and the pore volume were obtained after material analysis by N_2 physisorption, by the BET-equation and the BJH-method, respectively. d_{cryst} was found from X-ray diffraction, upon employment of the Scherrer-equation, and is denoted the crystallite size of the phase it represents. $NiCo_2O_4$ was analyzed twice for N_2 physisorption.

Batch	**Catalyst**	$\mathbf{S_{BET}}$ $[m^2 g_{cat}^{-1}]$	$\mathbf{V_P}$ $[cm^3 g_{cat}^{-1}]$	$\mathbf{d_{NiCo_2O_4}}$ [nm]	$\mathbf{d_{NiO}}$ [nm]
1[a]	$NiCo_2O_4$	53,50	0,19	6,01	-
1[a,b]	$NiCo_2O_4$	55,60	0,19	-	-
2[a]	$NiCoO_4$	64,80	0,18	4,91	2,86
3	$Ni_{0,75}Co_{2,25}O_4$	36,50	0,17	9,10	-
4	$NiCo_2O_{4-350°C}$	47,11	0,19	6,82	-
5	$NiCo_2O_{4-550°C}$	28,11	0,15	14,34	14,24
6[c]	$NiCo_2O_4$	56,71	0,15	6,29	-
6	0,5wt%Pd/$NiCo_2O_4$	51,98	0,16	5,79	-

[a] synthesized and analyzed for Specialization Project, A16.
[b] second analysis.
[c] support for 0,5wt%Pd/$NiCo_2O_4$.

4.1.3 X-ray Fluorescence

The results from the X-ray fluorescence analyses are presented in Table 4.2. It was found that small amounts of potassium were present in all catalysts, in addition to cobalt and nickel. The measured amount of palladium on 0,5 wt%Pd/$NiCo_2O_4$ deviated from the nominal loading by +58%. The theoretical mass percentage of each catalyst are calculated and presented in Table C.1 in Appendix C.

Table 4.2: Results from X-ray fluorescence analyses of all catalysts. The concentration of the identifies components are presented as mass percentage. d indicates the deviation by percentage from theoretical stoichiometric mass percentage, and is calculated according to Equation C.3. The theoretical stoichiometric mass percentages are presented in Table C.1 in Appendix C.

Batch	**Catalyst**	**Co^{3+}** [Mass%]	**±d** %	**Ni^{2+}** [Mass%]	**±d** [%]	**Pd^{2+}** [Mass%+d]	**K_2O** [Mass%]
1[a]	$NiCo_2O_4$	65,2	-2,3	33,8	+1,7	-	1,01
1[a,b]	$NiCo_2O_4$	66,4	-0,5	32,6	-1,9	-	0,99
2[a]	$NiCoO_4$	49,9	-0,4	48,9	-2,0	-	1,08
3	$Ni_{0,75}Co_{2,25}O_4$	74,4	-0,9	24,5	-1,6	-	1,05
4	$NiCo_2O_{4-350°C}$	66,3	-0,7	32,8	-1,3	-	0,82
5	$NiCo_2O_{4-550°C}$	65,9	-1,3	33,2	-0,1	-	0,89
6	0,5 wt%Pd/$NiCo_2O_4$	65,4	-1,5	32,6	-1,4	0,79+58%	1,17

[a] synthesized for Specialization Project, A16.
[b] second analysis.

4.1.4 Raman Spectroscopy

Figure 4.3 displays the results from the Raman spectroscopy analyses. Three Raman shifts were visible in all spectra at around 190, 470 and 670 cm^{-1}. In addition, the Raman spectra for $NiCoO_4$ and $Ni_{0,75}Co_{2,25}O_4$ displayed slight peaks around 518, as can be seen in Figures 4.3a and 4.3c, respectively. This peak was not detected for $NiCo_2O_4$, and is thus marked by a question mark in Figure 4.3b. $NiCo_2O_4$ and $Ni_{0,75}Co_{2,25}O_4$ displayed peaks around 611. The Raman vibrational modes for the spinel structure are F_{2g-1}, E_g, F_{2g-2}, F_{2g-3} and A_1, and for Co_3O_4 they are identified at 194, 482, 522, 618 ams 691 cm^{-1}, respectively.

According to Ezeigwe et al. (2017, [37]) Raman peaks at 186, 477, 523 and 671 cm^{-1} relate to the vibrational models of the Co-O and Ni-O bonds in $NiCo_2O_4$.

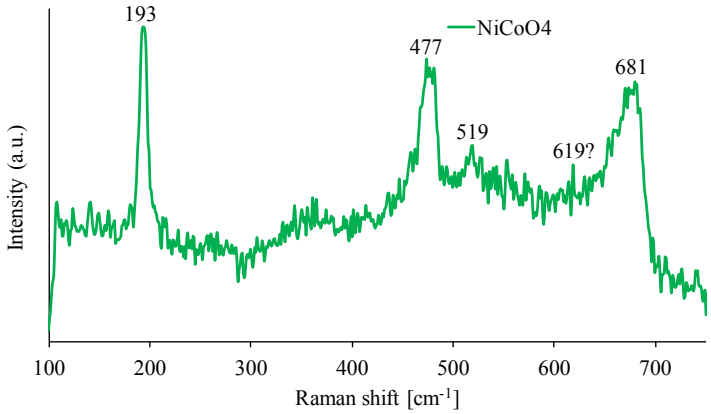

(a) Raman shift for $NiCoO_4$.

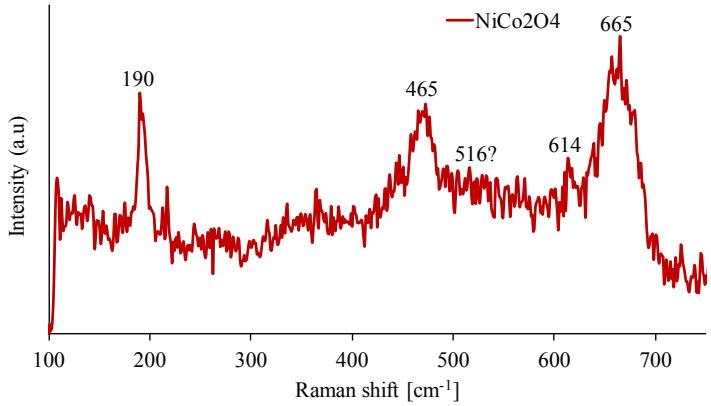

(b) Raman shift for $NiCo_2O_4$.

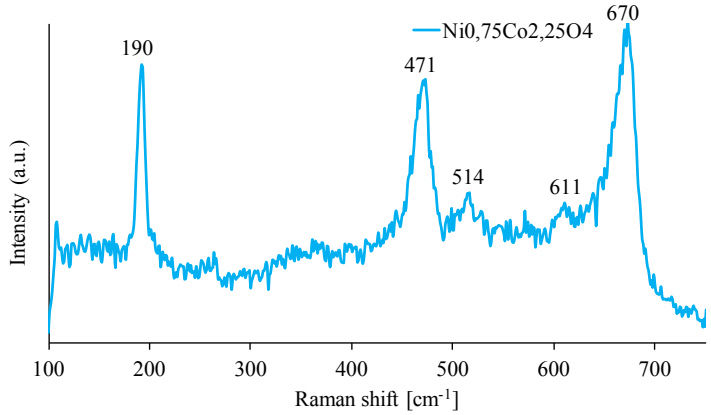

(c) Raman shift for $Ni_{0,75}Co_{2,25}O_4$.

Figure 4.3: Raman shifts over three catalysts with different Ni/Co-ratios.

4.1.5 Transmission Electron Microscopy

Figure 4.4a presents a TEM image over the particle system of 0,5 wt%Pd/$NiCo_2O_4$. The crystallites of $NiCo_2O_4$ were found to agglomerate into larger plates, and Figure 4.4b presents a High Resolution TEM image of the crossection structure of such a plate. The crystallite sizes of $NiCo_2O_4$ within the agglomerates were between 5 and 10 nm. Figure 4.5 presents the complementary TEM and STEM images for the location of a palladium particle on 0,5 wt%Pd/$NiCo_2O_4$, obtained at increasing resolutions for bright field and HAADF imaging, respectively. The Pd-particle is indicated by a blue box, with increasing resolution. Figures 4.5e and 4.5f indicates the position were the Pd-particle was located. EDXS was utilized to characterize the elements at different points over the particles, and the respective spectra on and next to the particle can be found in Figure 4.6. Several palladium particles were identified at different locations in the studied system, with a size of approximately 2 nm. Figure 4.7 presents a HRTEM image of the structure over another Pd particle identified in the sytem, for bright field and dark field imaging. The respective EDX-spectra are given in Figure 4.8a. In the EDXS-spectra provided the peaks of copper originates from the lattice that the catalyst was investigated on, and the carbon from a film that was spred over the copper lattice.

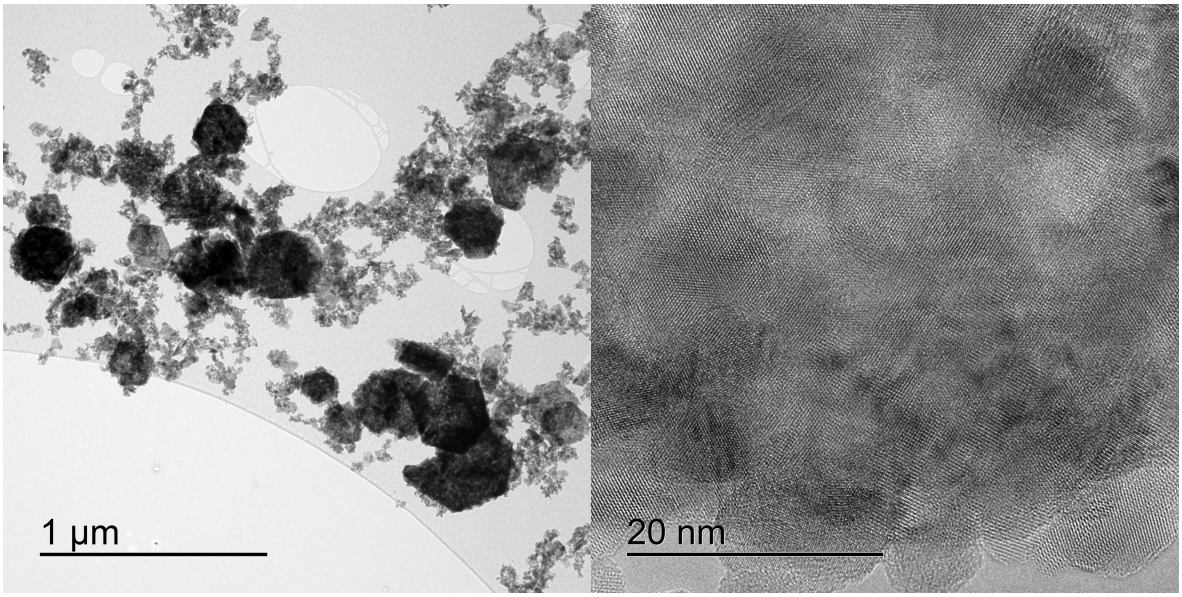

(a) BF TEM image of particle system **(b)** BF High Resolution TEM image of surface

Figure 4.4: BF TEM image and HRTEM image at to different resolution, indicating the structure of the particle system of 0,5 wt%Pd/$NiCo_2O_4$.

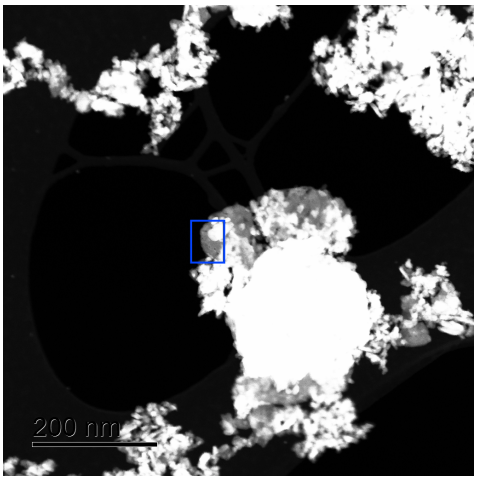

(a) STEM HAADF image

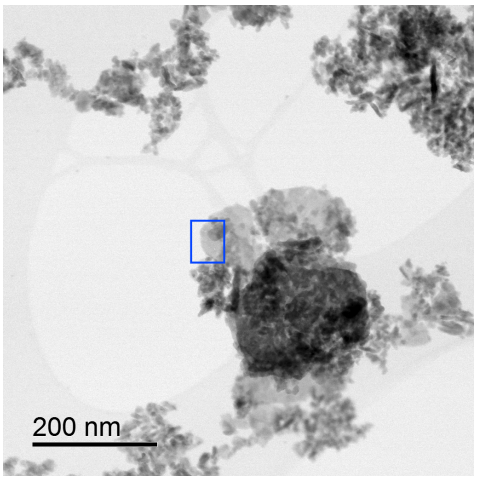

(b) TEM BF image

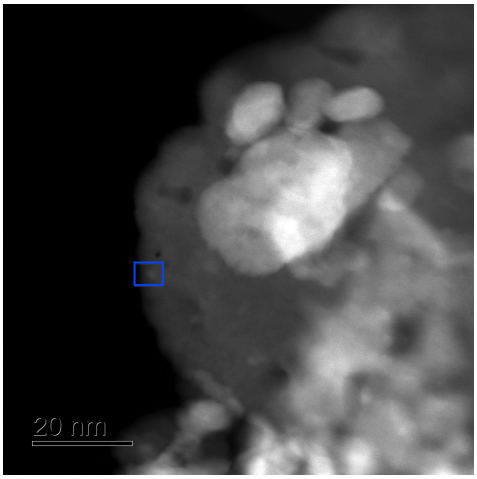

(c) STEM HAADF image

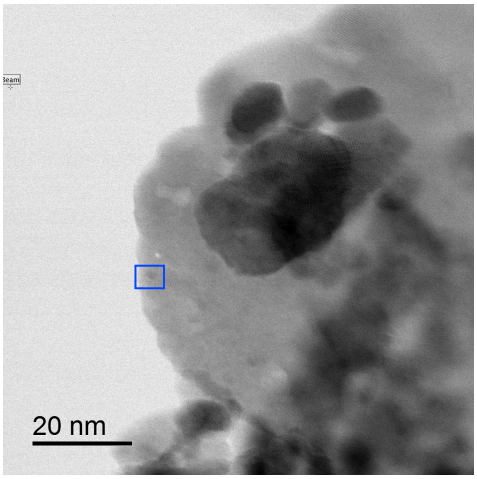

(d) TEM BF image

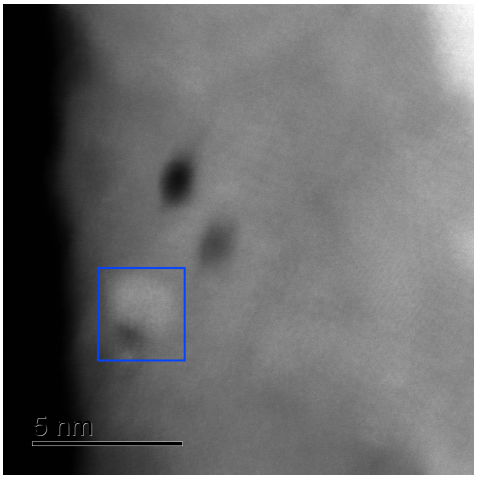

(e) STEM HAADF image

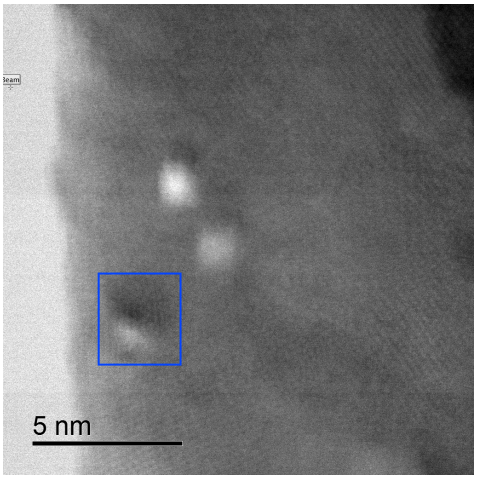

(f) TEM BF image

Figure 4.5: Complmentary HAADF and BF STEM and TEM images for increasing resolutions, indicating the position of a Pd-particle within the blue box in all images. EDXS results on and next to the Pd particle can be reviewed in Figure 4.6.

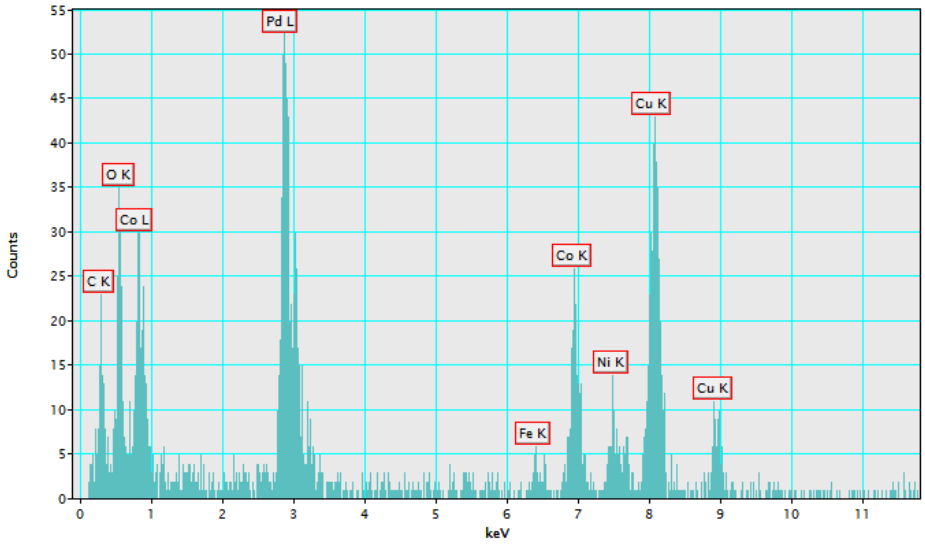

(a) EDXS spectrum on the Pd-particle

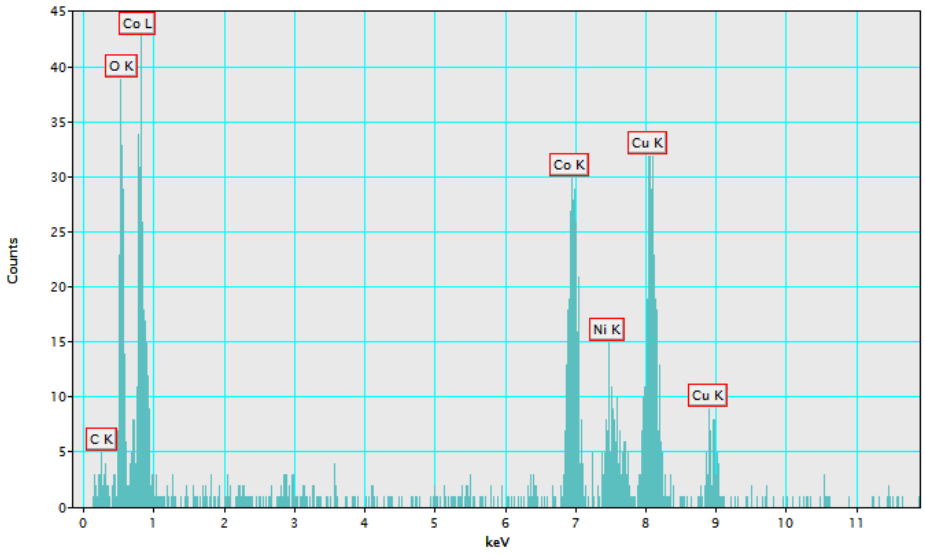

(b) EDXS spectrum next to the Pd-particle

Figure 4.6: EDXS on and next to the particle indicated within the blue box in Figure 4.5.

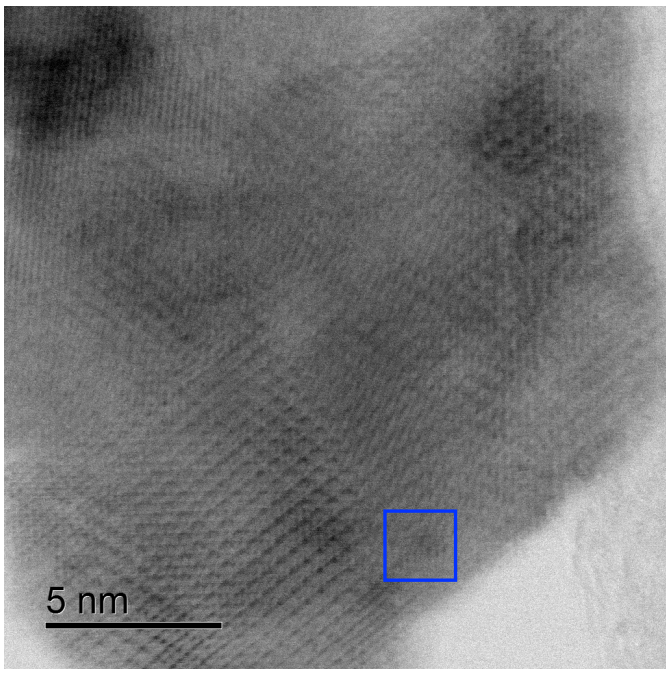

(a) BF TEM image

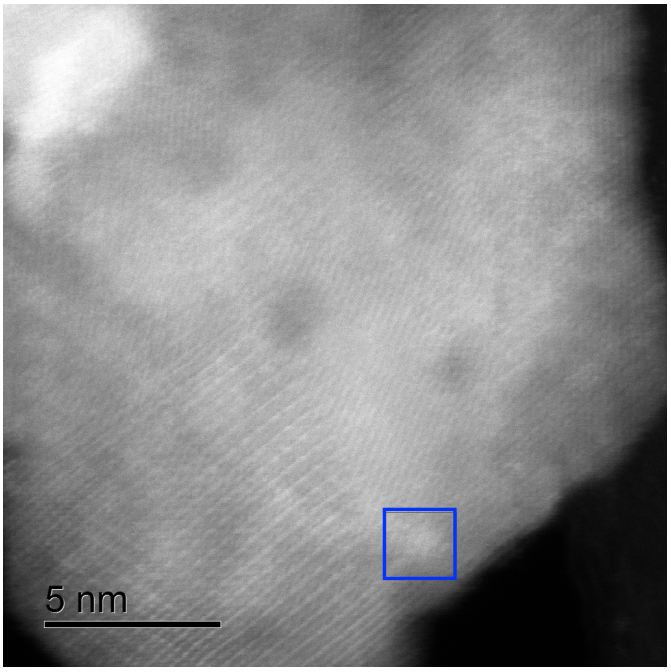

(b) HAADF TEM image

Figure 4.7: Complementary BF and DF images, presenting the lattice structure around the location of a Pd-particle, indicated by the blue box. EDXS spectra on and next to the particle are presented in Figure 4.8.

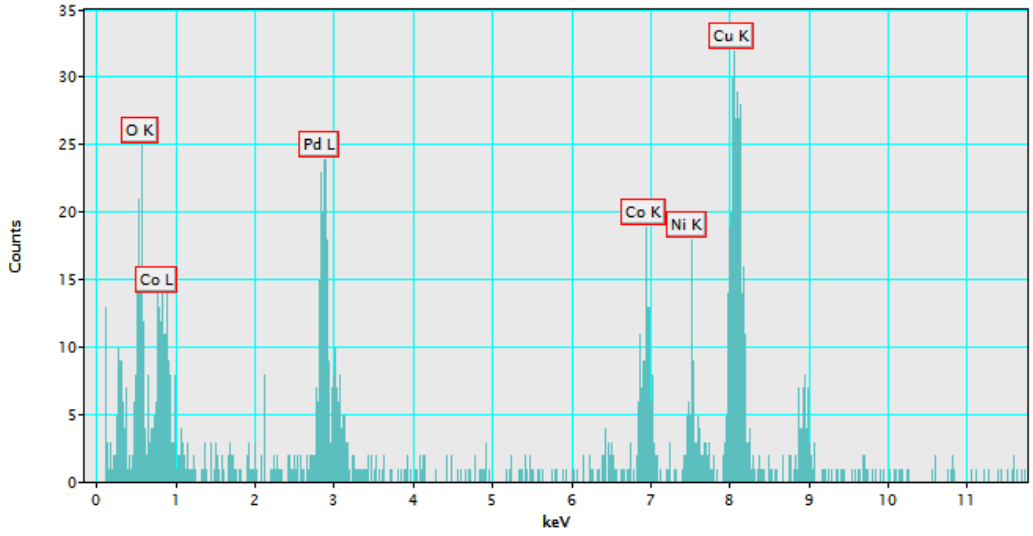

(a) EDXS spectrum on the Pd-particle

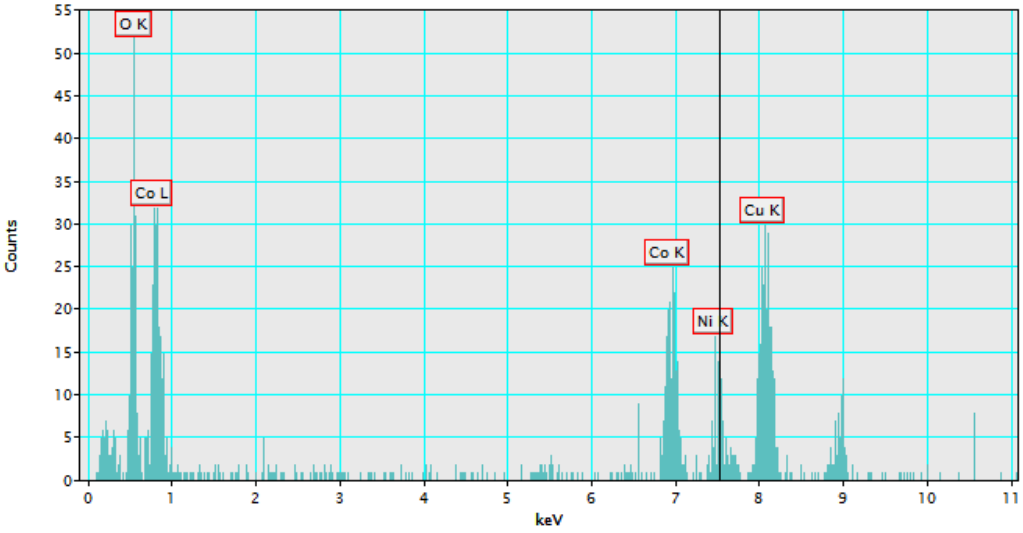

(b) EDXS spectrum next to the Pd-particle

Figure 4.8: EDXS on and next to the particle indicated within the blue box in Figure 4.7.

4.2 Catalyst Activity

The catalysts were tested for catalytic activity by the procedure outlined in Section 3.4. In the following section the obtained results from the conducted research are introduced. In order to gain clarity throughout the large data set, the results have been separated in relation to the investigated parameters. All results were compared to the results of the reference catalyst; Batch 1 of $NiCO_2O_4$. These results are thus presented in multiple tables in the following subsections. The outline of the present section will be further employed in the Chapter 5.2.

The data set from each reaction run entailed two logs, a chromatogram obtained from the μGC and temperature measurements from the thermocouple implemented at the reactor entry. The time stamp on each log entry enabled the conversion, calculated from the GC-chromatogram, to be matched to the respective temperature in the reactor, throughout the reaction. The GC-chromatograms from all runs were investigated for carbon species, and CH_4 and CO_2 were consistently the only detected carbon species in the system. The conversion of methane was thus calculated according to Equation 3.8. Multiple reaction cycles were completed for each run, to ensure accuracy and to investigate potential change in catalytic activity after time on stream. The temperature log from each cycle was used to locate points of prolonged stable temperature, which occurred every 25°C between 200°C and 550°C, for both the heating and the cooling sequence of all reaction cycles. The conversions at these points were plotted against the respective temperatures for both the heating and the cooling sequence, resulting in a plot of the conversion profile such as in Figure 4.9.

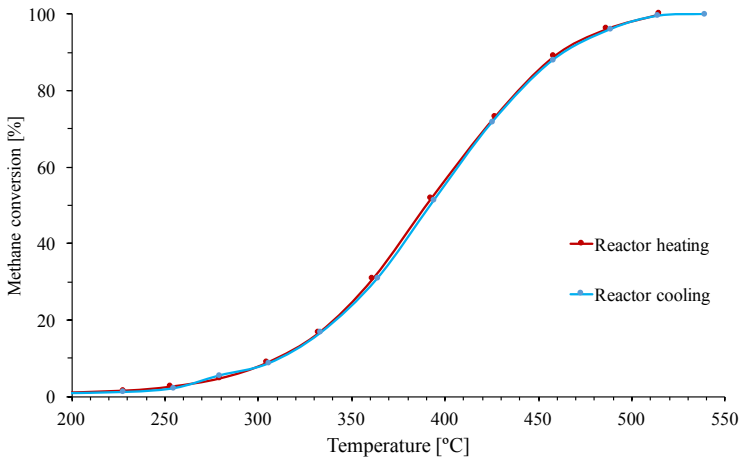

Figure 4.9: An example of the conversion plotted against temperature, for the heating and the cooling sequence of a reaction cycle. The illustrative plot was obtained for the third cycle over the reference catalyst $NiCo_2O_4$ (Batch 1) with 2% CH_4, 10% O_2 and balance N_2, and is denoted Run 1 in Table 4.4.

Matlab was utilized to estimate the necessary temperatures to obtain 10, 30, 50, 70 and 90% methane conversion. The Matlab script, presented in Appendix G, simulated a polynomial curve of the 5th degree based on the identified points of temperature and conversion, such as the points used to plot the curves in Figure 4.9. The temperatures for any level of conversion could thus be extracted from the Matlab script. The catalytic activity of all catalysts for the respective reactant feed concentrations are presented in Table 4.4.

The Matlab script was further utilized to identify the required values for calculation of the apparent activation energy and the reaction rate for the runs. The apparent activation energies, were calculated according to the theory presented in Section 2.6.2. The Matlab script was used to find the temperatures necessary to obtain 10-50% conversion of methane, which were plotted in Arrhenius plot that allowed for calculation of the activation energy. An example of an Arrhenius plot is presented in Figure 4.10, which were calculated from the results from Run 1 (2% CH_4 over $NiCo_2O_4$). Equivalent plots for all runs can be reviewed in Appendix D, and the respective activation energies are presented in the following subchapters.

The Matlab script was additionally utilized to estimate the reaction rate for all runs, by finding the conversion at 325°C, and applying it to Equation 2.7. At 325°C most runs were at a level of conversion under 20%, though the procedure entails certain limitations that will be discussed in the next chapter.

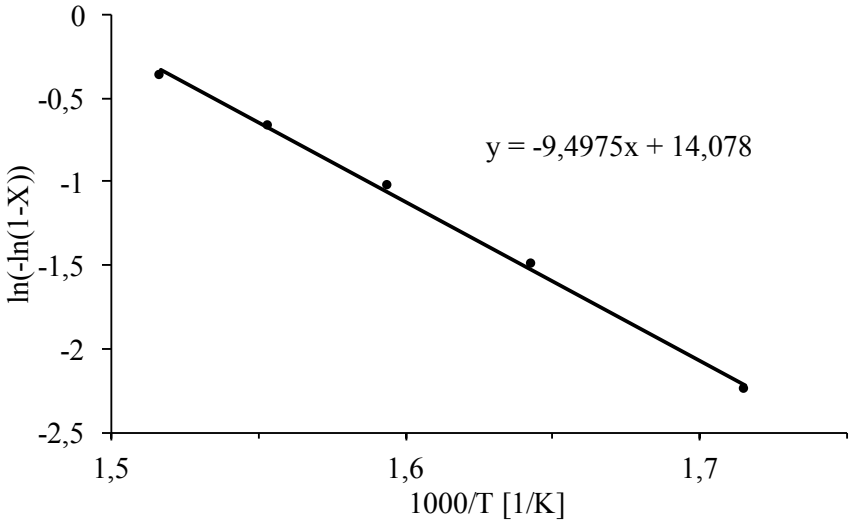

Figure 4.10: An example of an Arrhenius plot, used to estimate the apparent activation energy of methane over the catalyst, E_A. The slope of the curve equals $-E_A/R$, and E_A can thus be found by multiplying the slope with the negative gas constant, $-R$. The illustrative Arrhenius plot was calculated from the results obtained by the reaction over the batch of $NiCo_2O_4$ with 2% CH_4, 10% O_2 and balance N_2, denoted Run 1 in Table 4.4. The activation energy was found to be 70 $kJ\,mol^{-1}$.

The accuracy of the calculated conversion was investigated by calculating the error in the carbon balance over the reaction. This was done according to Equation 3.11, using data from the chromatograms for CH_4, CO_2 and N_2 provided by the μGC. The error was further plotted against complete conversion of methane, as illustrated in Figure 4.11. This illustrative plot was obtained from the measurements in Run 1. Similar plots were made for all runs, and can be reviewed in Appendix E. The error in carbon balance seemed to increase in the system as the methane conversion increased. As can be viewed in Appendix E, the error in carbon balance was highest for the reactant feed comprising the least CH_4. The significance of the carbon error will be discussed further in the next chapter.

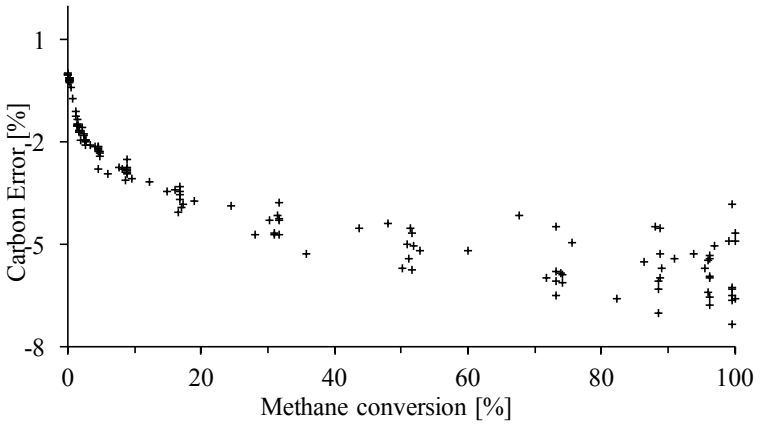

Figure 4.11: An example of the error in carbon balance plotted against conversion of methane, calculated according to Equation 3.11. The illustrative plot was calculated from the results obtained by the reaction over the reference catalyst $NiCo_2O_4$, with 2% CH_4, 10% O_2 and balance N_2, denoted Run 1 in Table 4.4.

The temperature profile over the catalytic bed was not investigated, although it was noted that the maximum measured temperature varied between the catalysts, despite the maximum temperature set point and the methane concentration in the feed being the same. Table 4.3 displays the maximum measured reactor temperature for reaction over Batches 1-5 of catalysts with methane feed concentration 2%. The maximum reactor set point was 550°C.

Table 4.3: The maximum temperature T_{Max} measured in the reactor for reaction over five catalysts with 2% CH_4 in feed. The maximum reactor heater set point was 550°C.

Catalyst	$NiCo_2O_4$	$NiCoO_4$	$Ni_{0,75}Co_{2,25}O_4$	$NiCo_2O_{4-350°C}$	$NiCo_2O_{4-550°C}$
Run	1	6	8	10	12
T_{Max} [°C]	562	552	540	552	564

Table 4.4: The temperatures at different levels of conversion T_X, for all reaction runs. The reactant feed for all runs comprised the specified concentration of CH_4, 10% O_2 and balance N_2, except Runs 4 and 16, which additionally included 15% water (denoted 0,1%$_{H_2O}$). In addition, temperatures at different levels of conversion over two noble metal based catalysts were calculated, with measurements reported by Sandvik [4] (denoted MT16). All temperatures were found using Matlab polynomial estimation, presented in Appendix G.

			Feed	Catalytic Activity				
Batch	**Catalyst**	**Run**	**mol% CH_4**	**T_{10}**	**T_{30}**	**T_{50}**	**T_{70}**	**T_{90}**
1^a	$NiCo_2O_4$	1	2%	310	354	386	418	462
		2	0,5%	290	334	364	392	429
		3	0,1%	296	343	369	390	410
		4^b	0,1%$_{H_2O}$	377	413	437	458	479
		5	0,1%	277	335	363	385	408
2^a	$NiCoO_4$	6	2%	309	352	382	412	451
		7	0,5%	302	343	372	399	433
3	$Ni_{0,75}Co_{2,25}O_4$	8	2%	303	347	378	408	448
		9	0,5%	294	340	370	400	438
4	$NiCo_2O_{4-350°C}$	10	2%	307	349	379	409	450
		11	0,5%	293	343	373	401	431
5	$NiCo_2O_{4-550°C}$	12	2%	314	357	388	419	463
		13	0,5%	302	350	382	411	443
6	0,5wt%Pd/$NiCo_2O_4$	14	2%	294	336	362	388	421
		15	0,1%	259	280	319	338	358
		16^b	0,1%$_{H_2O}$	343	381	400	416	432
		17	0,1%	258	299	321	340	361
$MT16^c$	0,2wt%Pd/Al_2O_3	-	2%	390	440	472	501	538
	2wt%Pd/Al_2O_3	-	2%	303	337	359	379	399

[a] synthesized during Specialization Project, A16.
[b] 15 mol% H_2O in reactant feed.
[c] results calculated with basis on measurements reported by Sandvik [4].

4.2.1 Effect of Catalyst Preparation

Oxide Composition

The dependency of the stoichiometric composition of the catalyst was investigated at two feed concentrations of methane, 2% and 0,5% CH_4. Figure 4.12 shows the conversion of methane plotted against the measured temperature at reactor inlet for the three investigated catalysts, $NiCo_2O_4$, $NiCoO_4$ and $Ni_{0,75}Co_{2,25}O_4$ for both reactant mixtures. The full and dashed lines indicate 2% and 0,5% CH_4 in the reactant feed, respectively. The catalytic activities are presented in Table 4.4 as Runs 1, 2 and 6-9, and the calculated activation energy and reaction rates are presented in Table 4.5. It was noted that all catalysts systematically required lower temperature to reach T_{10}-T_{90} when the feed concentration of CH_4 decreased. $NiCo_2O_4$ displayed slightly lower activity than $NiCoO_4$ and $Ni_{0,75}Co_{2,25}O_4$ for 2% CH_4 and slightly higher for 0,1% CH_4.

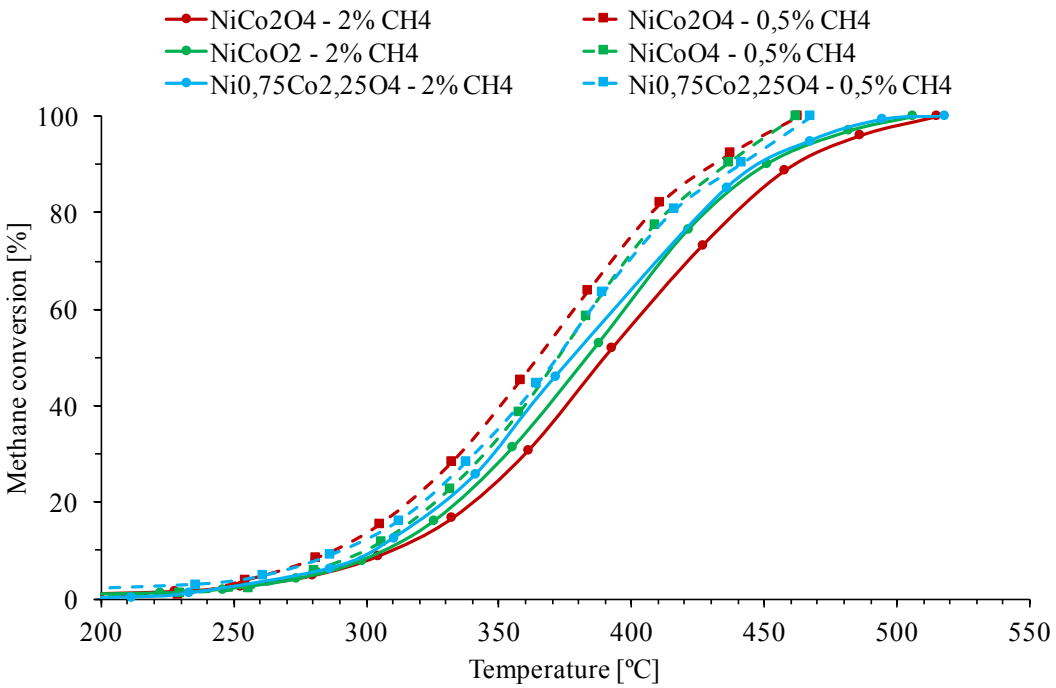

Figure 4.12: The conversion of methane plotted against temperature for two reactions over three catalysts with different Ni/Co-ratio, $NiCo_2O_4$(red), $NiCoO_4$(green) and $Ni_{0,75}Co_{2,25}O_4$(blue). Full line indicates 2% CH_4 in the feed, and dashed line indicates 0,1% CH_4. All runs were complimented with 10% O_2 and balance N_2. The catalytic activities are presented in Table 4.4 as Runs 1, 2 and 6-9.

Table 4.5: Temperature at 90% methane conversion, T_{90}, activation energy, E_A and reaction rate, r, over three catalysts with varying Ni/Co-ratios. The reaction runs can be further reviewed in Table 4.4.

Feed	Batch	Catalyst	T_{90} [°C]	E_A [kJ mol^{-1}]	r [mol h^{-1} g$_{cat}^{-1}$]	Run
2%	1[a]	$NiCo_2O_4$	462	79	0,00033	1
	2[a]	$NiCoO_4$	451	82	0,00034	6
	3	$Ni_{0,75}Co_{2,25}O_4$	448	79	0,00039	8
0,5%	1[a]	$NiCo_2O_4$	429	76	0,00013	2
	2[a]	$NiCoO_4$	433	83	0,00010	7
	3	$Ni_{0,75}Co_{2,25}O_4$	438	75	0,00015	9

[a] synthesized during Specialization Project, A16.

Calcination temperature

Figure 4.13 shows the conversion plotted against temperature for the first reaction cycle over $NiCo_2O_4$ calcined at two different temperatures. 4.13a shows $NiCo_2O_4$ calcined at 350°C, presented as Batch 4 in Table 4.4. 4.13b shows the catalyst calcined at 550°C, denoted Batch 5 in Table 4.4.

Figure 4.13a shows that $NiCo_2O_{4-350°C}$ exhibit superior activity in the heating sequence of the first cycle over fresh catalyst, compared to that of the cooling sequence. The first cycle over fresh catalyst for $NiCo_2O_{4-550°C}$, presented in Figure 4.13b, exhibited similar features for both the heating and the cooling sequence. Further reaction cycles indicated that the initial activity over fresh catalyst for $NiCo_2O_{4-350°C}$ decreased and stabilized at an activity level close to that of $NiCo_2O_{4-550°C}$. This is graphed in Figure 4.14, which shows the activities for both catalysts after multiple reaction cycles. The activation energy and reaction rate for the runs graphed in Figure 4.14 are presented in Table 4.6, and confirm that both catalysts exhibit similar features after the first cycle. The catalytic activities are presented in Table 4.4 in Runs 10-13.

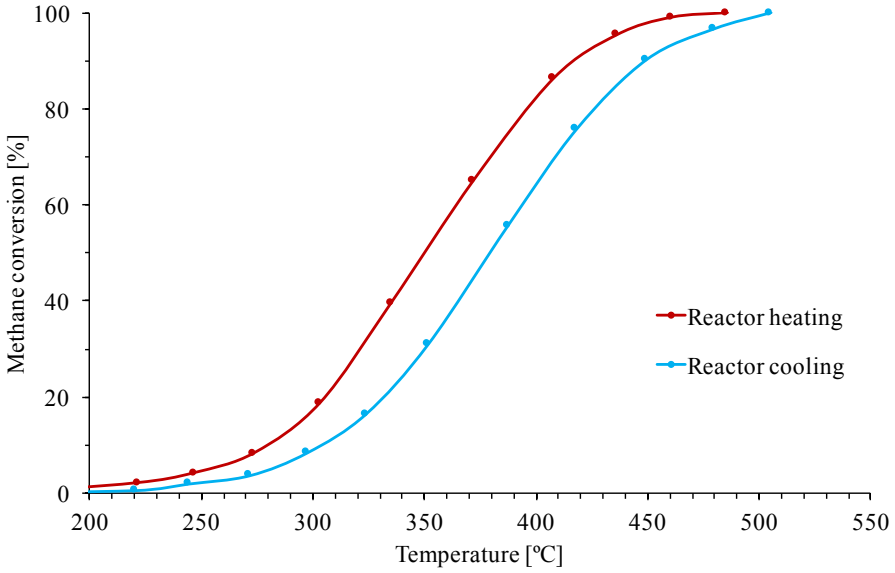

(a) First cycle over fresh $NiCo_2O_4$ catalyst calcined at 350°C.

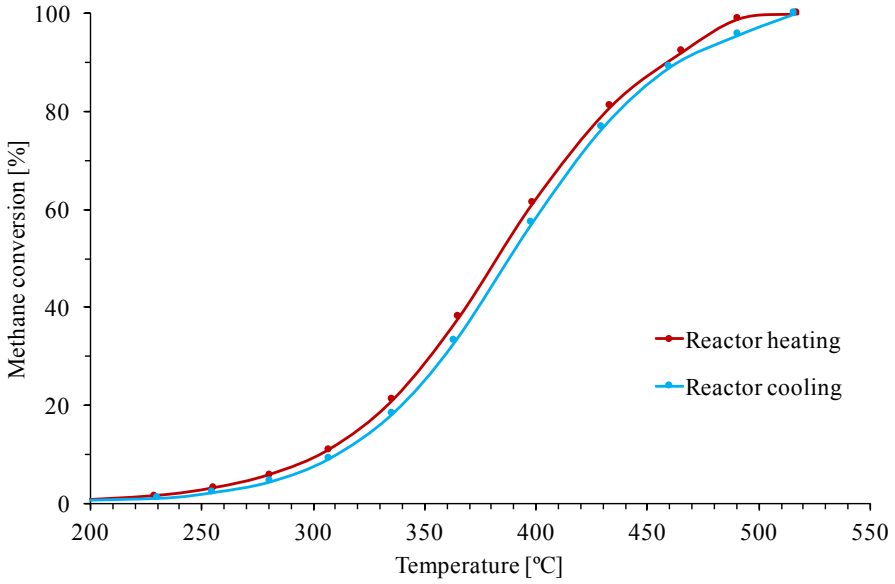

(b) First cycle over fresh $NiCo_2O_4$ catalyst calcined at 550°C.

Figure 4.13: Conversion of methane plotted against temperature for the heating and cooling sequence over fresh catalyst for **(a)** $NiCo_2O_{4-350°C}$ and **(b)** $NiCo_2O_{4-550°C}$, with reactant feed 2% CH_4, 10% O_2 and balance N_2.

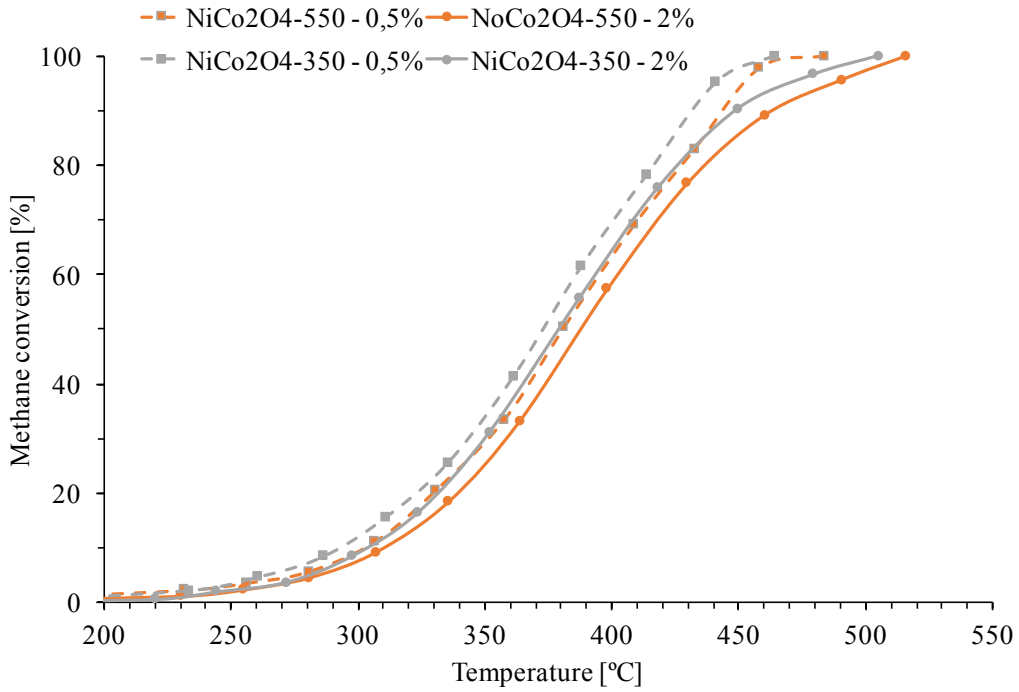

Figure 4.14: The conversion of methane plotted against temperature after multiple reaction cycles over $NiCo_2O_4$ calcined at 350°C and 550°C, indicated by gray and orange respectively. Full and dashed line respectively indicate 2% and 0,5% CH_4 in reactant feed, with 10% O_2 and balance N_2. The reactions can be reviewed as Runs 10-13 in Table 4.4.

Table 4.6: Temperature at 90% conversion, T_{90}, activation energy, E_A, and reaction rate, r, for two batches of $NiCo_2O_4$ calcined at different temperatures, 350°C and 550°C for Batch 4 and 5, respectively. $NiCo_2O_{4-350°C}$ exhibited superior activity during the first cycle, which decreased and stabilized at the second cycle. r and E_A are calculated based on the measurements made from the third reaction cycle.

Feed	**Batch**	**Catalyst**	**T_{90}** [°C]	**E_A** [kJ mol^{-1}]	**r** [mol h^{-1} g$_{cat}^{-1}$]	**Run**
2%	4	$NiCo_2O_{4-350°C}$	448	82	0,00037	10
	5	$NiCoO_{4-550°C}$	450	82	0,00030	12
0,5%	4	$NiCo_2O_{4-350°C}$	438	72	0,00011	11
	5	$NiCoO_{4-550°C}$	431	73	0,000095	13

4.2.2 Effect of Methane Concentration

Figure 4.15 shows the methane conversion plotted against temperature for reactions with three reactant feed compositions over $NiCo_2O_4$. All plotted reactops are after frist reaction cycle. Full, long dashed and small dashed line indicates 2%, 0,5% and 0,1% CH_4 in feed, respectively. The temperature necessary to obtain full conversion, T_{90} decreased systematically with decreasing methane concentration, which can be reviewed in Run 1-3 Table 4.4. It was also noted that the shape of the curves tended towards a sharper S-shape for 0,1% CH_4, than for the other two reactant feed compositions. The calculated apparent activation energy and reaction rate for the three runs are presented in Table 4.7.

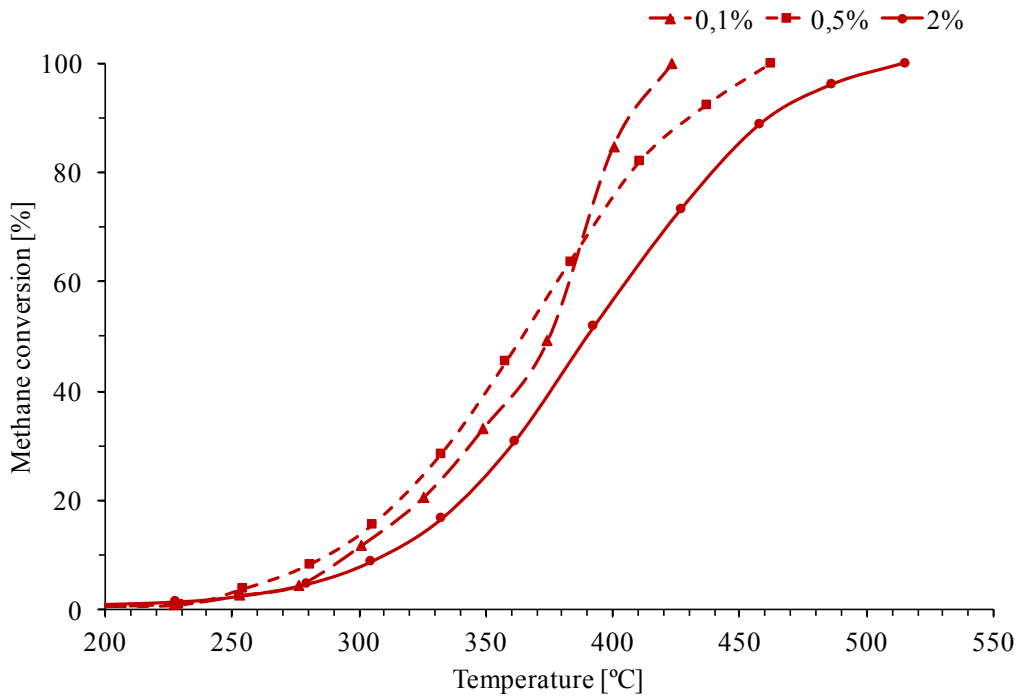

Figure 4.15: The conversion of methane plotted against temperature over $NiCo_2O_4$ for three feed concentrations of methane, 2%, 0,5% and 0,1%, respectively indicated by full, short dashed and long dashed lines. In addition to methane the reactant feed contained 10% O_2 and balance N_2. The reactions can be reviewed as Runs 1-3 in Table 4.4.

4.2.3 Effect of Palladium

The effect of Pd deposition on $NiCo_2O_4$ was investigated for two reactant feeds with 2% and 0,1% CH_4. The methane conversion plotted against temperature, and is presented in Figure 4.16, togehter with the equivalent results from the reference catalyst $NiCo_2O_4$. The figure

shows that the deposition of Pd enhanced the catalytic activity for both feed compositions. The previously observed sharpening of the curve indicating 0,1% CH_4 was also observed for 0,5wt%Pd/$NiCo_2O_4$.

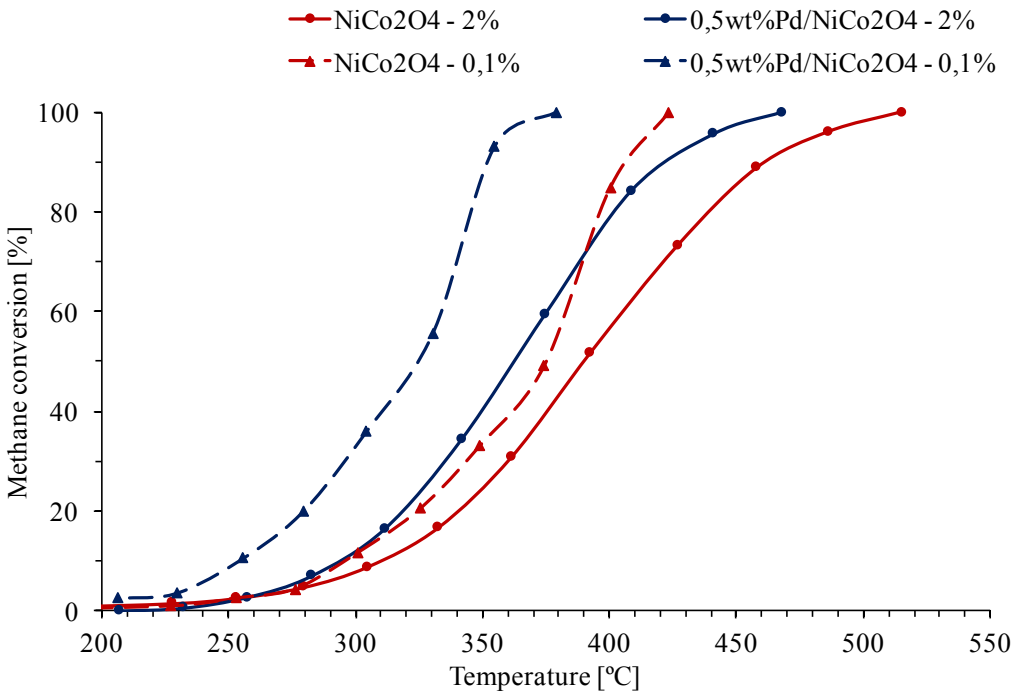

Figure 4.16: The conversion of methane plotted against temperature over $NiCo_2O_4$ (red) and 0,5wt%Pd/$NiCo_2O_4$ (blue), for two feed concentrations of methane, 2% and 0,1%, indicated by full and dashed line, respectively. In addition to methane the reactant feed contained 10% O_2 and balance N_2. The reactions can be reviewed as Runs 1, 3, 14 and 15 in Table 4.4.

The apparent activation energies and reaction rates for the runs plotted in Figure 4.16 are presented in Table 4.7. The table additionally contains results calculated based on the research performed by Helene Sandvik the spring 2016. Sandvik completed her Master thesis *Catalysis for Control of Methane Slip in Marine Machinery Using a Palladium Based Catalyst* for the Catalysis group at NTNU June 2016, and the catalytic activity experiments were executed in the same reaction rig used in the present work. Considering the similarities between the experimental procedure, the results obtained by Sandvik were assumed to be fit for comparison to the activity of the present researched materials. To investigate the possibility of a synergic effect between the palladium and $NiCo_2O_4$ in 0,5wt%Pd/$NiCo_2O_4$, the reaction rate of methane conversion over the catalytic materials were calculated on the basis of amount of palladium, according to Equation F.3 in Appendix F.2. Sandvik produced two catalysts with palladium deposited on Al_2O_3 with weight fraction 0,2wt% and 2wt%. 0,5wt%Pd/$NiCo_2O_4$ could thus not be directly compared to Sandvik's results, due to the different loading on the catalysts.

Table 4.7: Temperature at 90% conversion, T_{90}, activation energy, E_A, and reaction rate per gram catalyst and per gram palladium, r and r_{Pd}, for $NiCo_2O_4$, 0,5wt%Pd/$NiCo_2O_4$ (Batch 1 and 6, respectively) and for two palladium based catalysts produced by Sandvik [4], 0,2wt%Pd/Al_2O_3 and 2wt%Pd/Al_2O_3.

Batch	**Catalyst**	**Feed**	$\mathbf{T_{90}}$ [°C]	$\mathbf{E_A}$ [kJ/mol]	**r** [mol/h g_{cat}]	$\mathbf{r_{Pd}}$ [mol/h g_{Pd}]	**Run**
1[a]	$NiCo_2O_4$	2%	462	79	0,00033	-	1
		0,5%	429	76	0,00010	-	2
		0,1%	410	69	0,00002	-	3
6	0,5wt%Pd/$NiCo_2O_4$	2%	421	82	0,0005	1,0	14
		0,1%	358	82	0,00006	-	15
MT16[b]	0,2wt%Pd/Al_2O_3	2%	538	95	0,0001	0,89	-
	2wt%Pd/Al_2O_3	2%	399	102	0,001	0,55	-

[a] synthesized during Specialization Project, A16.
[b] results calculated with basis on measurements reported by Sandvik [4].

4.2.4 Effect of Water

The effect of water in the reactant feed was of interest to investigate the catalytic performance in an environment closer to realistic exhaust gas conditions. The effect of water was investigated for the reference catalyst, $NiCo_2O_4$, and for 0,5wt%Pd/$NiCo_2O_4$. Figure 4.17 shows the methane conversion plotted against temperature for Runs 1-3 and 15-17 in Table 4.4. Red and blue respectively represent reaction over $NiCo_2O_4$ and 0,5wt%Pd/$NiCo_2O_4$. Long dashed line indicates the preliminary reaction with 0,1% CH_4, which was followed by a reaction with equal methane concentration and 15% H_2O indicated by full line. The catalytic activity was found to decrease significantly in the presence of water. The former reaction conditions were thus repeated, to investigate if the observed catalytic deactivation was reversible. It was observed that the catalytic activities for 0,1% CH_4 exhibited similar features, regardless of H_2O exposure between runs. The calculated apparent activation energy and reaction rate for the runs are presented in Table 4.8.

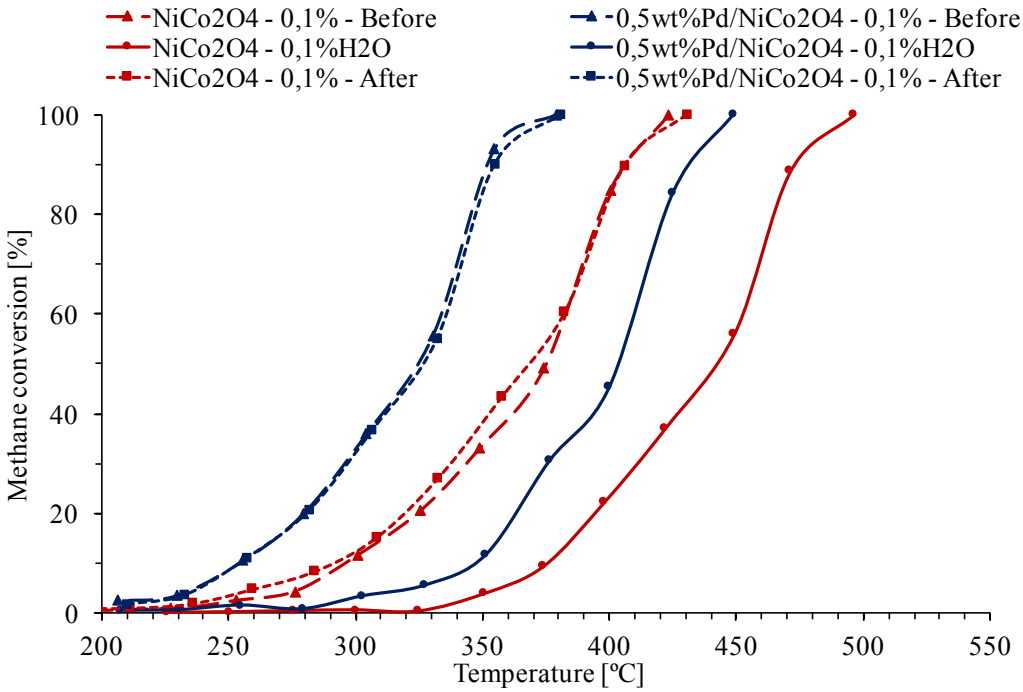

Figure 4.17: The conversion of methane plotted against temperature for three subsequent runs over $NiCo_2O_4$ (red) and 0,5wt%Pd/$NiCo_2O_4$ (blue). Long dashed line indicate 0,1% CH_4, and full line indicates the addition of 15% H_2O to the feed, 0,1%$_{H_2O}$. The former reactant feed was repeated after running reaction with H_2O, indicated by the short dashed line. All reactant feeds were complimented with 10% O_2 and balance N_2. The reactions can be reviewed as Runs 3-5 and 15-17 in Table 4.4.

Table 4.8: Temperature at 90% conversion, T_{90}, activation energy, E_A, and the reaction rate, r, for three subsequent runs over $NiCo_2O_4$ and 0,5wt%Pd/$NiCo_2O_4$. The intermediate run contained 15% H_2O in the reactant feed, which caused a reversible loss of catalytic activity for both catalysts.

Batch	**Catalyst**	**Feed**	**T_{90}** [°C]	**E_A** [kJ mol^{-1}]	**r** [mol h^{-1} g$_{cat}^{-1}$]	**Run**
1[a]	$NiCo_2O_4$	0,1%	410	69	0,00002	3
		0,1%$_{H_2O}$	479	120	0,000001	4
		0,1%	408	64	0,00002	5
6	0,5wt%Pd/$NiCo_2O_4$	0,1%	358	82	0,00006	15
		0,1%$_{H_2O}$	432	112	0,000007	16
		0,1%	361	79	0,00006	17

[a] synthesized during Specialization Project, A16.

Chapter 5

Discussion

5.1 Catalyst Characterization

In the following section the different characterization results will be discussed in unison for the different investigated aspects, with focus on catalyst synthesis, oxide composition and structural properties, and the effect on structural properties by calcination temperature and palladium deposition.

The accuracy of the characterization techniques of XRD, N_2 physisorption and XRF were investigated by repeated analyses over the reference catalyst $NiCo_2O_4$. Information about reproducibility of the experimental protocol are assembled in Appendix C. Figure C.1 presents the XRD-spectra of two analyses of the reference catalyst $NiCo_2O_4$. The two spectra displayed highly similar features, and the method of XRD analysis was thus deemed accurate. The small deviations between two analyses over the reference catalyst for the methods of XRF and BET indicated that also these techniques were conducted with high accuracy.

5.1.1 Synthesis of Metal Oxide

The activity of the catalysts produced in the present work was not investigated for dependency of synthesis conditions. Pu et al (2017 [18]) report that the activity of methane combustion over Co_3O_4 depends on the aging time during coprecipitation. A similar effect over $NiCo_2O_4$ was not investigated in the present work, although procedure inaccuracy could have influenced the synthesized materials. The aging time was not considered during the synthesis, but may have contributed to differences in the activity of the final products. Even though the catalysts were synthesized as similarly as possible, the procedure was conducted faster for the catalysts produced at the end of the experimental work compared to those produced in the beginning. This was due to familiarity to the experimental procedure after it had been completed several times. In addition, certain catalysts was left to stir for a while, as other work was conducted, while other catalysts were completed in one continuous process. This might have induced an unintentional aging time for certain catalysts, which could have influenced the final catalytic

activity. Further, a general obstacle with mixed oxide catalysts is that the exact active site on the catalyst is unknown. This impedes the possibility to tune the catalyst preparation to increase the amount of active sites.

Compared to the theoretical mass percentages (in Table C.1 in Appendix C), all catalysts seem to have precipitated with high accuracy of the desired composition according to the XRF measurements presented in Table 4.2. The first and second analysis of the reference catalyst indicated that the reproducibility of the XRF procedure was acceptable, with a deviation of less than $\pm 2\%$. All batches precipitated with equal stoichiometric ratio to the reference catalyst (Batch 1), Batches 4, 5 and 6 are within the deviation limit of the reference catalyst, indicating that they contain approximately equal ratio of nickel and cobalt. This further indicate that the increased calcination temperature for Batch 5 did not influence the ratio of nickel and cobalt in the material. However, as previously mentioned, all conditions during coprecipitation can influence the catalytic properties, possibly including the volume of the precipitation reactor. Batch 1, 4 and 6-support (support for palladium deposited catalyst) were synthesized with the same calcination temperature, however, the two latter were produced in a batch twice the size of Batch 1. The XRD spectra of these three batches of catalyst are thus presented together in Figure C.2 in Appendix C. The three spectra exhibit highly similar characteristic features, indicating that the catalytic synthesis was reproducible also with regards to the present phases. This was corroborated by resembling values of surface area and pore volume obtained from N_2 physisorption. Further potential deviations between the catalysts with equal stoichiometry and calcination treatment can be investigated by comparing the activities of Runs 1 and 10 and 2 and 11 on the basis of catalyst reproduction.

All six batches of catalyst included traces of potassium, ranging from 0,8 to 1,2mass%. This impurity could be traced to either the catalyst syntheses or the XRF analyses. The XRF measurements were not executed simultaneously, and the utilized equipment was washed between each analysis. As all catalysts display relatively equal amounts of potassium, it is more likely that the impurity originated from the catalyst syntheses. The precipitation agent used for the catalyst synthesis was KOH, and insufficient washing of the precipitated crystallites or potassium being incorporated to the lattice may have caused the impurity. This presumption is corroborated by the potassium measured amounts in $NiCo_2O_{4-350°C}$ and $NiCo_2O_{4-550°C}$, that are close to equal, 0,82 and 0,89mass% respectively. The two catalysts were synthesized together, but prepared for XRF separately. As they comprise close to equal amounts of impurity, it is likely that this impurity originates from the synthesis.

5.1.2 Oxide Composition

Reference Catalyst

The reference catalyst was found to be an adequate catalyst for comparison, as the reproducibility of the catalyst was high, due to the arguments discussed above. Based on the similarity of the obtained values of XRF mass%, BET surface area and XRD-crystallite sizes for catalyst batches 1, 4 and 6-support, the synthesis procedure was generally regarded to have been executed with high reproducibility.

The BET-results from the two measurements done for the reference catalyst, $NiCo_2O_4$, were found to display acceptable deviations, indicating that the method for N_2 physisorption had satisfactory reproducibility. However, a deviation of at least ±4% should be accounted for when regarding the results provided in Table 4.1. If the results from the reference catalyst (denoted Batch 1) are compared to Batches 4 and 6-support (denoted 6^c in Table 4.1), the deviation is higher. The surface area of Batch 6 is within the ±4% deviation range. Batch 4, however, exceed this limit. As presented in Section 2.3.1 the material properties, such as surface area and pore volume, are highly dependent on the conditions during coprecipitation. Although the three mentioned batches were synthesized as accurately as possible, the properties of the batches may differ, for instance because of unintentional differences in aging time. This may affect the properties of the finished catalyst, implying that the measured difference between surface area of Batch 4 and the reference catalyst might be correct.

Change in Ni/Co-Ratio

The difference in oxide stoichiometry between catalyst batches 1-3, is clear when regarding the results reported from the XRF analyses in Table 4.2. All catalysts match their respective nominal loading with less than 2% deviation. However, the consequences of the variations of stoichiometric composition are not equally clear in all characterization techniques. All three XRD spectra for the three materials with different Ni/Co-ratio are presented in Figure 4.1, and seems to exhibit similar characteristic features. However, with basis on the stoichiometric spinel $NiCo_2O_4$, $NiCoO_4$ and $Ni_{0,75}Co_{2,25}O_4$ seem to alter in opposite fashions. $NiCoO_4$ display broader peaks than $NiCo_2O_4$, and $Ni_{0,75}Co_{2,25}O_4$ display more narrow peaks.

The BET method is useful to identify the total surface area of a material, but less so in providing information about the activity of this area, [21]. For a supported metal catalyst, the active surface area is usually determined by methods such as chemisorption. For transition metal oxides, this would prove unsatisfactory, as the active surface area is dependent on the surface composition, and on the interaction between vacancies and neighboring species on the

surface. Although the surface area and the activity thus may be unrelated, a large surface area is in most instances found to be beneficial. By reviewing the measured BET-area in Table 4.1, there seem to be a trend of decreasing specific surface area by decreasing nickel amount in the catalysts. However, the trend observed in the BET area, may not be correlated to a trend in the activity measurements.

5.1.3 Catalyst Structure

Reference Catalyst

The XRD spectrum of the reference catalyst, $NiCo_2O_4$ is presented in Figure 4.1, and displays the characteristic features matching those to the phase of $NiCo_2O_4$. However, as reported by Lim et al. (2015 [19]) Co_3O_4 and $NiCo_2O_4$ comprise the same spinel structure with small differences in lattice parameters, 8,084 Å and 8,110 Å, respectively. This implies that they can be difficult to differentiate in a XRD-spectrum. The presence of Co_3O_4 can thus not be discarded from the analyzed catalyst. If Co_3O_4 were to be present in the system, this would imply that the catalyst displayed separate phases of nickel, in a state that was undetectable for the XRD-analysis. No separate nickel phases were detected by the XRD, although the possibility of an amorphous nickel phase can not be discarded. However, the nickel phase comprise 1/3 of the metal ions in the catalyst, so the phase of $NiCo_2O_4$ seem to be a better stoichiometric fit for the system.

The peaks of the XRD spectrum was of a broad nature, that indicated small $NiCo_2O_4$ crystallites. By investigation of the peaks with the Scherrer equation, the crystallite sizes were found to be about 6 nm. This was in compliance with the TEM measurements made of catalyst 6, where the $NiCo_2O_4$ crystallites of 0,5wt%Pd/$NiCo_2O_4$ were observed in the size range between 5 and 10 nm. However, it should be noted that the impregnation of palladium may have induced a structural change to the catalyst, compared to the reference catalyst. For instance, the crystallite size obtained from XRD investigation of 0,5wt%Pd/$NiCo_2O_4$ was found to be slightly lower after impregnation of Pd (6,3 nm before impregnation and 5,8 nm after). The TEM image in Figure 4.4a presents how the crystallites agglomerate into larger particles. According to the observations, the crystallites form larger plate-like structures, with a joint lattice structure, as can be viewed by the lattice cross section in the HRTEM image in Figure 4.4. The BF TEM image in Figure 4.5d indicate how the crystallites are placed on top of each other within the larger plates.

Effect of Oxide Composition

With basis on the stoichiometric spinel $NiCo_2O_4$ in Figure 4.1, $NiCoO_4$ and $Ni_{0,75}Co_{2,25}O_4$ seem to alter in opposite fashions. $NiCoO_4$ display broader peaks than $NiCo_2O_4$, and $Ni_{0,75}Co_{2,25}O_4$ display more narrow peaks.

The spectrum of $NiCoO_4$ indicates that most cobalt have precipitated in the phase of $NiCo_2O_4$. According to the XRF analysis, the catalyst does comprise a 1:1 ratio of nickel and cobalt, which leaves an excess of nickel in the system. The phase of the nickel surplus is more difficult to identify, and an interesting field of study. The magnitude of the peak identified around $2\theta = 44°$ and the slight shoulder identified around $2\theta = 63°$ might suggest that small amounts of crystalline NiO are present in the system. It is uncertain if the amount of NiO balances the stoichiometry of the system. It is possible that a larger fraction of nickel oxide was undetected by the scan due to very small crystallite sizes, or that NiO has precipitated amorphously, [21]. As nickel is identified to be in stoichiometric surplus by the XRF-analyses, it is logical to assume that cobalt have precipitated in the phase of $NiCo_2O_4$, rather than Co_3O_4. However, the presence of Co_3O_4 in the catalyst can not be completely discarded without further investigation.

The blue spectrum in Figure 4.1 represent the catalyst with a stoichiometric deficit of nickel, $Ni_{0,75}Co_{2,25}O_4$. It is possible that the surplus of cobalt ions simply have precipitated as divalent cations and occupy vacancies in tetrahedral sites, originating from the nickel deficit. As $NiCo_2O_4$ and Co_3O_4 exhibit almost indistinguishable lattice parameters, regions of Co_3O_4-phase within the lattice, or as separate crystallites, would maintain the spinel structure with the characteristic features displayed in the XRD-spectrum.

The crystallite sizes for the $NiCo_2O_4$-phase in the three catalysts were found to be 4,7 nm, 6 nm and 9,1 nm for $NiCoO_4$, $NiCo_2O_4$ and $Ni_{0,75}Co_{2,25}O_4$, respectively. The increase of crystallite size upon decreasing nickel amount was indicated by the nature of the peaks presented in Figure 4.1, although more extensive investigation would be necessary to determine the cause of this trend. In $NiCoO_4$ the NiO phase was about 2,8 nm. The specific surface area of $NiCo_2O_4$, $NiCoO_4$ and $Ni_{0,75}Co_{2,25}O_4$ presented in Table 4.1, show that the surface area seems to decrease with decreasing nickel amount in the catalyst. This is in coherence with the XRD investigation, as increased crystallite sizes implies smaller surface area. However, the pore volume does not necessarily decrease by the same trend. Although $NiCoO_4$ was found to have higher surface area, it comprised smaller pore volume than $NiCo_2O_4$. This may indicate that the former catalyst has more pores than the latter, but that the pores are of a smaller and more narrow nature than the ones in $NiCo_2O_4$. $Ni_{0,75}Co_{2,25}O_4$ have both smaller surface area and pore volume than $NiCo_2O_4$, indicating that $Ni_{0,75}Co_{2,25}O_4$ have fewer or smaller pores than the reference catalyst. The differences in pore volumes are however small for the studied catalysts, and it is questionable if this variable may influence the catalytic activity.

$NiCo_2O_4$, $NiCoO_4$ and $Ni_{0,75}Co_{2,25}O_4$ were studied with Raman spectroscopy in the range of 100-3000 cm^{-1}, but the spectra presented in Figure 2.7 were overcome by fluorescence beyond the presented range. Raman spectroscopy was employed to the three catalysts to investigate potential differences between the stoichiometrically different catalysts. However, in resemblance to the respective XRD-spectra, the Raman spectra for the three catalysts employ highly similar features.

There is little research regarding Raman spectroscopy over $NiCo_2O_4$, although Eizeigwe et al. (2017 [37]) report that Raman spectroscopy of $NiCo_2O_4$ prepared by coprecipitation, displayed Raman shift around 186, 477, 523 and 671 cm^{-1} that correspond to the F_{2g}, E_g, F_{2g} and A_{1g} models of $NiCo_2O_4$ respectively. More research has been applied to the more common spinel Co_3O_4. The vibrational modes relating to F_{2g-1}, E_g, F_{2g-2}, F_{2g-3} and A_{1g} for Co_3O_4 can be reviewed in a Raman spectra at 194, 484, 522, 618 and 691 cm^{-1}, [17]. As mentioned, the lattice parameters for $NiCo_2O_4$ and Co_3O_4 are highly similar, which is from neighboring atoms in the transition metal block in the periodic table. The similarities between cobalt and nickel atoms, are likely to imply that the Raman spectra for $NiCo_2O_4$ and Co_3O_4 will exhibit similar features.

Clear peaks were found for all spectra presented in Figure 4.3 around 190, 471 and 670 cm^{-1}, which correspond to the vibrational modes of F_{2g-1}, E_g and A_{1g}, respectively. Additionally, the spectra for $NiCoO_4$ and $Ni_{0,75}Co_{2,25}O_4$, presented in Figures 4.3a and 4.3c, display small peaks around 515 cm^{-1}, which were indistinct in $NiCo_2O_4$ in 4.3b. This peak relates to the vibrational mode of F_{2g-2}. The vibrational mode for F_{2g-3} was only detected in the spectra for $NiCo_2O_4$ and $Ni_{0,75}Co_{2,25}O_4$, around 615 cm^{-1}. Figure 4.3a displays a slight increase around this value, but the observation might be caused by a spike in intensity during analysis, rather than a peak. An interesting feature of the respective XRD-spectra in Figure 4.1 is the peaks identified at 2θ =38°and 56°, which both seem to loose intensity as the amount of nickel in the catalyst increases. There might be a correlation between the decreased intensities at these angles, and the loss of Raman shift at certain frequencies.

The only spectrum displaying peaks for all Raman active vibration modes for a spinel structure is $Ni_{0,75}Co_{2,25}O_4$. Further, this spectrum seems to exhibit sharper and more distinct peaks than the peaks displayed in Figures 4.3a and 4.3b, a relation that can be related to the respective XRD-spectra presented in Figure 4.1. In this figure, $Ni_{0,75}Co_{2,25}O_4$ comprise peaks of a more distinct nature than the complementary spectra for $NiCo_2O_4$ and $NiCoO_4$. By regarding the XRD- and Raman-spectra in unison, there might be an indication that addition of nickel disturb the spinel crystal lattice somewhat. Although cobalt and nickel are highly similar, they are not identical, and the increased addition of nickel might impede the formation of perfect spinel crystallites. In result, the XRD- and Raman-spectra for increased Ni-ratio in the material imply decreased distinction of characteristic spinel features, and also the formation of

smaller crystallites.

No peaks implying secondary phases were detected by the Raman spectroscopy, although the presence of potassium has been identified by XRF. There might be peaks indicating impurities or hydroxyl groups on the surface above 750 cm^{-1}, though these could not be identified due to fluorescence in the sample.

5.1.4 Effect of Calcination

$NiCo_2O_{4-350°C}$ and $NiCo_2O_{4-550°C}$ were synthesized together in a large batch, and calcined at different temperatures, 350°C, and 550°C, respectively. If accounting for the accepted deviation of 2%, XRF analyses suggests that the catalysts are comprised of the same ratio of nickel and cobalt. The XRD and BET analyses, however, indicate that $NiCo_2O_{4-550°C}$ undergo structural changes caused by the increased heat exposure during calcination treatment at 550°C.

The spectrum for $NiCo_2O_{4-550°C}$, presented in Figure 4.2, exhibit two peaks that are undetected in the complementary spectrum for $NiCo_2O_{4-350°C}$. These peaks were identified by the applied software as NiO. In addition all peaks for $NiCo_2O_{4-550°C}$ display a sharper and more narrow nature, which indicates that $NiCo_2O_{4-550°C}$ comprise larger crystallites than $NiCo_2O_{4-350°C}$. The TOPAS software identified the crystallite sizes for the $NiCo_2O_4$-phase in $NiCo_2O_{4-350°C}$ and $NiCo_2O_{4-550°C}$ to 6,82 and 14,34 nm, respectively. Further, the BET surface area of $NiCo_2O_{4-350°C}$ and $NiCo_2O_{4-350°C}$ presented in Table 4.1 confirm that the calcination at 550°C resulted in a significant decrease in specific surface area for $NiCo_2O_{4-550°C}$, compared to surface area of $NiCo_2O_{4-350°C}$. The formation of larger crystallites during the temperature interval between 350°C and 550°C, seems to alter both surface area and pore volume.

As the two catalysts were synthesized together in a large batch, it is logical to assume that they comprised equal features prior to the calcination treatment. It can thus be argued that the catalyst undergoes structural changes that includes sintering into larger crystallites within the temperature interval between 350°C and 550°C. The identified NiO-phase also indicates that nickel is released from the spinel structure and forms crystalline NiO-phase. This, however, results in an excess of cobalt ions in the spinel structure, seeing that the XRF-measurements establish that the overall stoichiometry remains unchanged. It is possible that some trivalent cobalt ions originally occupying octahedral sites transforms to divalent cations and occupy vacancies in tetrahedral sites, formed by the divalent nickel ions that form crystalline nickel oxide. However, as formation of NiO includes loss of oxygen from the spinel structure, the resulting coordination of the $NiCo_2O_4$ spinel structure can be hard to determine. In addition to NiO, the $NiCo_2O_4$-phase remains the preferred suggested phase for the spectra, although the presence of Co_3O_4 is possible, as explained above.

5.1.5 Palladium Deposition

The XRF analysis confirmed the presence of palladium on 0,5wt%Pd/$NiCo_2O_4$. However, the measured amount of palladium was higher than the nominal value, with a deviation of +58%. This could be a result of error during synthesis, for example that the amount of support was smaller than the basis of calculation. The amount of palladium precursor was 26 mg, and small weight errors upon measurement of the palladium precursor could cause large differences in the resulting load. Additionally, the impregnation of the palladium might not have been completely homogeneous, resulting in fractions of the catalyst comprising more or less Pd than average. The sample used for the analysis might thus have retained more Pd than the average load on the catalyst.

No palladium phases were detected in the XRD-spectrum of 0,5wt%Pd/$NiCo_2O_4$, which is presented in Figure 4.2. The identification of palladium on the catalyst by XRF implies that palladium is distributed on the catalyst in a state that is undetectable for XRD, either as small crystalline particles below the 2 nm limit of detection or as an amorphous phase. Further, the addition of 0,5wt% palladium onto $NiCo_2O_4$ (calcined at 350°C), does not seem to alter the XRD-spectrum distinctly, if comparing the spectrum of 0,5wt%Pd/$NiCo_2O_4$ to that of $NiCo_2O_{4-350°C}$ in the same figure. According to the BET-investigation, the support might undergo a slight loss of surface area upon deposition of 0,5wt% palladium. This is contradictory to the investigation of the crystallite size by the Scherrer equation, that provide a smaller crystallite size for 0,5wt%Pd/$NiCo_2O_4$ than its respective support. It should however be noted that the respective sizes were 5,8 and 6,3 nm, and the software might not provide high accuracy on such small sizes. In addition, the loss of surface area did not surpass the estimated deviation of ±4% considerably (8% deviation).

It was desired to investigate the dispersion of palladium on the catalyst further. On inert supports, the dispersion of noble metal catalysts can be investigated by chemisorption. However, for metal oxides the active site on the catalyst is unknown. The complexity of palladium deposited on such a surface would complicate the chemisorption method, as it would be unclear how the probe molecule (for instance CO) would interact with the surface. It was thus found to be preferable to determine the dispersion by investigating 0,5wt%Pd/$NiCo_2O_4$ with TEM. The TEM imaging contributed to the information regarding the deposition of palladium on 0,5wt%Pd/$NiCo_2O_4$. Figure 4.5 indicates the position of an identified Pd-particle, with increasing resolution. Figures 4.5a, c and e presents the images obtained by the backscattered electrons detected by STEM, and b, d and f are the complementary images obtained by the transmitted electrons detected by TEM. The image of palladium deposited on 0,5wt%Pd/$NiCo_2O_4$ reveal relatively modest contrast between Pd and $NiCo_2O_4$. This can be a typical feature for a particle with well-dispersed metal on a metal oxide support, [30]. The identified palladium

particles were thus subjected to elemental analysis to confirm the presence of palladium. The respective EDXS-plots presented in Figure 4.6a confirm that the particle pictured in Figure 4.5 is comprised of palladium, due to the locally increased Pd-signal. The EDXS-analysis made next to the particle, detected no Pd-elements. This implies that the Pd-deposition was performed in a way that produced small Pd particles with rather distinct boundaries between particle and support.

The Pd-particle pictured in Figure 4.5e and f, were found to have a crystalline structure with a cross section of approximately 2 nm. Further Pd-particles with equal sizes were discovered on other examined $NiCo_2O_4$ crystallites, for example the one presented in Figure 4.7. This figure indicates that the deposited palladium particle does not disturb the lattice structure of the support notably. These features were in compliance with the results, or rather the lack of results, from the XRD-spectra over 0,5wt%Pd/$NiCo_2O_4$. As no Pd-phase were detected by XRD-analysis it was likely to assume that the palladium was deposited as crystallites smaller than the detection limit for XRD, and the TEM-imaging confirms this assumption. As mentioned, by comparing the XRD-spectrum for 0,5wt%Pd/$NiCo_2O_4$ with that of $NiCo_2O_{4-350°C}$, the deposition of palladium does not seem to have induced a structural change of the support.

Only one impregnation of palladium onto $NiCo_2O_4$ was performed. The catalyst should be reproduced to validate the reported activity of the catalyst. The catalyst could possibly be optimized further by investigating for example the drying regime. However, based on the characterization results from XRD, XRF and TEM the palladium can be concluded to be well dispersed on the $NiCo_2O_4$-support. It is a promising feature for the catalyst that dispersion of the observed level was obtained at the first synthesis. The high level of dispersion could be caused by hydroxyl groups on the $NiCo_2O_4$ surface, functioning as anchor points for the palladium precursor. According to Su et al (2015 [24]), $NiCo_2O_4$ may comprise surface hydroxyl groups, which could explain the high level of dispersion obtained for 0,5wt%Pd/$NiCo_2O_4$.

5.2 Catalyst activity

The catalytic activity measurements indicate that mixed oxides of nickel and cobalt, primarily in spinel structure, have catalytic properties for low temperature methane oxidation.

In the following sections the effect of different conditions on the catalytic activity will be discussed in detail. However, certain limitations can be accounted for in all the following sections. They can be summarized as:

- T_{10}-T_{90} were found using a polynomial fitting. This polynomial was fitted to 8-10 points for the different runs, and the curve between the points may thus not describe the con-

version path perfectly.

- It was found an error in carbon balance for all runs, which increased for decreasing methane concentration in the feed.
- The reaction rate and the apparent activation energy were calculated with the assumption of a kinetic model that was of first order in methane and zero order in oxygen.

The magnitude of the limitations generated from the assumptions summarized above will be discussed to further extent in the fitting sections.

Further, the temperature profiles over the catalytic beds have not been investigated. The catalyst was diluted for the purpose of heat dissipation over the catalytic bed. It was not expected that a temperature gradient would influence the activity of the results considerably, as also diluted concentrations of reactants were investigated. However, it was noted that the heat evolution from the different reactions with equal feed concentration and reactor temperature set point, seemed to vary slightly between the different catalysts, as presented in Table 4.3. It is logical to assume that the reactions displaying equal feed concentrations will generate the same reaction heat at full conversion of methane. The difference in maximum reactor temperature might thus originate from the catalytic materials being distributed differently in the reactor during their respective reactions. The thermocouple measured the local temperature at the reactor inlet. The amount of catalytic material in the perimeter of the thermocouple will thus influence the measured temperature, due to generation of reaction heat at the active sites on the catalyst.

Finally, all the apparent activation energies found for the different runs display quite high values. It is thus assumed, based on the theory presented in Section 2.6.2, that the respective reaction rates are not considerably altered by mass transfer limitations [21].

5.2.1 Effect of Oxide Composition and Calcination

Oxide Composition

As can be seen in Figure 4.12 and Table 4.5, the Ni/Co-ratio seems to have limited dependency on catalytic activity. The catalysts were studied for activity with two reactant conditions, and they apparently display similar features for both feed compositions. All catalytic materials systematically reached full conversion at lower temperatures for 0,5% compared to 2% CH_4 in the reactant feed, with approximately 20°C difference. When regarding the 2% feed, it seemed that reference catalyst, $NiCo_2O_4$, displayed slightly lower catalytic activity, reaching full conversion temperature T_{90} at 10°C higher than $NiCoO_4$ and $Ni_{0,75}Co_{2,25}O_4$. However, this

feature was not continued for the 0,5% feed, where $Ni_{0,75}Co_{2,25}O_4$ displayed lowest activity, reaching T_{90} at 10°C higher than the other two. The lack of systematic trend in activity for the three catalyst compositions might imply that is does not exist. Lim et al. (2015 [19]) report that cobalt nickel spinel with 1:1 ratio display higher activity than $NiCo_2O_4$ and $Ni_{0,75}Co_{2,25}O_4$, however, in the present study this catalyst does not stand out.

The characterization of the three materials implies that they display similar features for both XRD- and Raman-analysis. The active sites on metal oxide catalysts are assumed to be dependent on the coordination and interaction between the vacancies and neighboring atoms on the surface [21]. The XRD- and Raman-analyses indicate that lattice parameters and vibration modes in lattice bonds are similar. This could explain why the catalysts also exhibit similar activity for methane oxidation. Pu et al (2017 [18]) reported that the activity of Co_3O_4 for methane oxidation is dependent on the abundance of Co^{2+} cations in tetrahedral sites. In the present study the tetrahedral sites are occupied by Ni^{2+}, however, the dependency of activity on abundance of tetrahedral sites might be applicable. The characterization indicated that the three catalysts displayed highly similar features, maintaining the features characteristic for a spinel oxide. However, tuning of the ratio of Ni and Co might not change the overall amount of tetrahedral and octahedral sites within the lattice, which could explain the similar activities displayed by the catalysts.

The reaction rates presented in Table 4.5 decrease with decreasing amounts of methane in feed. This is in accordance with the kinetics for a first order reaction. However, the reaction rate is not completely proportional to the feed concentration of methane.

The reaction rates for the 0,5% reactions are approximately 1/3 of the reaction rates in the 2% reaction for all three investigated catalysts. It is rare that the empirical reaction rate fits mathematical models completely, although as all catalysts seem to be proportional in the same trend it might be an indication of a systematic error based on a mismatch between the assumed and the realistic model. All three catalysts display slightly different apparent activation energies for the 2% and 0,5%. However, the deviance is not prominent, and might be within the range that can be expected from the discussed assumptions. However, when regarding the activation energies, it should be kept in mind that they are based on assumptions that might not be valid for the reaction mechanisms of methane oxidation over the studied mixed oxides. This will be discussed in further detail under 5.2.2.

In general, the results obtained from investigating the effect of Ni/Co-ratio on catalytic activity did not imply dependency between the two, as opposed to the results reported by Lim et al. [19].

Calcination Temperature

Figure 4.13 indicates the effect of calcination temperature on catalytic activity for reaction over fresh catalysts. For $NiCo_2O_{4-350°C}$ the catalyst initially showed a superior activity, which can be reviewed in Figure 4.13a. This preliminary activity was deprived during the reactor cooling in the same reaction cycle, and did not recover for the subsequent cycles. $NiCo_2O_{4-550°C}$, did not display this feature, with close to equal conversion profiles for the heating and cooling sequence. The difference in the profiles, in addition to the characterization results already discussed, implies that the catalysts undergo structural changes at high temperatures. These changes seem to be independent of the reaction occurring on the surface. The catalysts were calcined in air, and if the change in activity witnessed for fresh $NiCo_2O_{4-350°C}$ was caused by interactions made during reaction on the surface, the change would likely be evident in the conversion profile for $NiCo_2O_{4-550°C}$ as well. Since the latter maintained its initial activity, the loss of activity seen in $NiCo_2O_{4-350°C}$ is likely to be thermally caused. The activity for $NiCo_2O_{4-350°C}$ stabilized at a level close to that of $NiCo_2O_{4-550°C}$, as can be reviewed in Figure 4.14. It is thus reasonable to assume that the structural changes indicated by the activity loss in Figure 4.13a will resemble the structural changes that $NiCo_2O_{4-550°C}$ underwent during the calcination treatment.

The characterization of the two catalysts indicated two changes upon calcination at 550°C, rather than at 350°C. The loss of initial activity for catalyst calcined at the latter, can on this basis be explained by two potential effects. First, the $NiCo_2O_{4-550°C}$ comprised larger crystallites, more than twice the size of those in $NiCo_2O_{4-350°C}$. This implied loss of specific surface area, which was measured as considerably lower for $NiCo_2O_{4-550°C}$. Second, the phase of NiO was detected in the XRD-spectrum for $NiCo_2O_{4-550°C}$ and not in the spectrum for $NiCo_2O_{4-350°C}$. NiO is reported to exhibit lower activity for methane combustion compared to the activity of $NiCo_2O_4$, [19] and [14]. If the formation of NiO caused a reduction of the amount of catalytic material from the active spinel structure, this might have induced loss of active material. However, it should be noted that the previously discussed possibilities still apply. The spinel structure may have been maintained by the transfer of cobalt within the lattice structure, and thus have maintained activity. Co_3O_4 is reported to have considerable activity for methane combustion [18]. Further, the amount of nickel attributed to the NiO-peaks in the XRD-spectrum of $NiCo_2O_{4-550°C}$ has not been investigated. The measured loss of activity might thus not be balanced by the amount of crystalline NiO formed.

The conversion profiles presented in Figure 4.14 and their respective activities presented in Table 4.6, presents the activity for both catalysts after several reaction cycles. The presented runs display the similar features discussed above, in regards to feed concentration of CH_4, activation energy and reaction rate. Investigation of Figure 4.14 and the respective activities presented in Table 4.4, show that T_{10}-T_{90} for $NiCo_2O_{4-350°C}$ systematically lie approximately

10°C lower than the respective values for $NiCo_2O_{4-550°C}$ for both reactant feeds investigated. Two explanations could describe this trend. $NiCo_2O_{4-550°C}$ was calcined at 550°C for 24 h. Even though several reaction cycles were performed over $NiCo_2O_{4-350°C}$, it was not exposed to such high temperatures for an equal amount of time as $NiCo_2O_{4-550°C}$ was during calcination. It might thus be possible that the magnitude of the structural changes applied to $NiCo_2O_{4-550°C}$ not was matched by those applied to $NiCo_2O_{4-350°C}$. $NiCo_2O_{4-350°C}$ would thus maintain parts of its superior activity over $NiCo_2O_{4-550°C}$. The other explanation relates to the maximum temperature measured in the reactor, presented in Table 4.3. Upon complete conversion of 2% methane, the maximum temperature in the reactor was measured to 12°C higher for $NiCo_2O_{4-550°C}$ than for $NiCo_2O_{4-350°C}$, despite that both reactions have the same temperature set point (550°C) and are converting the same amount of methane. It is thus possible that differences in catalyst distribution within the catalyst bed entailed different temperature being measured at the reactor inlet.

Tao et al. (2015, [14]) report that the first and second reaction cycle of methane oxidation over $NiCo_2O_4$ were equal. Further it is reported that full conversion of a feed with 5% CH_4 over 500 mg of $NiCo_2O_4$ was reached at 350°C, and that this activity was maintained after heating the catalyst to 550°C. In the present work, higher temperatures were required to obtain full conversion over the same amount of catalyst, despite the CH_4 concentration being lower. However, to advocate the arguments discussed above, conversion profiles similar to the one presented in Figure 4.13a was observed over fresh catalyst for all catalysts calcined at 350°C, except the reference catalyst. The measurements for the first reaction cycle over the reference catalyst was lost, due to technical issues during the experimental start up. It is however, based on the observations made for the other catalysts, assumed that this catalyst would display an initial superior activity as illustrated in Figure 4.13a. The loss of initial activity was smaller for 0,5wt%Pd/$NiCo_2O_4$, which may be related to the maximum reactor set point being 50°C lower than for the other reactions. However, the first cycle over 0,5wt%Pd/$NiCo_2O_4$ is not completely comparable, as the deposition of palladium might change the material properties causing the system to be more complex.

5.2.2 Effect of Methane Concentration

The effect of feed concentration of CH_4 over the reference catalyst, $NiCo_2O_4$, was investigated for three feeds, 2%, 0,5% and 0,1% CH_4. The previously mentioned systematic decrease in T_{90} was continued for the reaction with 0,1% methane in the feed. This reaction reached T_{90} at a temperature 20°C lower than for 0,5% as shown in Table 4.7. However, the conversion profile in Figure 4.15, displayed a sharper tendency than those observed for the 0,5% and 2% reactions. According to the activities presented in Table 4.4, T_{10}-T_{50} for 0,1% are higher

than for 0,5%. However, beyond the half conversion temperature, the 0,1% reaction requires less heat to reach full conversion. It seems that the upper tail of all conversion profiles in Figure 4.15 is extended by increased CH_4 feed concentration, with the profiles for 0,5% and 2% reactions having more distinct S-shapes. The carbon error in the system is increased for decreasing initial concentration of CH_4. At 0,1%, the methane concentration is approaching the detection limit of the μGC-apparatus. The apparatus might fail to detect the conversion of methane at lower temperatures, and the obtained conversion profile are thereby presented with a slower initiation. However, the carbon error profile indicates that the carbon error gets higher at increasing conversion of methane.

The significance of the carbon error on the calculated conversion of methane might be dismissed by regarding the source of the carbon error. By investigating the GC-logs obtained from the different runs, it was concluded that methane and carbon consistently were the only carbon species present in the system. However, it was noted that the measured amounts for CO_2 never reached the same concentration level as the initial methane concentration. The μGC was calibrated for two levels of methane, 0,5% and 1% CH_4, and the μGC logs generally displayed the desired feed concentrations which decreased steadily until complete conversion was noted. CO_2 was first detected in the system a short while after conversion CH_4 seemed to have been initiated, and the detection of CO_2 after full conversion of CH_4 did not match the feed concentration of methane. The μGC was not calibrated for dilute concentrations of CO_2, and the magnitude of the carbon error might originate mainly from the detection of CO_2. The calculation of the methane conversion was performed on the basis of CH_4 and N_2, and it can thus be argued that the magnitude of the carbon error will have limited significance for the calculated conversion. With this basis it is assumed that in the present work the shift in conversion profiles is not due to the carbon error in the system, but rather an accurate presentation of how methane conversion at decreased reactant concentration occurs.

It was found by investigating the temperature logs for Runs 1-3 that the heat evolution in the system was higher for higher methane concentration. This is in accordance with the thermodynamics of the system, the more methane that is being converted, the more reaction heat is generated to the system. All three reactions had maximum oven set point at 550°C, and the maximum temperature measured for Runs 1-3 were 562°C, 535°C and 522°C, respectively.

The calculated catalytic activities for the three investigated runs over $NiCo_2O_3$ are presented in Table 4.7. As previously mentioned, the activation of methane should be independent of the feed concentration of methane. The results presented in Table 4.7, however, seem to indicate that the activation energy decrease with decreasing methane concentration in feed. The origin of this deviation could be explained by the assumptions that are the bases of the calculation. The assumption of a reaction mechanism that is first order in methane might result in a systematic decrease of E_A at decreasing methane concentration. The deviation could also be

caused by a systematic error in the measurement procedure. The trend of the reaction rates seems to be coherent with the kinetic model, however, the values should be regarded with care, due to previously mentioned arguments.

5.2.3 Effect of Palladium

The effect of palladium deposition was investigated and compared to the activity of the reference catalyst for two reactant feeds, 2% and 0,1% CH_4. As shown in Figure 4.16, the addition of 0,5wt% Pd to the surface of $NiCo_2O_4$ increased the catalytic activity remarkably. For the 2% reaction T_{90} was achieved at 40°C lower than for the reference catalyst, and for the 0,1% reaction T_{90} was achieved at 50°C lower. The increase in catalytic activity in 0,5wt%Pd/$NiCo_2O_4$ might be caused by a synergic effect between Pd and the support. Alternatively, it may be caused by the methane conversion being completed singularily by the highly active palladium particles deposited on the surface. Tables 4.4 and 4.7 presents the activities for the runs presented in Figure 4.16. In addition, the activities for two catalysts comprised of 0,2wt% and 2wt% palladium deposited on Al_2O_3 are presented. These values were calculated from the measurements reported by Sandvik (2016 [4]). Sandvik's results were included to compare the catalytic activity of the reference catalyst to the conventional noble metal catalyst, and to identify the possibility of a synergic effect between Pd and $NiCo_2O_4$ in 0,5wt%Pd/$NiCo_2O_4$.

The log entries from the temperature- and the μGC-log for the two investigated catalysts were reported in Sandvik's thesis, and the measurements were processed by the same method used for the results in the present work. The reported measurements were thus applied to the Matlab-script to obtain measures on catalytic activity. It should thus be noted that systematic errors that could occur during the data processing also would be relevant for the reproduced activities of the Pd/Al_2O_3-catalysts reported in Tables 4.4 and 4.7.

Figure 4.16 indicates that 0,5wt%Pd/$NiCo_2O_4$ follows the same trend as the reference catalyst in regards to CH_4 concentration in feed, including a sharpening of the conversion profile for 0,1% CH_4. However, the upper tail of the curve suggests a slight flattening of conversion at higher temperature, which relates to the conversion profile that can be seen in both 2% CH_4 reactions. Further, the deposition of palladium seem to have a larger effect for the reaction with 0,1% CH_4. By reviewing the activities presented in Table 4.4, it seems that relative to the full line (2%), the dashed line (0,1%) is shifted more towards lower temperatures for 0,5wt%Pd/$NiCo_2O_4$ compared to $NiCo_2O_4$. This could be an indication that the two catalysts follow different kinetic models, to some extent. The dependency of methane concentration of a reaction with order below zero, would not be equally high compared to a reaction with first order in methane. The possible increased dependency of methane concentration over 0,5wt%Pd/$NiCo_2O_4$, might be an indication that methane oxidation over this catalyst follow

a reaction order that is higher in methane, than methane oxidation over $NiCo_2O_4$. This is not in complete alliance with the calculated reaction rates for the two catalysts, which indicate that the reaction over $NiCo_2O_4$ are closer to proportionality between the reactions with 0,1% and 2% CH_4 in the feed. However, the calculated values can be misleading for the reactions comprising 0,1%, because the rate was determined based on the conversion at 325°C. For 0,5wt%Pd/$NiCo_2O_4$ both reactant feeds have surpassed the limit of 20% conversion, meaning that the activity is beyond the valid range of Equation 2.7. Furthermore, this is the case for the 0,1% feed over $NiCo_2O_4$ as well. The reaction rates presented in Table 4.7 might thus have higher inaccuracy than the reported reaction rates for the supplementary reactions.

Both 0,5wt%Pd/$NiCo_2O_4$ and $NiCo_2O_4$ display higher activity than the catalyst with 0,2wt%Pd supported on alumina. 0,5wt%Pd/$NiCo_2O_4$ reach T_{90} at 120°C lower than 0,2wt%Pd/Al_2O_3, and $NiCo_2O_4$ reach it at 75°C lower. By investigating T_{10}-T_{90} it seems that the low activity of the alumina supported catalyst is mainly due to the high temperature necessary to reach the ignition temperature. The temperature difference from T_{10} and T_{90} is about the same for 0,2wt%Pd/Al_2O_3 and $NiCo_2O_4$ (ΔT=148 and 152, respectively). 0,5wt%Pd/$NiCo_2O_4$ seem to display slightly higher rate of conversion after ignition, as the respective ΔT between T_{10} and T_{90} is 127°C. This might be explained by the activation energy of the system, that according to Table 4.7 is higher for 0,2wt%Pd/Al_2O_3. The increased E_A indicate that the reaction over 0,2wt%Pd/Al_2O_3 requires higher temperature in the system to initiate reaction. An interesting topic for further study would be to investigate how high the alumina loading must be, to surpass the activity of $NiCo_2O_4$.

2wt%Pd/Al_2O_3 displays higher activity than 0,5wt%Pd/$NiCo_2O_4$ and $NiCo_2O_4$, which respectively reach T_{90} at 20°C and 60°C higher. Interestingly, 0,5wt%Pd/$NiCo_2O_4$ seems to "keep up" with the initial activity of 2wt%Pd/Al_2O_3, displaying similar temperatures until T_{50} in Table 4.4. Beyond this point, palladium supported on alumina showed superior activity. However, the two catalysts have different loading of palladium, and the activity can thus not be directly compared. Alumina is a widely used support, due to the material's high surface area. Sandvik report that 2wt%Pd/Al_2O_3 have a BET surface area of 130 m^2/g, with Pd-particles of about 5,5 nm. This implies that Pd is relatively well dispersed on the surface. However, the TEM images indicate that the palladium particles on 0,5wt%Pd/$NiCo_2O_4$ are about 2 nm. The Pd might thus be better dispersed on 0,5wt%Pd/$NiCo_2O_4$, which can imply higher efficiency of the Pd particles despite 0,5wt%Pd/$NiCo_2O_4$ having a smaller loading of Pd and less than half the surface area of 2wt%Pd/Al_2O_3.

E_A for 0,5wt%Pd/$NiCo_2O_4$ seemed to be independent of the concentration of CH_4 in the feed. This might indicate that methane oxidation over 0,5wt%Pd/$NiCo_2O_4$ displays features that are closer to the assumed kinetic model of the system. Methane oxidation over 2wt%Pd/Al_2O_3 is a widely studied reaction sequence, and the reaction has been reported to be of first order in

methane, and of zero order in oxygen under lean conditions [1]. However, the reaction order is reported to be dependent of the oxygen concentration if the reaction conditions are varied between oxidizing and reducing conditions (lean and rich) [1]. Regardlessly, when calculating the activation energy and reaction rate in the present work, it was assumed that the reaction was of first order in methane and zero order in oxygen. The activation energy may indicate that 0,5wt%Pd/$NiCo_2O_4$ follows the assumed model, as it displays independence of methane concentration. Both 0,5wt%Pd/$NiCo_2O_4$ and the reference catalyst seem to have lower activation energy than the two alumina supported palladium catalysts. However, the activation energy values obtained might be misleading, when accounting for previously discussed arguments.

The reaction rates presented in Table 4.7 indicate that the 2wt%Pd/Al_2O_3 exhibit a reaction rate per gram catalyst twice as high as the rate for 0,5wt%Pd/$NiCo_2O_4$. The reaction rate per gram palladium for 0,5wt%Pd/$NiCo_2O_4$ was found to be higher than the two investigated catalysts with palladium supported on alumina. This may indicate a synergic effect between the palladium and the support oxide, as the reaction rate over the palladium in 0,5wt%Pd/$NiCo_2O_4$ is higher than for both catalysts were palladium is the only active site. The reaction rate over Pd in 0,5wt%Pd/$NiCo_2O_4$ might be enhanced by reaction that occurs on the metal oxide sites of the support. The possibility of a synergic effect between Pd and $NiCo_2O_4$ is an interesting topic for further investigation, for motivations that will be discussed in Section 5.2.4. It should be noted that the reaction rate per gram palladium is calculated on the basis on the nominal amount of palladium. According to the XRF-analysis, there might be more Pd in the system than 0,5wt%. According to Sandvik's results, the deviation from nominal loadings of the alumina supported catalysts are approximately +40 and -15% for 0,2wt%Pd/Al_2O_3 and 2wt%Pd/Al_2O_3 respectively. The deviations from nominal loading might decrease the accuracy of the calculations in the values presented in Table 4.7.

5.2.4 Effect of Water

It was found that H_2O deactivated the 0,5wt%Pd/$NiCo_2O_4$ and $NiCo_2O_4$ catalysts reversibly. 0,5wt%Pd/$NiCo_2O_4$ maintains the superior activity over the reference catalyst in the presence of water, as can be seen in Figure 4.17 and Table 4.8. The reference catalyst reached T_{90} at 479°C, which was 47°C higher than for 0,5wt%Pd/$NiCo_2O_4$, which reached T_{90} at 432°C. The difference between T_{90} for the two catalysts were at the same level for the reaction with and without water present in the feed (52 °C for the latter). This indicates that the inhibiting effect of water occurs by a similar process for both catalysts.

The deactivation of the catalyst is reversible, discarding the possibility of permanent structural changes of the catalyst. Xu et al. (2015 [38]) report that water molecules can deactivate most non-noble metal catalysts reversibly, by adsorbing on the active sites on the surface. Similar

effects are also reported for Pd/Al_2O_3, and Chen et al. (2015 [13]) report of competitive adsorption between CH_4 and H_2O on active sites in the presence of water. This competition can transform the active PdO site to inactive $Pd(OH)_2$, leading to slow irreversible deactivation of the Pd-sites. In the present work the immediate effect of water was investigated, though it would be interesting to investigate if 0,5wt%$Pd/NiCo_2O_4$ would maintain superior activity over the reference catalyst over time. No data indicating increased loss of activity in the presence of water over $NiCo_2O_4$ was discovered during the literature search conducted for this thesis. Adsorption of water molecules on the catalyst surface seems to be a likely explanation for the loss of activity over the two catalysts, as the activity was restored upon the following reaction runs without water in the reactant feed. Further investigations should elucidate if the irreversible deactivation reported for Pd/Al_2O_3 also is valid over 0,5wt%$Pd/NiCo_2O_4$, or if a possible synergic effect between Pd and $NiCo_2O_4$ deprive the formation of inactive Pd-sites.

The apparent activation energies presented in Table 4.7 indicate that both catalysts display higher E_A than was found for the reactions with dry feed. It is possible that the increase in activation energy is a consequence of the adsorption of water on the surface. In this case, the E_A would enclose the activation of methane and the energy of desorption of water from the surface, or it could entirely rely on the latter. The rate of reaction is also decreased in the presence of water. It is possible that methane oxidation follows a kinetic model in the presence of water that deviates more from the assumed model than the previously investigated reactions. Giezen et al. [39] report that catalytic methane oxidation over supported palladium in the presence of water follows a kinetic model that is of order 1,0 in CH_4, 0,2 in O_2 and -0,9 in H_2O. Although the kinetic model for supported Pd might not be applicable for the present catalysts, it should not be discarded. In addition, it should be noted that although the kinetic model might not follow the presumed assumptions, there is definitely a linear relationship in the Arrhenius plots found for the $0{,}1\%_{H_2O}$ reactions over 0,5wt%$Pd/NiCo_2O_4$ and $NiCo_2O_4$, which are presented in Figures D.6c and D.1d in Appendix D, respectively.

The water tolerance over $NiCo_2O_4$ and $Pd/NiCo_2O_4$ is an interesting field for further study. Pu et al. (2017 [18]) report that the aging time during synthesis of coprecipitated Co_3O_4 can improve the water tolerance of the catalyst for methane oxidation in a wet atmosphere. It would be interesting to investigate if this study is applicable for mixed oxides of nickel and cobalt.

Based on the results obtained in this thesis, $NiCo_2O_4$ and $Pd/NiCo_2O_4$ exhibit sufficient activity for NGV exhaust gas after treatment, by reaching 90% methane conversion at 479°C and 432°C, respectively. The temperature of NGV exhaust gas generally holds around 550°C, and 500-1500 ppm methane concentration. It should be further investigated how high the methane feed concentration can become before higher temperatures are necessary to reach full conversion. As mentioned in the introduction, the methane concentration of exhaust gas can vary

depending on conditions such as the engine fire power.

Chapter 6

Conclusion

In this master thesis the catalytic activity of mixed transition metal oxides comprised of nickel and cobalt have been investigated for complete catalytic oxidation of methane at low temperatures. The motivation for the project was to contribute research of new material for complete catalytic oxidation of methane, to be used for exhaust clean up in marine natural gas vehicles. This was to ensure greenhouse gas abatement from the marine industry.

The catalytic activity was investigated for dependency on stoichiometric ratio between nickel and cobalt, calcination temperature during preparation and activity upon deposition of a small fraction of palladium deposited on the surface. Further, the dependency of methane concentration in reactant feed and activity in presence of water were investigated, to conclude on the catalytic activity in realistic exhaust gas conditions. All catalysts were synthesized by the coprecipitation method, and the catalyst investigating Pd deposition was further prepared by incipient wetness impregnation. The catalysts were characterized with XRD, N_2 physisorption, XRF, Raman spectroscopy and TEM. They were further investigated in a reaction rig adapted for methane oxidation. The catalytic activities were studied at different levels of conversion, and by estimating the reaction rate and activation energy when assuming the reaction as first order in methane and zero order i oxygen.

The stoichiometric dependency was investigated over three catalysts, one stoichiometric spinel, $NiCo_2O_4$, one comprising nickel surplus with 1:1 ratio of nickel and cobalt, $NiCoO_4$ and one comprising nickel deficit, $Ni_{0,75}Co_{2.25}O_4$. The characterization of the catalysts suggested that with decreasing nickel ratio in the catalyst, the crystallite sizes increased and the surface area decreased. It was further suggested by the XRD and Raman analyses that the three catalysts comprised highly similar features, which was assumed to be caused by the similar properties of nickel and cobalt. The activity measurements indicated that there were limited dependency between the nickel cobalt ratio in the catalyst and the catalytic activity for methane oxidation. By decreasing the methane concentration in the feed, it was found that all studied catalysts systematically required lower temperatures to reach full conversion. The kinetic investigations resulted in similar activation energies for most runs, between 70 and 80 $KJ\,mol^{-1}$ which were assumed to be an appropriate value. However, with reactions comprising very low amounts of methane (0,1%) or addition of water, the activation energy was altered. The range of activation

energy values obtained from different concentrations of methane in feed for one catalyst, was possibly caused by deviation from the assumed kinetic model. For the reactions not comprising water in feed, the kinetic model was however found to be sufficient to investigate the catalytic activity, partly due to the observed proportionality between reaction rate and methane concentration.

It was found that the calcination treatment facilitated structural changes on the catalyst. The two catalysts produced for this investigation, $NiCo_2O_{4-350°C}$ and $NiCo_2O_{4-550°C}$, were calcined at 350°C and 550°C, respectively, and were found to comprise equal nickel cobalt ratio, by XRF analysis. The calcination at 550°C induced sintering of the crystallites, loss of surface area and formation of NiO-phase in the catalytic material, by XRD and BET investigation. The first cycle over $NiCo_2O_{4-350°C}$ catalyst showed no loss of activity over fresh catalyst, contradictory to $NiCo_2O_{4-350°C}$. After several reaction cycles the two catalysts displayed similar activities, suggesting that the first reaction cycle induced structural changes in $NiCo_2O_{4-350°C}$ resembling those observed after calcination in $NiCo_2O_{4-550°C}$.

The deposition of 0,5wt%Pd onto $NiCo_2O_4$ was found to enhance the catalytic activity of the catalyst remarkably, possibly due to the high dispersion obtained for the palladium particles. TEM investigation indicated that the Pd particles on $NiCo_2O_4$ were small crystallites with a cross section of approximately 2 nm. The effect of water seemed to deactivate both 0,5wt%Pd/$NiCo_2O_4$ and $NiCo_2O_4$ reversibly in a similar matter, with 0,5wt%Pd/$NiCo_2O_4$ maintaining superior activity of the two. Further, addition of water to the feed was likely to alter the kinetic model of the system. By regarding the necessary temperature to reach 90% conversion for 0,5wt%Pd/$NiCo_2O_4$ and $NiCo_2O_4$ to that of a conventional palladium catalyst supported on alumina it was found that they: i) displayed higher activity than 0,2wt%Pd/Al_2O_3 and ii) displayed lower activity of 2wt%Pd/Al_2O_3, in a reactant feed comprising 2% CH_4, 10% O_2 and balance N_2. Investigations of the reaction kinetics indicated that a possible synergic effect between Pd and $NiCo_2O_4$ enhanced the activity of 0,5wt%Pd/$NiCo_2O_4$, and that the catalyst possibly followed the assumed kinetic model to greater extent than undeposited oxide.

In general, all catalysts displayed high catalytic activity for methane oxidation. In a reactant feed of 0,1% CH_4, 15% H_2O, 10% O_2 and balance N_2, corresponding to realistic exhaust gas conditions, $NiCo_2O_4$ and 0,5wt%Pd/$NiCo_2O_4$ exhibit sufficient activity for application to NGV exhaust gas after treatment, by reaching 90% methane conversion at 479°C and 432°C, respectively. This is below the limit of minimum temperature of NGV exhaust gas, and the catalysts can thus be fitting materials for this application. However, the catalysts should be subjected to further research to investigate how high the methane feed concentration can become before higher temperatures are necessary to reach full conversion. As mentioned in the introduction, the methane concentration of exhaust gas can vary depending on conditions such as the engine fire power.

Chapter 7

Further Work

$NiCo_2O_4$ should be investigated further for the application of catalytic after treatment of exhaust gas from marine NG vessels. The present research indicated that the stoichiometric ratio of nickel and cobalt did not change the catalytic activity considerably, and thus could limited conclusions be made on the dependency. This was contradictory to previous research made by Lim et al (2015 [19]), and further investigation should thus be made to these materials, to establish the relationship between nickel and cobalt ratio and the catalytic activity. Further, effects facilitating enhanced activity in the presence water should be investigated further, such as aging time reported by Pu et al (2017 [18]) for Co_3O_4 and the addition of SnO that was reported to improve water tolerance of Co_3O_4 for CO oxidation by Xu et al (2015 [38]).

Based on the results obtained in this thesis, $NiCo_2O_4$ and $Pd/NiCo_2O_4$ exhibit sufficient activity for NGV exhaust gas after treatment, by reaching 90% methane conversion at 479°C and 432°C, respectively. However, it should be further investigated how high the methane feed concentration can become before higher temperatures are necessary to reach full conversion. As mentioned in the introduction, the methane concentration of exhaust gas can vary depending on conditions such as the engine fire power. Further, the catalytic activity for proper exhaust gas conditions should be investigated, i.e with a reactant feed comprising all compounds found in exhaust gas. It is however expected that the compound causing the most notable drawback of catalytic activity is water. The catalytic lifetime should further be investigated, to evaluate if the catalysts exhibit loss of activity over time on stream. It is reported that Pd-based catalysts are deactivated by water after time on stream. It would be of commercial interest to investigate if Pd experience the same features when supported on $NiCo_2O_4$. The possibility of such synergic effects between palladium and $NiCo_2O_4$ should additionally be investigated further. The high dispersion of palladium obtained in this work, indicate that $Pd/NiCo_2O_4$ could be a promising catalyst.

Bibliography

[1] Patrick Gélin and Michel Primet. Complete oxidation of methane at low temperature over noble metal based catalysts: a review. *Applied Catalysis B: Environmental*, 39(1):1–37, 2002.

[2] United Nations Framework Convention on Climate Change. UNFCCC - Global Warming Potentials, 1995. `http://unfccc.int/ghg{_}data/items/3825.php` [Accessed: 2017-05-29].

[3] Joo H. Lee and David L. Trimm. Catalytic combustion of methane. *Fuel Processing Technology*, 42(2):339–359, 1995.

[4] Helene Mørkkåsa Sandvik. *Catalysis for Control of Methane Slip in Marine Machinery Using a Palladium based Catalyst*. PhD thesis, Norwegian University of Science and Technology, 2016.

[5] Hanna Marie Storvik. *Catalysis for control of methane slip in marine machinery*. Master's thesis, Norwegian University of Science and Technology, 2016.

[6] DNV GL Maritime. Reduksjon Av Klimagassutslipp Fra Skipsfarten. Technical report, Oslo, 2016.

[7] Mathias Klingenberg. Kaptein om bord på verdensnyheten: - Jeg kjenner ingen forskjell, 2016. `http://www.tu.no/artikler/kapteinen-om-bord-pa-verdensnyheten-jeg-kjenner-ingen-forskjell/363685` [Accessed: 2017-03-10].

[8] Hilde Venvik. Lecture in TKP4515 Energy Environmental Catalysis. Technical report, Norwegian University of Science and Technology, 2016.

[9] DNV GL and ENOVA SF. Teknologier og tiltak for energieffektivisering av skip. Technical report, 2016.

[10] United Nations Economic Commision for Europe. Gothenburg Protocol. `http://www.unece.org/environmental-policy/conventions/envlrtapwelcome/guidance-documents-and-other-methodological-materials/gothenburg-protocol.html` [Accessed: 2017-05-29].

[11] European Commision. Paris Agreement. https://ec.europa.eu/clima/policies/international/negotiations/paris{_}en [Accessed: 2017-05-09].

[12] Grønt Kystfartsprogram. Sjøkart for grønn kystfart. Technical report, 2016.

[13] Jinghuan Chen, Hamidreza Arandiyan, Xiang Gao, and Junhua Li. Recent Advances in Catalysts for Methane Combustion. *previously: Catalysis Surveys from Japan*, 19(3):140–171, 2015.

[14] Franklin Feng Tao, Jun-Jun Shan, Luan Nguyen, Ziyun Wang, Shiran Zhang, Li Zhang, Zili Wu, Weixin Huang, Shibi Zeng, and P Hu. Understanding complete oxidation of methane on spinel oxides at a molecular level. *Nature communications*, 6:7798, 2015.

[15] Naoto Kamiuchi and Koichi Eguchi. *Catalytic Combustion of Methane*, pages 305–327. Springer New York, New York, NY, 2012.

[16] Anthony R. West. *Basic Solid State Chemistry*. John Wiley & Sons Ltd, Chichester, 2. edition edition, 2010.

[17] Brian D Hosterman. *Raman Spectroscopic Study of Solid Solution Spinel Oxides*. PhD thesis, University of Nevada, 2011.

[18] Zhiying Pu, Huan Zhou, Yifan Zheng, Wanzhen Huang, and Xiaonian Li. Enhanced methane combustion over Co3O4 catalysts prepared by a facile precipitation method: Effect of aging time. *Applied Surface Science*, 410:14–21, 2017.

[19] Tae Hwan Lim, Sung June Cho, Hee Sung Yang, M.H Engelhard, and Do Heui Kim. Effect of Co/Ni ratios in cobalt nickel mixed oxide catalysts on methane combustion. *Applied Catalysis A: General*, 505:62–69, 2015.

[20] Martin Lok. Coprecipitation. In Krijn P. de Jong, editor, *Synthesis of Solid Catalysts*, chapter 7, pages 135–151. WILEY-VCH Verlag GmbH & Co. KGaA, Weinheim, 2009.

[21] I. Chorkendorff and J.W. Niemantsverdriet. *Concepts of Modern Catalysis and Kinetics*. WILEY-VCH Verlag GmbH & Co. KGaA, Weinheim, second edition, 2007.

[22] James Thomas Richardson. *Principles of Catalyst Development*. Plenum Press, New York, 1989.

[23] Eric Marceau, Xavier Carrier, and Michel Che. Impregnation and Drying. In Krijn P. de Jong, editor, *Synthesis of Solid Catalysts*, chapter 4, pages 59–83. WILEY-VCH Verlag GmbH & Co. KGaA, Weinheim, first edition, 2009.

[24] Yu-Zhi Su, Qi-Zhi Xu, Gao-Feng Chen, Hui Cheng, Nan Li, and Zhao-Qing Liu. One dimensionally spinel NiCo2O4 nanowire arrays: facile synthesis, water oxidation, and magnetic properties. *Electrochimica Acta*, 174:1216–1224, aug 2015.

[25] Malte Behrens and Robert Schlögl. X-Ray Diffraction and Small Angle X-Ray Scattering. In Michel Che and Jacques C. Védrine, editors, *Characterization of Solid Materials and Heterogeneous Catalysts - Volume 2*, chapter 15, pages 611–653. WILEY-VCH Verlag GmbH & Co. KGaA, Weinheim, 2012.

[26] International Union of Crystallography. Ewald Sphere. `http://reference.iucr.org/dictionary/Ewald{_}sphere` [Accessed: 2017-06-05].

[27] Eva Margui and R van Grieken. *X-Ray Fluorescence Spectrometry and Related Techniques : An Introduction*. Momentum Press, [New York, N.Y.] [222 East 46th Street, New York, NY 10017], 2013.

[28] Karl Wirth. X-Ray Fluorescence.

[29] Introduction to XRF Spectroscopy. `http://www.horiba.com/scientific/products/x-ray-fluorescence-analysis/tutorial/` [Accessed: 2017-04-12].

[30] J.W. Niemantsverdriet. *Spectroscopy in Catalysis, An Introduction*. WILEY-VCH Verlag GmbH & Co. KGaA, Weinheim, third edition, 2007.

[31] Fengtao Fan, Zhaochi Feng, and Can Li. Raman and UV-Raman Spectroscopies. In Michel Che and Jacques C. Védrine, editors, *Characterization of Solid Materials and Heterogeneous Catalysts - Volume 1*, chapter 2, pages 49–87. WILEY-VCH Verlag GmbH & Co. KGaA, Weinheim, first edition, 2012.

[32] Edgar Bright Wilson, J. C. Decius, and Pauls C. Cross. *Molecular Vibrations - The Theory of Infrared and Raman Vibrational Spectra*. McGraw-Hill Book Compony, Inc, New York, first edition, 1955.

[33] John Meurig Thomas and Caterina Ducati. Transmission Electron Microscopy. In Michel Che and Jackes C Verdrine, editors, *Characterization of Solid Materials and Heterogeneous Catalysts - Volume 2*, chapter 16, pages 655–699. WILEY-VCH Verlag GmbH & Co. KGaA, Weinheim, first edition, 2012.

[34] H. M. McNair and J. M. Miller. *Basic Gas Chromatography*. John Wiley & Sons, Inc., Hoboken, 2nd ed. edition, 2009.

[35] Scott H. Fogler. *Elements of Chemical Reaction Engineering*. Pearson Education Limited, Harlow, fourth edition, 2014.

[36] Zhiping Chen, Sheng Wang, Ya Ding, Lei Zhang, Lirong Lv, Mingzhe Wang, and Shudong Wang. Pd catalysts supported on Co3O4 with the specified morphologies in CO and CH4 oxidation. *Applied Catalysis A: General*, 532:95–104, 2017.

[37] Ejikeme Raphael Ezeigwe, Poi Sim Khiew, Chiu Wee Siong, and Michelle T T Tan. Solvothermal synthesis of NiCo2O4 nanocomposites on liquid-phase exfoliated graphene as an electrode material for electrochemical capacitors. *Journal of Alloys and Compounds*, 693:1133–1142, 2017.

[38] Xianglan Xu, Xiongfei Sun, Hong Han, Honggen Peng, Wenming Liu, Xing Peng, Xiang Wang, and Xiangjie Yang. Improving water tolerance of Co3O4 by SnO2 addition for CO oxidation. *Applied Surface Science*, 355:1254–1260, nov 2015.

[39] J C Van Giezen, F R Van Den Berg, J L Kleinen, A J Van Dillen, and J W Geus. The effect of water on the activity of supported palladium catalysts in the catalytic combustion of methane. 47, 1999.

Appendix A

Calculation of Amount of Precursor

A.1 Syntheisis by Coprecipitation

Table A.1 presents the amount of mol of the two precursor compounds that were used to produce the different catalysts.

Table A.1: Amount mol of the two precursor compounds used to produce the different mixed transition oxides.

Batch	**Catalyst**	**$Ni(NO_3)_2 \cdot 6H_2O$** [mol]	**$Co(NO_3)_2 \cdot 6H_2O$** [mol]
1[a]	$NiCo_2O_4$	0,01	0,02
2[a]	$NiCoO_4$	0,02	0,02
3	$Ni_{0,75}Co_{2,25}O_4$	0,0075	0,0225
4+5[b]	$NiCo_2O_4$	0,02	0,04
	$NiCo_2O_4$		
6[c]	$NiCo_2O_4$		

[a] synthesized during Specialization Project, autumn 2016.
[b] precipitated together in a large batch, and calcined at different temperatures after drying.
[c] $NiCo_2O_4$ synthesized as support for 0,5wt%Pd/$NiCo_2O_4$.

The mass of precursors were calculated according to Equation A.1, where m is the mass, n is the amount of mol and Mm is the molar mass.

$$m = n \cdot Mm \qquad [g] \tag{A.1}$$

Equation A.2 exemplifies the calculation of correct amount of nickel precursor for the stoichio-

metric catalyst.

$$\begin{aligned} m_{Ni-pre} &= 0,01mol \cdot 290,786\frac{g}{mol} \\ &= 2,908g \end{aligned} \tag{A.2}$$

The needed amount of precursors for both catalysts are presented in Table 3.1.

The precipitation agent was a solution of 1 M KOH, which was prepared using solid KOH. The different amounts and volumes used to prepare this solution is presented in Table A.2, which were found according to Equation A.3 and A.1. In Equation A.3 M is the desired molarity of the solution, and V is the volume.

$$n = M \cdot V \tag{A.3}$$

Table A.2: Amount of solid potassium hydroxide and volume of deionized water to to make the desired molarity of precipitation agent, (aq-H_2O). KOH_{aq} denotes the amount of precipitation agent used to produce the different batches of catalyst. de-H_2O indicate the amount of H_2O used to ionize the precursor compounds for the different catalysts.

Batch	**Catalyst**	**KOH**	**aq-H_2O**	**KOH_{aq}**	**de-H_2O**
		Mass [g]	V^a_{dilute} [mL]	V [mL]	V [mL]
1^a	$NiCo_2O_4$				
2^a	$NiCoO_4$	11,22	200	150	50
3	$Ni_{0,75}Co_{2,25}O_4$				
4+5[b]	$NiCo_2O_4$				
	$NiCo_2O_4$	16,83	300	300	100
6^c	$Ni_{0,75}Co_{2,25}O_4$				

[a] synthesized during Specialization Project, autumn 2016.
[b] precipitated together in a large batch, and calcined at different temperatures after drying.
[c] $NiCo_2O_4$ synthesized as support for 0,5wt%Pd/$NiCo_2O_4$.

A.2 Synthesis by Impregnation

The amount of Palladium nitrate, $Pd(NO_3)_2$, used for incipient wetness impregnation to synthesise the 0,5wt%Pd/$NiCo_2O_4$ catalyst was calculated according to Equations A.4-A.6, where

the desired weight percent of Pd is denoted wt%Pd and $m_{NiCo_2O_4}$ is the amount of support.

$$\begin{aligned} m_{\mathrm{Pd}} &= \frac{wt\%\mathrm{Pd} \cdot \mathrm{m}_{\mathrm{NiCo_2O_4}}}{100\%} \\ &= \frac{0,5\% \cdot 2,4770g}{100\%} \\ &= 12,4mg \end{aligned} \tag{A.4}$$

$$\begin{aligned} n_{\mathrm{Pd(NO_3)_2}} &= n_{Pd} \\ &= \frac{m_{\mathrm{Pd}}}{Mm_{\mathrm{Pd}}} \\ &= \frac{0,0124g}{106,42\frac{g}{mol}} \\ &= 1,165 \cdot 10^{-4} mol \end{aligned} \tag{A.5}$$

$$\begin{aligned} m_{\mathrm{Pd(NO_3)_2}} &= n_{\mathrm{Pd(NO_3)_2}} \cdot Mm_{\mathrm{Pd(NO_3)_2}} \\ &= 1,165 \cdot 10^{-4} mol \cdot 230,43 \frac{g}{mol} \\ &= 26,8mg \end{aligned} \tag{A.6}$$

Appendix B

Calibration of Mass Flow Controllers

The mass flow controllers (MFCs) were calibrated using a stop watch and a feed bypass to a bubblemeter. The flow rate was found by measuring the time a bubble took to pass a 1, 10 or 100 mL mark. The aim was to find the flow rates at given set points of the MFCs. An average of three flow rates measured for each MFC set point was used to obtain the calibration curves for the respective MFCs. The measured flow rates were converted from mL/min to NmL/min using Equation B.1, where $F_{measured}$ is the measured flow rate , T is the room temperature in Kelvin and T_0 is 273 K.

$$F = F_{measured} \cdot \frac{T}{T_0} \qquad \left[\frac{NmL}{min}\right] \tag{B.1}$$

During the experimental work, the pressure vessel and pressure regulator for the synthetic air was changed. The MFC for the synthetic air was thus recalibrated, after the change of the gas pressure regulator. Figure B.1, presents the calibration curves for the MFC for **(a)** concentrated methane, **(b)** diluted methane (5% CH_4 in N_2), **(c)** first calibration of synthetic air, **(d)** second calibration of synthetic air and **(e)** nitrogen.

To obtain the correct set point reflecting the desired flow rate for the reaction, the flow rate was inserted to the calibration curve. Equations B.2-B.3 presents the calculation of the necessary flow rate of CH_4 for the respective set point of the CH_4 MFC, resulting in a feed gas of 2% CH_4. The latter was found using the calibration curve for concentrated CH_4 MFC, given in Figure B.1a. In the expression $y = 20,019 \cdot x - 0,1312$, y denotes the flow rate of CH_4 and x the CH_4 MFC set point.

$$\begin{aligned} F_{H_2} &= \frac{2\%}{100\%} \cdot 200 \frac{NmL}{min} \\ &= 4 \frac{NmL}{min} \end{aligned} \tag{B.2}$$

$$\begin{aligned} \%MFC &= \frac{F_{\mathrm{H_2}} + 0,1312}{20,019} \cdot 100\% \\ &= \frac{4 + 0,1312}{20,019} \cdot 100\% \\ &= 20,63\% \end{aligned} \tag{B.3}$$

Figure B.1f presents the calibration curve for the liquid flow controller (LFC), that controlled the H_2O flow. This was calibrated in June 2016. The flow of H_2O in g/h was found according to Equation B.4, and the set point of the LFC was found according to Equation B.3.

$$\begin{aligned} F_{\mathrm{H_2O}} &= 30\frac{\mathrm{mL}}{\mathrm{min}} \cdot 10^{-3}\frac{\mathrm{L}}{\mathrm{mL}} \cdot 60\frac{\mathrm{min}}{\mathrm{h}} \\ &= 5 \cdot 10^{-4}\frac{\mathrm{L}}{\mathrm{h}} \cdot \frac{18\mathrm{g\,mol^{-1}}}{22,4\mathrm{L\,mol^{-1}}} \\ &= 1,446\frac{\mathrm{g}}{\mathrm{h}} \end{aligned} \tag{B.4}$$

Table B.1 presents the set points for the MFCs and the LFC for the different Runs presented in Table 3.5. The flow rates and set points were calculated according to the Equations above, with the calibration curves for the respective gases, given in Figure B.1.

Table B.1: The mass flow controller (MFC) set points of CH_4 (concentrated and diluted), synthetic air (O_2), N_2 and the liquid flow controller (LFC) for H_2O, used in Runs 1-17. The total flow rate was 200 $\mathrm{NmL \cdot min^{-1}}$, and the respective flow rates of the components can be reviewed in Table 3.5.

Reactant feed	**CH_4** MFC [%]	**O_2**[b] MFC [%]	**N_2** MFC [%]	**H_2O** LFC [g/h]	**Run**
2%	20,63	90,67/90,7[c]	15,4	-	1, 6, 8, 10, 12, 14
0,5%	15,82	90,67[d]/90,7	15,82	-	2, 7, 9, 11, 13
0,1%	19,77[a]	90,7	15,4	-	3, 5, 15, 17
$0,1\%_{H_2O}$	19,77[a]	90,7	11,3	13,43	4, 16

[a] diuted methane ($5\%CH_4$ in N_2).
[b] synthetic air.
[c] MFC set point for Run 1 and 14 was 90,7, due to change of pressure regulator and recalibration.
[d] MFC set point for Run 13 was 90,67, due to change of pressure regulator and recalibration.

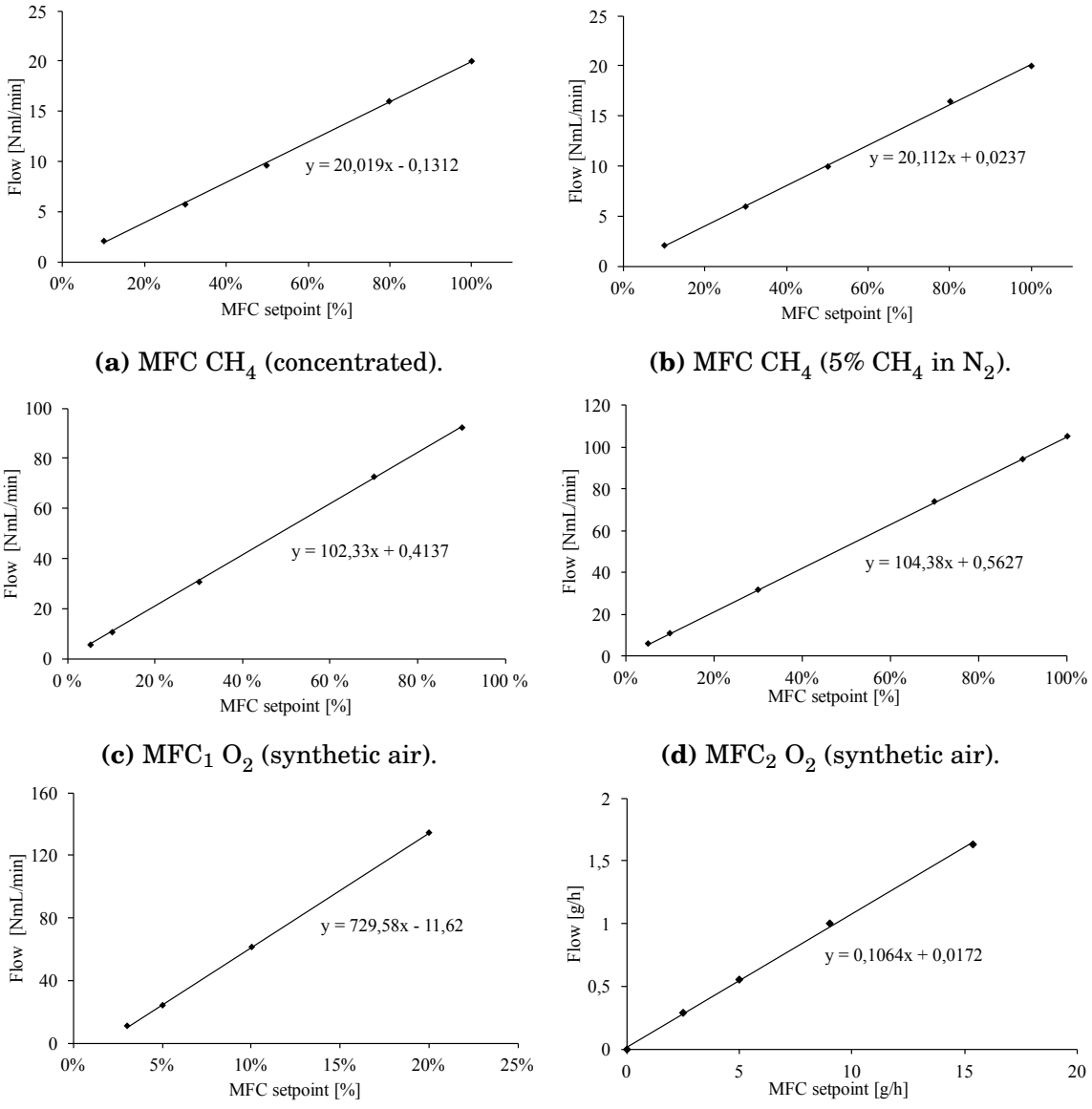

(a) MFC CH_4 (concentrated).

(b) MFC CH_4 (5% CH_4 in N_2).

(c) MFC_1 O_2 (synthetic air).

(d) MFC_2 O_2 (synthetic air).

(e) MFC N_2.

(f) LFC H_2O.

Figure B.1: Calibration curves for mass flow controllers (MFCs) for concentrated CH_4, diluted CH_4, N_2 and synthetic air, and liquid flow controller (LFC) for H_2O. The pressure regulator of synthetic air was changed during the lab work, and the MFC was thus recalibrated. The first and second calibration are presented in figures **(c)** and **(d)**, respectively.

Appendix C

Reproducibility and Accuracy

C.1 XRD Reproducibility

Figure C.1 presents the spectra of two XRD-analyses of the reference catalyst $NiCo_2O_4$. The two spectra displayed highly similar features, and the method of XRD analysis was thus deemed accurate. Figure C.2 show the XRD spectra for all batches of stoichiometric spinel calcined at 350°C, where red indicates the reference catalyst, batch 1 (denoted $NiCo_2O_4$, gray indicate batch 4 (denoted $NiCo_2O_{4-350°C}$) and blue indicates batch 6, which was synthesized as support for 0,5wt%Pd/$NiCo_2O_4$. The three spectra indicate that the three materials exhibit the same phases. This indicates that the catalyst synthesizes was conducted with similar procedure.

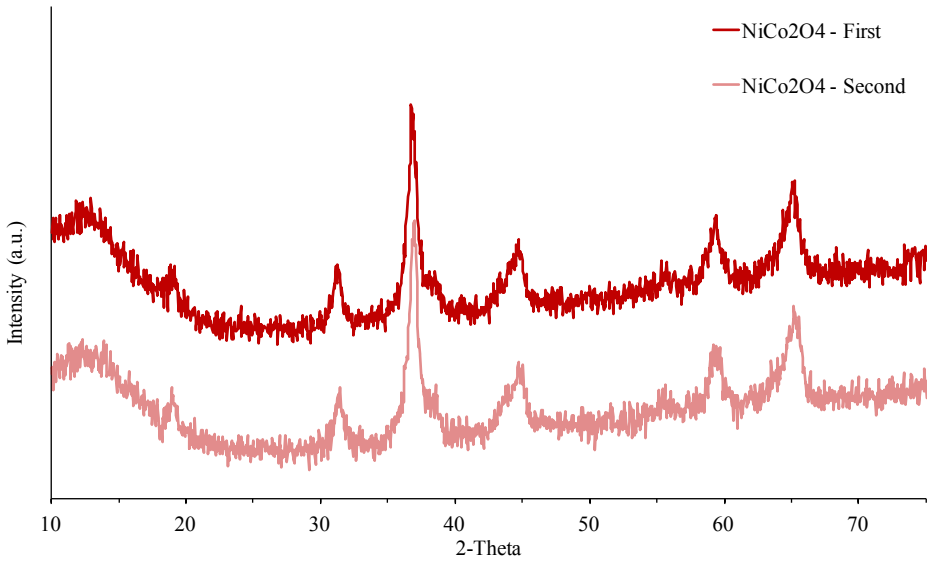

Figure C.1: The XRD spectra for two analyses of the reference catalyst $NiCo_2O_4$. The reproducibility of the method of XRD analysis was deemed acceptable, as the two obtained spectra displayed highly similar features.

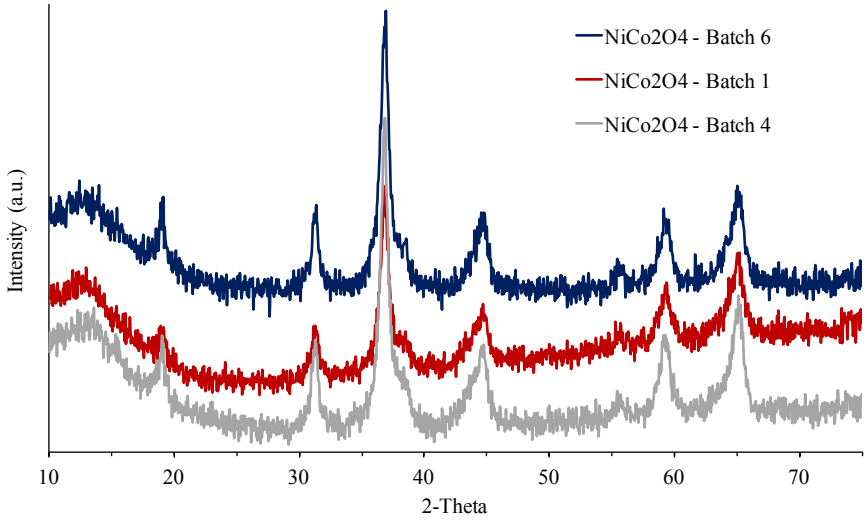

Figure C.2: The XRD spectra for all batches made of $NiCo_2O_4$ calcined at 350°C. Batch 6, indicated by blue, was used as a support for 0,5wt%Pd/$NiCo_2O_4$. The three catalysts display similar features, which indicate that the preparation of the three catalysts was similar.

C.2 Nitrogen Physisorption Deviation

Deviation, d, from first and second analysis of the reference catalyst was calculated according to Equation C.1. $S_{1,BET}$ and $S_{2,BET}$ respectively indicate the measured surface area for the first and second analysis by N_2 physisorption. All obtained results can be reviewed in Table 4.1.

$$\begin{aligned} d &= \pm \frac{(S_{1,BET} - S_{2,BET})}{S_{1,BET}} \cdot 100\% \\ &= \pm \frac{53,5 - 55,6}{53,6} \cdot 100\% \\ &= \pm 3,9\% \end{aligned} \tag{C.1}$$

C.3 Theoretical Mass Percent for X-ray Fluorescence

For a catalyst with the stoichiometric relationship $Ni_aCo_bO_4$ the theoretical mass percentage $m\%_t$ can be calculated according to Equation C.2. In this equation, calculation of the mass percentage is singularly based on the metal species in the mixed oxide, as the XRF-analysis provide the mass percentages of metal species in the analyzed sample. Equation C.2 includes

an example for the calculation of the theoretical mass percentage of Co in $NiCo_2O_4$, where m_i denotes the mass of compound i.

$$\begin{aligned} m\%_t &= \frac{b \cdot m_{Co}}{a \cdot m_{Ni} + b \cdot m_{Co}} \cdot 100\% \\ &= \frac{2 \cdot 58,93}{58,69 + 2 \cdot 58,93} \cdot 100\% \\ &= 66,75\% \end{aligned} \tag{C.2}$$

Table C.1 presents the theoretical mass percentage of the compounds in the different catalysts. The results of the XRF analyses were compared to the theoretical amounts to gain information about the synthesis accuracy. The deviations from theoretical mass percentage was calculated according to Equation C.3, where $m\%_m$ is the measured mass percentage. The measured mass percentages and the respective deviations from theoretical value are presented in Table 4.2. C.3 includes an example of the deviation of measured amount of cobalt from the first analysis of the reference catalyst $NiCo_2O_4$, and the theoretical mass percentage of cobalt in $NiCo_2O_4$.

$$\begin{aligned} d &= \pm \frac{m\%_m - m\%_t}{m\%_t} \cdot 100\% \\ &= \pm \frac{65,2 - 66,75}{66,75} \cdot 100\% \\ &= -2,3\% \end{aligned} \tag{C.3}$$

Table C.1: Theoretical mass percentage of each component, calculated according to Equation C.2, used to investigate nominal deviations of the catalysts. The results obtained from XRF-analyses are presented in Table 4.2.

Batch	**Catalyst**	**Co^{3+} Mass%**	**Ni^{2+} Mass%**	**Pd^{2+} Mass%**
1, 4, 5	$NiCo_2O_4$	66,75	33,25	-
2	$NiCoO_4$	50,1	49,9	-
3	$Ni_{0,75}Co_{2,25}O_4$	75,1	24,9	-
6	0,5 wt%Pd/$NiCo_2O_4$	66,4	33,1	0,5

Appendix D

Arrhenius plots

The Arrheius plots were found by using the method outlined in Section 2.6.2. $\ln(-\ln(1-X_{CH_4}))$ was calculated for methane levels from 10-50% conversion, and plotted against 1000/T. The respective temperatures were found by utilizing the polynomial fitted to the μGC- and temperature logs. Figure D.1 presents the Arrhenius plots for all reactant feeds over the reference catalyst, $NiCo_2O_4$. Figures D.2, D.3, D.4 and D.5 respectively presents the Arrhenius plots over the two reactions over the catalysts $NiCoO_4$, $Ni_{0,75}Co_{2,25}O_4$, $NiCo_2O_{4\,350°C}$ and $NiCo_2O_{4\,550°C}$. Figure D.6 presents the plots for reactions over 0,5wt%Pd/$NiCo_2O_4$. All figures indicate which run they are denoted as in the report. The expressions obtained for the different plots are on the form $\ln(-\ln(1-X_{CH_4})) = \ln(A) + \frac{-E_A}{R} \cdot \frac{1}{T}$. The slope of the obtained line was thus multiplied with the negative gas constant (-R) to attain the activation energy for the different systems. The obtained activation energies are presented in the Tables 4.5-4.8 in Section 4.2.

Figure D.7 presents the Arrhenius plots for reaction over two catalysts, 2wt%Pd/Al_2O_4 and 0,2wt%Pd/Al_2O_4, calculated with basis on measurements reported by Sandvik in [4].

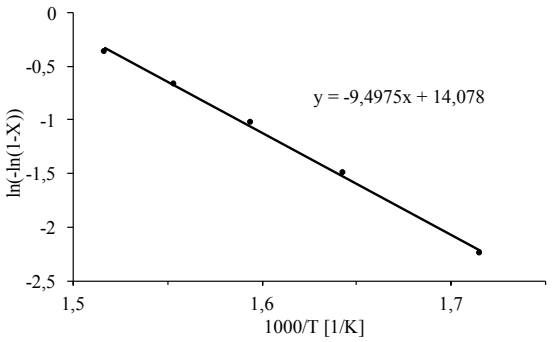

(a) Run 1: 2% CH_4, 10% O_2 and 88% N_2.

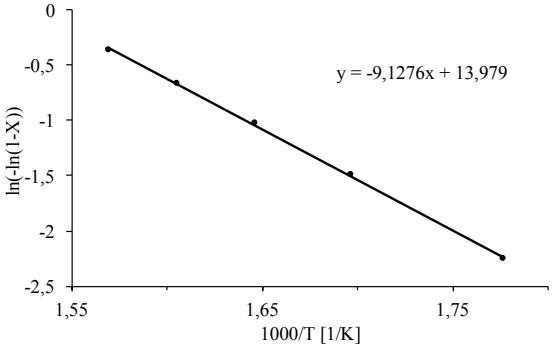

(b) Run 2: 0,5% CH_4, 10% O_2 and 89,5% N_2.

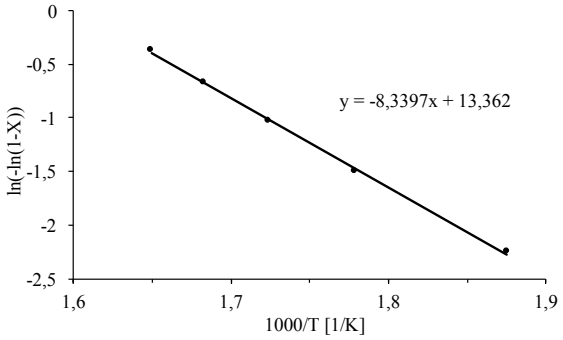

(c) Run 3: 0,1% CH_4, 10% O_2 and 89,9% N_2.

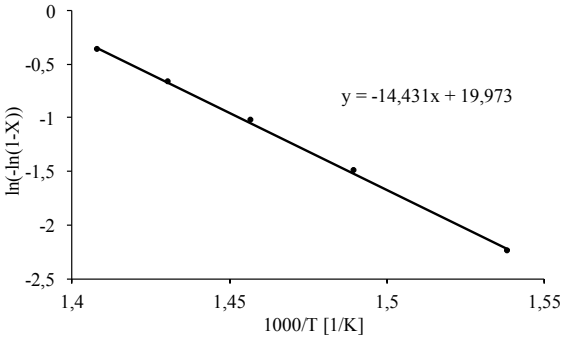

(d) Run 4: 0,1% CH_4, 10% O_2, 15% H_2O and 74,9% N_2.

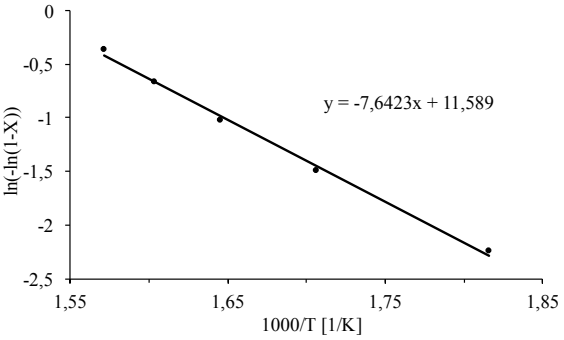

(e) Run 5: 0,1% CH_4, 10% O_2 and 89,9% N_2.

Figure D.1: Arrhenius plots for $NiCo_2O_4$ (Batch 1) for different feed compositions. The expressions obtained for the different plots are on the form $\ln(-\ln(1-X_{CH_4})) = \ln(A) + \frac{-E_A}{R} \cdot \frac{1}{T}$. The Arrhenius method is presented in Section 2.6.2.

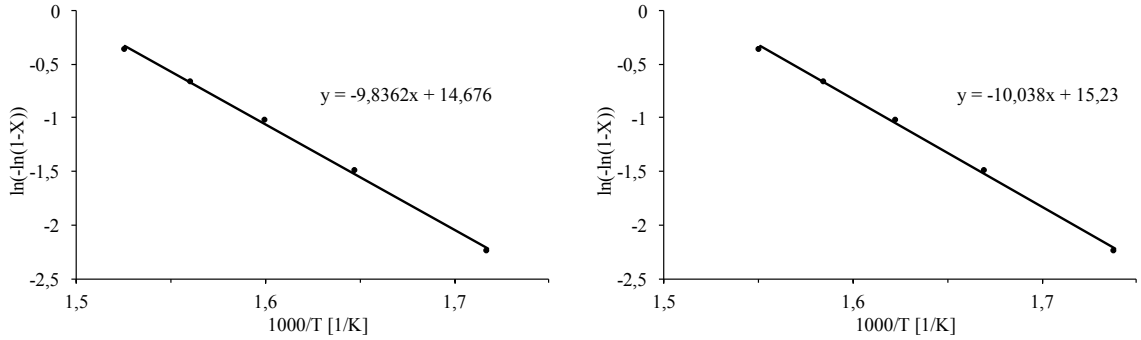

(a) Run 6: 2% CH_4, 10% O_2 and 88% N_2. **(b)** Run 7: 0,5% CH_4, 10% O_2 and 89,5% N_2.

Figure D.2: Arrhenius plots for $NiCo_2O_4$ (Batch 2) for different feed compositions. The expressions obtained for the different plots are on the form $\ln(-\ln(1-X_{CH_4})) = \ln(A) + \frac{-E_A}{R} \cdot \frac{1}{T}$. The Arrhenius method is presented in Section 2.6.2.

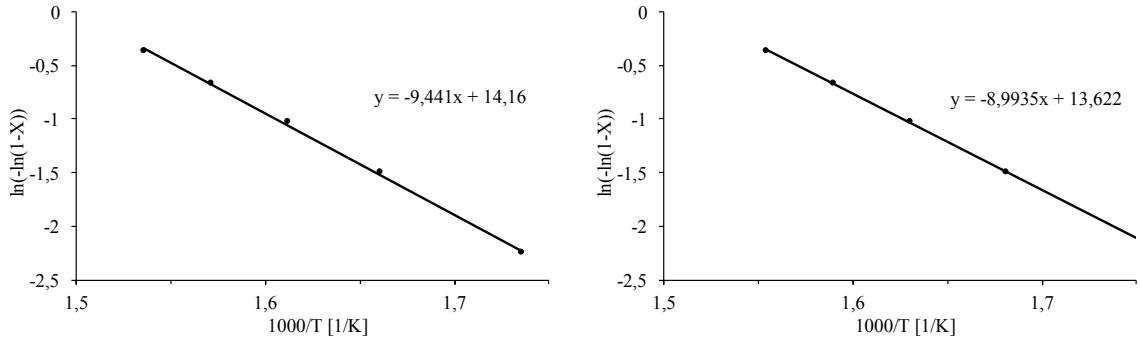

(a) Run 8: 2% CH_4, 10% O_2 and 88% N_2. **(b)** Run 9: 0,5% CH_4, 10% O_2 and 89,5% N_2.

Figure D.3: Arrhenius plots for $Ni_{0,75}Co_{2,25}O_4$ (Batch 3) for different feed compositions. The expressions obtained for the different plots are on the form $\ln(-\ln(1-X_{CH_4})) = \ln(A) + \frac{-E_A}{R} \cdot \frac{1}{T}$. The Arrhenius method is presented in Section 2.6.2.

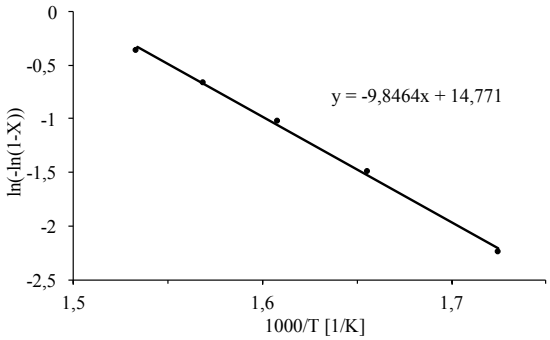

(a) Run 10: 2% CH_4, 10% O_2 and 88% N_2.

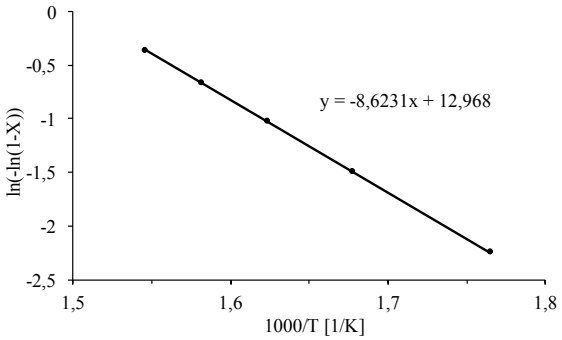

(b) Run 11: 0,5% CH_4, 10% O_2 and 89,5% N_2.

Figure D.4: Arrhenius plots for $NiCo_2O_{4\,350°C}$ (Batch 4) for different feed compositions. The expressions obtained for the different plots are on the form $\ln(-\ln(1-X_{CH_4})) = \ln(A) + \frac{-E_A}{R} \cdot \frac{1}{T}$. The Arrhenius method is presented in Section 2.6.2.

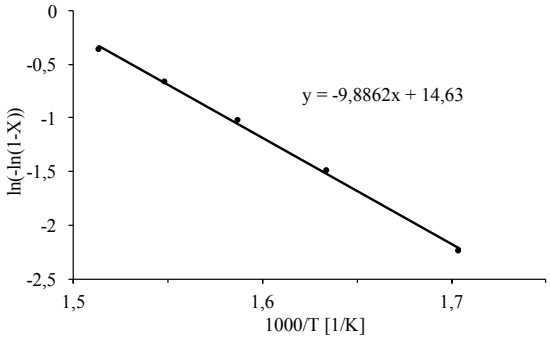

(a) Run 12: 2% CH_4, 10% O_2 and 88% N_2.

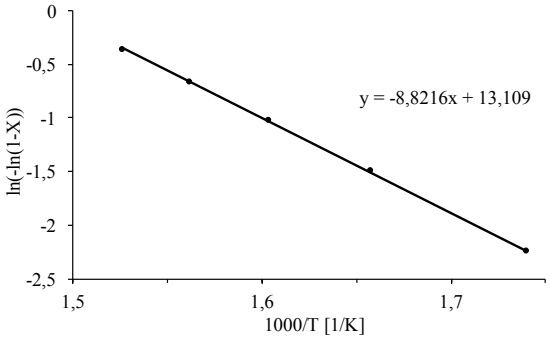

(b) Run 13: 0,5% CH_4, 10% O_2 and 89,5% N_2.

Figure D.5: Arrhenius plots for $NiCo_2O_{4\,550°C}$ (Batch 5) for different feed compositions. The expressions obtained for the different plots are on the form $\ln(-\ln(1-X_{CH_4})) = \ln(A) + \frac{-E_A}{R} \cdot \frac{1}{T}$. The Arrhenius method is presented in Section 2.6.2.

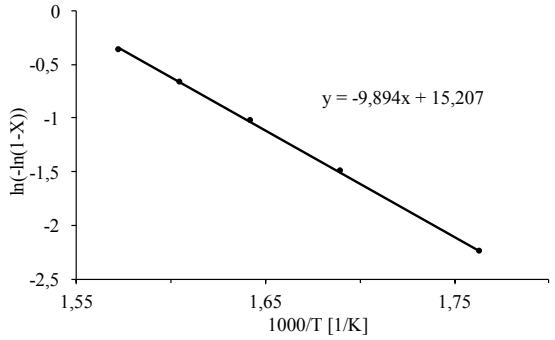

(a) Run 14: 2% CH_4, 10% O_2 and 88% N_2.

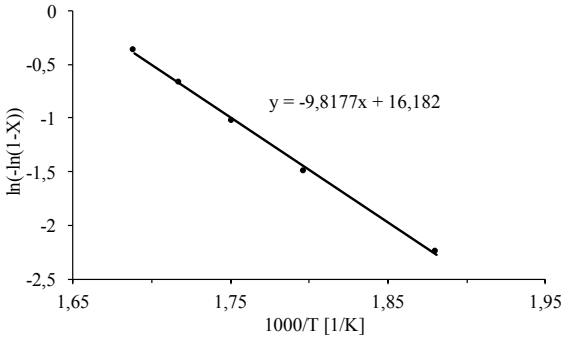

(b) Run 15: 0,1% CH_4, 10% O_2 and 89,9% N_2.

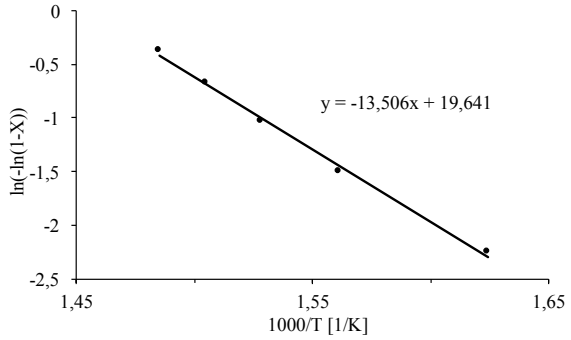

(c) Run 16: 0,1% CH_4, 10% O_2, 15% H_2O and 74,9% N_2.

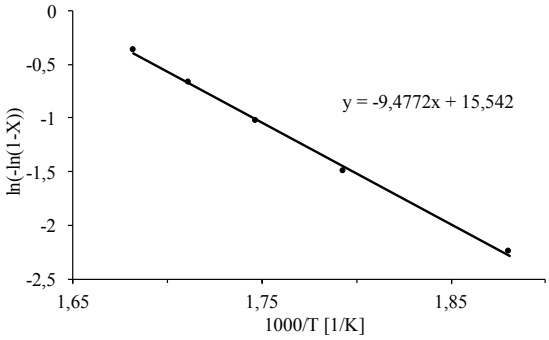

(d) Run 17: 0,1% CH_4, 10% O_2 and 89,9% N_2.

Figure D.6: Arrhenius plots for 0,5wt%Pd/$NiCo_2O_4$ (Batch 6) for different feed compositions. The expressions obtained for the different plots are on the form $\ln(-\ln(1-X_{CH_4})) = \ln(A) + \frac{-E_A}{R} \cdot \frac{1}{T}$. The Arrhenius method is presented in Section 2.6.2.

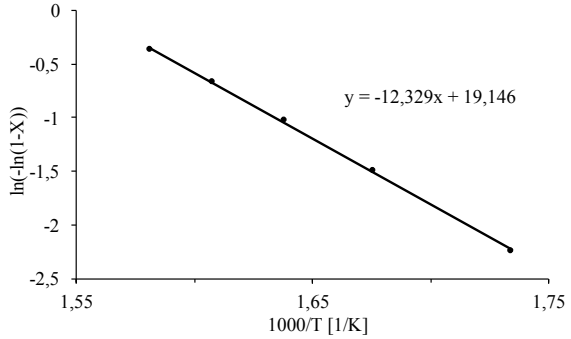

(a) 2wt%Pd/Al_2O_4.

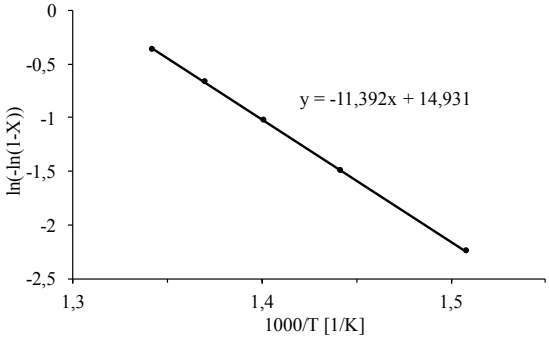

(b) 0,2wt%Pd/Al_2O_4.

Figure D.7: Arrhenius plots for reaction over two catalysts produced by Sandvik with feed composition 2% CH_4, 10% O_2 and 88% N_2. The plots are based on measurements reported in [4]. The expressions obtained for the different plots are on the form $\ln(-\ln(1-X_{CH_4})) = \ln(A) + \frac{-E_A}{R} \cdot \frac{1}{T}$. The Arrhenius method is presented in Section 2.6.2.

Appendix E

Caron Balance Error

The mass balance of the system was calculated for error over carbon according to Equation 3.11, presented in Section 3.4.2. The carbon balance for all investigated reactions are presented in Figures E.1-E.4, where the carbon error is plotted against conversion of CH_4.

Figure E.1 presents the carbon error for the reactions with 2% methane in feed over all catalysts. The carbon error from the reactions with 0,5% methane feed are presented in Figure E.2. Figure E.3 presents the carbon error for the four reactions with 0,1% methane in feed, and Figure E.4 for the $0{,}1\%_{H_2O}$ feed. The two latter reactions were only investigated for the reference catalyst $NiCo_2O_4$ and over 0,5wt%Pd/$NiCo_2O_4$. All figures indicate which run they are denoted as in the report.

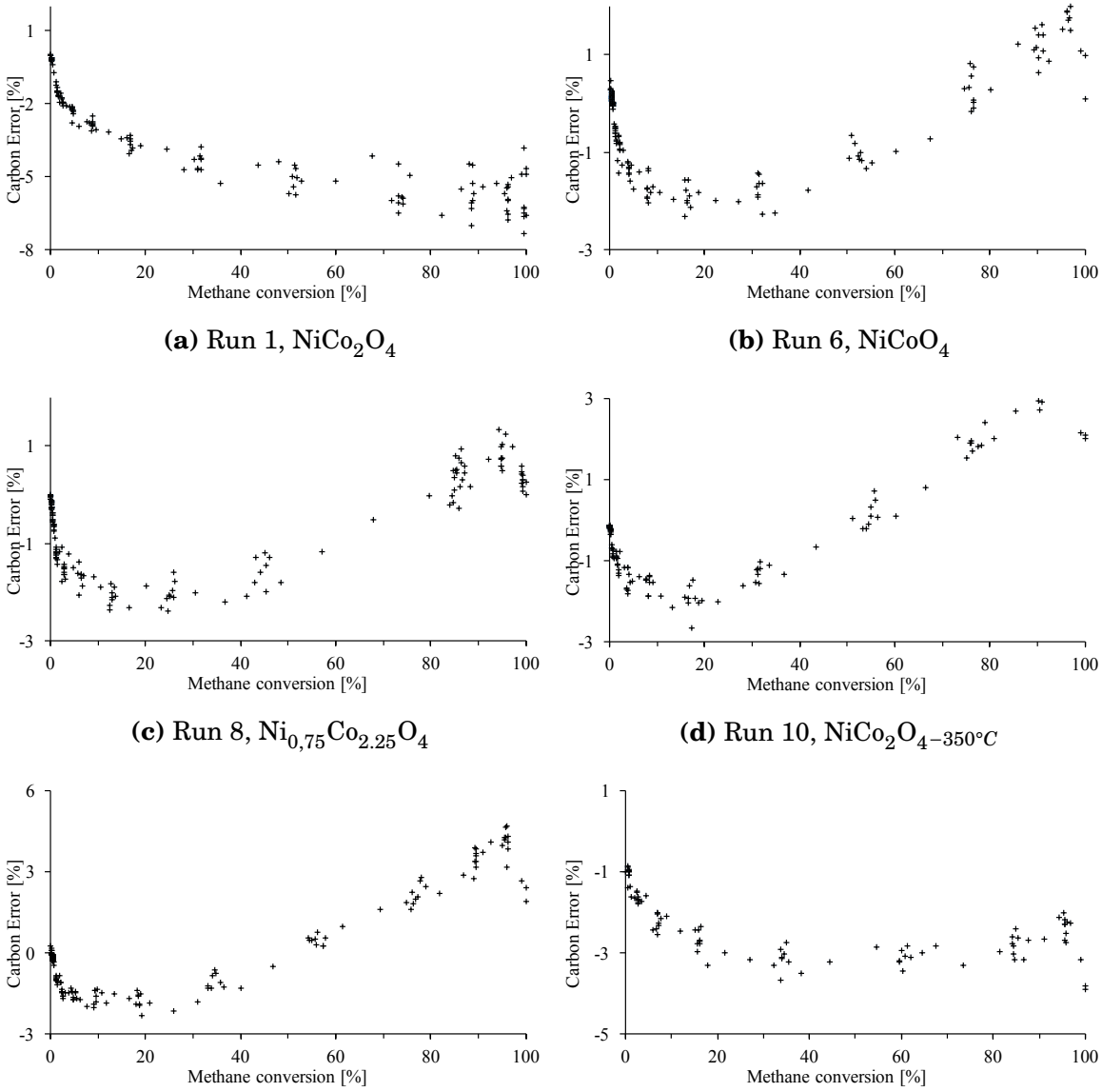

(a) Run 1, $NiCo_2O_4$

(b) Run 6, $NiCoO_4$

(c) Run 8, $Ni_{0,75}Co_{2.25}O_4$

(d) Run 10, $NiCo_2O_{4-350°C}$

(e) Run 12, $NiCo_2O_{4-550°C}$

(f) Run 14, 0,5wt%Pd/$NiCo_2O_4$

Figure E.1: Carbon balance error plotted against conversion of methane for six reactions over different catalysts, with 2% CH_4, 10% O_2 and 88% N_2. The error was calculated according to Equation 3.11, and the indicated activities can be reviewed in Table 4.4.

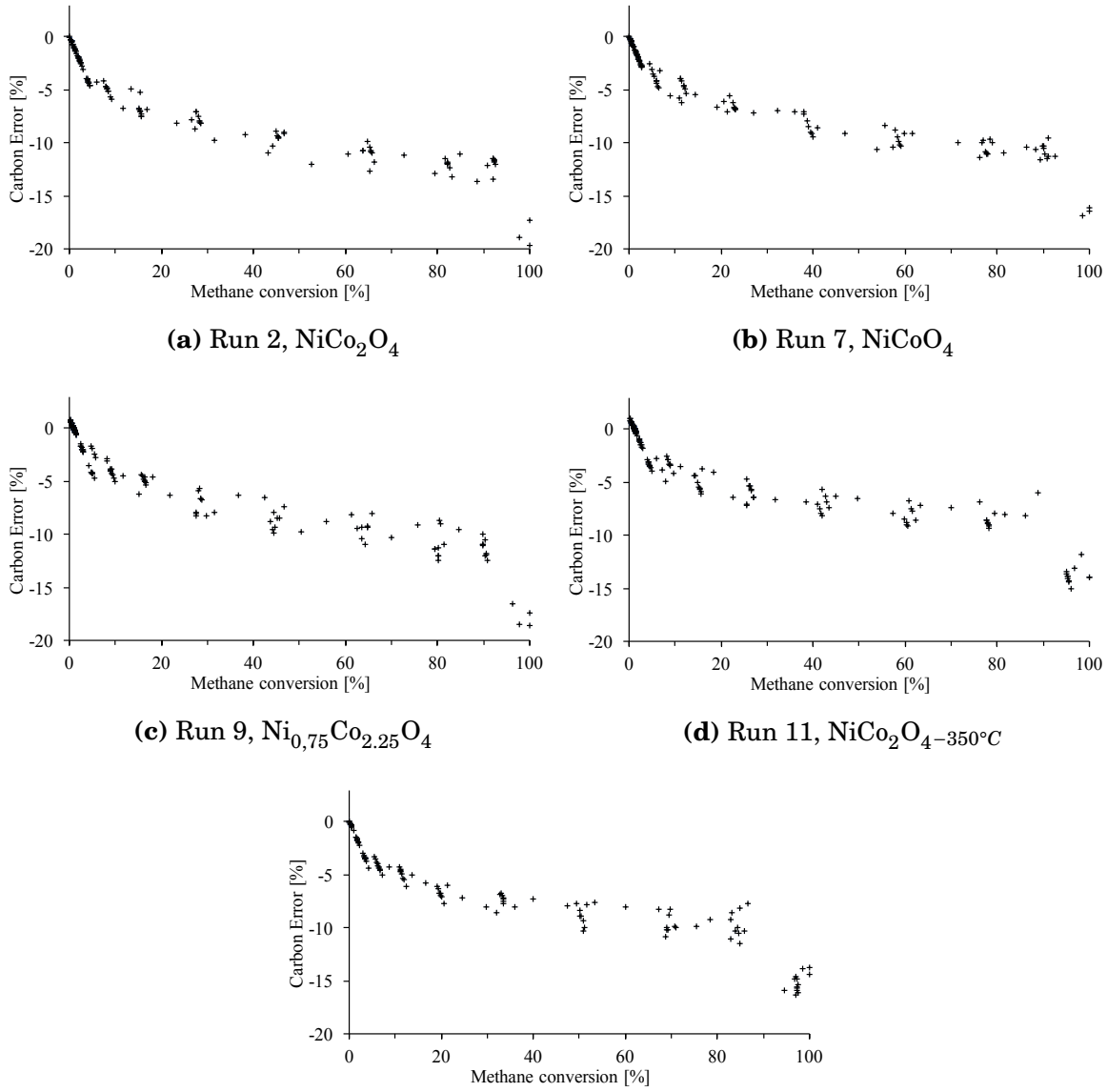

(a) Run 2, $NiCo_2O_4$

(b) Run 7, $NiCoO_4$

(c) Run 9, $Ni_{0,75}Co_{2.25}O_4$

(d) Run 11, $NiCo_2O_{4-350°C}$

(e) Run 13, $NiCo_2O_{4-550°C}$

Figure E.2: Carbon balance error plotted against conversion of methane for five reactions over different catalysts, with 0,5% CH_4, 10% O_2 and 89,5% N_2. The error was calculated according to Equation 3.11, and the indicated activities can be reviewed in Table 4.4.

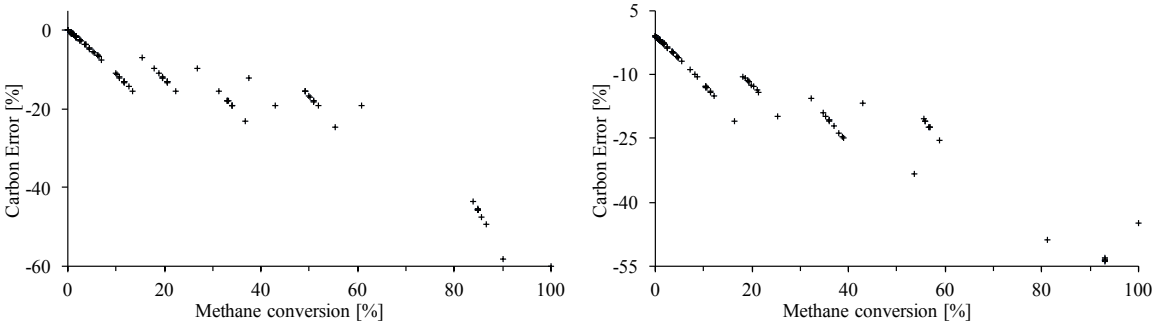

(a) Run 3, $NiCo_2O_4$

(b) Run 15, 0,5wt%Pd/$NiCo_2O_4$

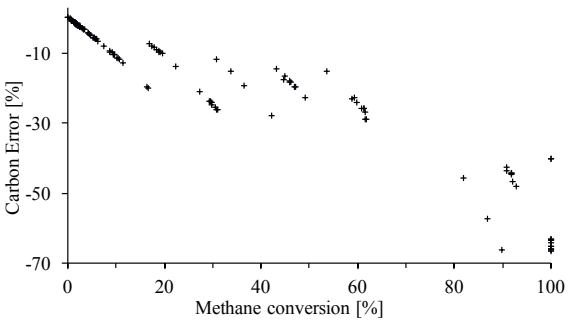

(c) Run 5, $NiCo_2O_4$

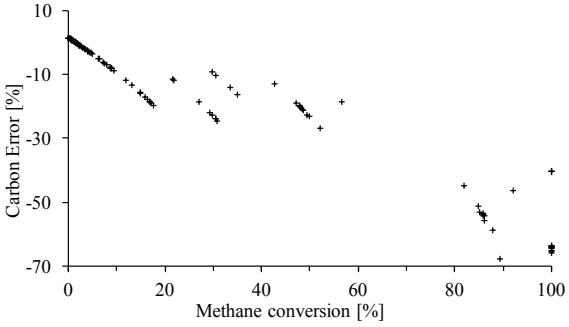

(d) Run 17, 0,5wt%Pd/$NiCo_2O_4$

Figure E.3: Carbon balance error plotted against conversion of methane for four reactions over different catalysts, with 0,1% CH_4, 10% O_2 and 89,9% N_2. The error was calculated according to Equation 3.11, and the indicated activities can be reviewed in Table 4.4.

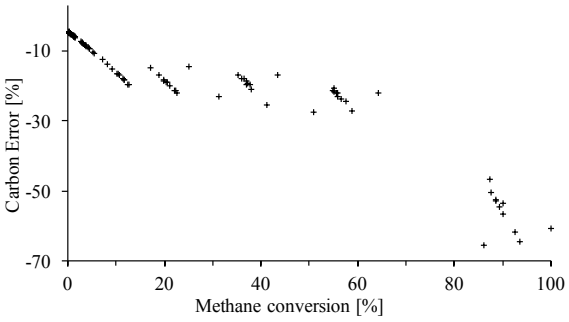

(a) Run 4, $NiCo_2O_4$

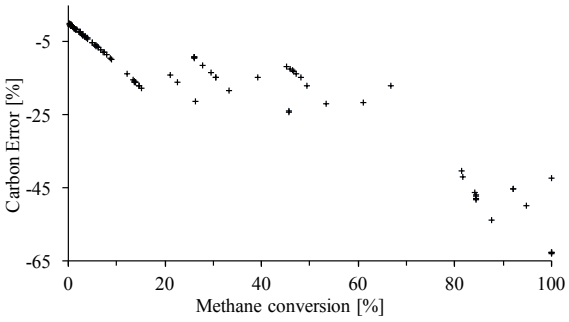

(b) Run 16, 0,5wt%Pd/$NiCo_2O_4$

Figure E.4: Carbon balance error plotted against conversion of methane for two reactions over different catalysts, with 0,1% CH_4, 15% H_2O, 10% O_2 and 89,9% N_2. The error was calculated according to Equation 3.11, and the indicated activities can be reviewed in Table 4.4.

Appendix F

Calculations

F.1 Calculation of Lambda

The air fuel equivalence ratio for the different feed compositions, λ, were calculated according to Equation 2.2. Equation F.1 presents an example of the air-to-fuel ratio (AFR) calculation and Equation F.2 presents the calculation of λ for the reactant feed with 2% CH_4 and 10% O_2 (with respective flow rates 4 and 20 NmL/min).

$$\begin{aligned} AFR_{2\%} &= \frac{n_{air}}{n_{fuel}} \\ &= \frac{10}{2} \\ &= 5 \end{aligned} \tag{F.1}$$

$$\begin{aligned} \lambda &= \frac{\text{AFR}}{\text{AFR}_{Stoic}} \\ &= 5/2 \\ &= 2,5 \end{aligned} \tag{F.2}$$

F.2 Calculation of Reaction Rate

The reaction rate was calculated according to Equation 2.7. This equation yelds a rate with the dimension $\text{molh}^{-1}\text{g}_{\text{cat}}^{-1}$. The reaction rate was modified to express the rate per gram palladium on the catalyst, to compare the catalysts produced for this thesis with those reported by Sandvik [4]. This was done according to Equation F.3.

$$r = \frac{r_{\text{cat}}}{\text{Pd}wt\%/100} \qquad \left[\frac{mol}{h \cdot g_{\text{Pd}}}\right] \tag{F.3}$$

Appendix G

Matlab Script

Listing G.1: Matlab script to estiamte activity. Example for temperature and conversion measurements from Run 1.

```
%Matlab program to plot conversion (y) as a function of temperature
%(x) to find T10, T30, T50, T70 and T90.

%clear memory
clear all
close all
clc

format long g

%Import data from excel(taken from sheet of measured and calculated
    points)
T_exp = [227.99
     252.86
     279.52
     304.75
     332.47
     361.35
     392.56
     426.72
     457.99
     486.34
     514.96];

c_exp = [1.49
     2.53
     4.73
     8.85
```

```
28      19.69
29      30.86
30      57.85
31      73.22
32      88.85
33      96.09
34      100];
35
36  p = polyfit(T_exp,c_exp,5);
37
38  T_plot = 227.90:0.1:515;
39  c_plot = polyval(p,T_plot);
40
41  figure(1)
42  set(gcf,'color','w');
43  plot(T_exp,c_exp,'ro',T_plot,c_plot,'k-')
44  grid
45  legend('Experimental',...
46      'Fitted curve',...
47      'Location', 'Northwest');
48  title('Conversion at Temperautre')
49  xlabel('Temperature, \it T \rm [C]')
50  ylabel('Conversion, \rm [%]')
51
52  %Find T at given C (10, 30, 50, 70, 90%) when difference between
        function
53  %and C is minimum. Can alter to find C=10-50 to estimate Activation
        Energy.
54
55  T_C = zeros(1,5);
56  C=10;
57  for i=1:5
58      [difference, index] = min(abs(c_plot-C));
59      T_C(i) = T_plot(index);
60      C=C+20
61  end
62
63  %Conversion at given T, T=325 used to estimate reaction rate.
```

```
64 T_325 = 325;
65 C_325 = polyval(p,T_325);
```